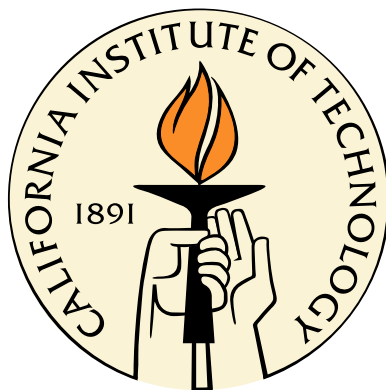


# Structural Dynamics by Ultrafast Electron Crystallography

Thesis by  
Songye Chen

In Partial Fulfillment of the Requirements  
for the Degree of  
Doctor of Philosophy



California Institute of Technology  
Pasadena, California

2007  
(Defended November 30, 2006)

© 2007

Songye Chen

All Rights Reserved

To my beloved daughter Hanning.

# Acknowledgements

I would like to express my sincere gratitude to my advisor, Professor Ahmed H. Zewail, for his attentive guidance during this work. Without his scientific vision and insight, his passion to push the frontier of science, and his generous support, this work would not have been possible.

I have been very fortunate to work with many talented postdoctoral fellows and graduate students. I thank all of them: Dr. Franco Vigliotti, Dr. Vladimir A. Lobastov, Dr. Chong-Yu Ruan, Dr. Marco T. Seidel, Dr. Nuh Gedik, Dr. Peter Baum, and Jerry (Ding-shyue) Yang.

Other members in Professor Zewail's group have given me much help over the years, especially these people in UED3: Dr. Boyd Goodson, Dr. Ramesh Srinivasan, Dr. Jonathan S. Feenstra and Dr. Sang Tae Park; and two theorists: Dr. Scott Habershon and Dr. Jau Tang.

I would also like to acknowledge Professor Nathan S. Lewis and Dr. Lauren Webb for help in preparing the silicon surfaces; Professor James R. Heath for the use of his Langmuir-Blodgett film preparation facilities, Peigeng Cao, Dr. Yi Luo, and Dr. Hongbin Yu for advice and discussion on Langmuir-Blodgett films.

This work was supported by the National Science Foundation and the Air Force Office of Scientific Research. I thank the Robert A. Millikan Fellowship for the financial support in the first three years of my graduate work.

Last but not least, I thank my family for giving me all their love and support.

# Abstract

Ultrafast electron crystallography (UEC), combining the ultrafast time resolution with femtosecond lasers and the atomic spatial resolution with electron crystallography, is developed and applied to elucidate the structural dynamics in solids, surfaces and macromolecular systems. The UEC experiments for surface studies were first demonstrated on semiconductor surfaces. Coherent nonthermal motions of atoms following ultrafast laser irradiation were shown with the timescales in picoseconds, and the amplitude of the motions was determined in picometer. Using Langmuir-Blodgett films, two-dimensional crystalline monolayer, bilayers and multilayers of fatty acids and phospholipids were also studied by UEC. The atomic structures under different preparation conditions were determined. The structural dynamics following a temperature jump induced by femtosecond laser on the substrates were obtained and compared to the equilibrium temperature dependence. It was observed that a coherent anisotropic expansion solely along the aliphatic chains happens at picosecond timescale, followed by nonequilibrium contraction and restructuring at longer times. The effects of different molecules, layer thickness and substrate on the dynamics were examined. Unlike monotonic disordering in the equilibrium heating, a transient structural ordering was revealed on the picosecond timescale.

# Contents

<b>Acknowledgements</b>	<b>iv</b>
<b>Abstract</b>	<b>v</b>
<b>1 Introduction</b>	<b>1</b>
<b>2 Apparatus</b>	<b>7</b>
2.1 UHV chamber system . . . . .	7
2.2 Electron gun system . . . . .	14
2.3 Imaging system . . . . .	18
2.4 Sample translation and manipulation . . . . .	19
2.5 Gas-handling system . . . . .	22
2.6 Femtosecond laser system . . . . .	26
<b>3 Methodology</b>	<b>30</b>
3.1 Electron crystallography . . . . .	30
3.2 Pump-probe experiment . . . . .	39
3.2.1 Characterization of the electron pulses . . . . .	41
3.2.2 Alignment of the laser and electron beams . . . . .	44
3.2.3 Measuring the laser fluence on the sample . . . . .	45
3.2.4 Determining time resolution and time zero . . . . .	46
3.3 Analysis of the diffraction patterns . . . . .	48
<b>4 Studies of Single-Crystal Surfaces with Small Adsorbates</b>	<b>51</b>
4.1 Silicon(111) surface . . . . .	52

4.2	GaAs(111) surface . . . . .	58
4.3	Surfaces with adsorbates . . . . .	68
<b>5</b>	<b>Fatty Acid and Phospholipid Crystalline Adsorbates:</b>	
	<b>Steady State Studies</b>	<b>70</b>
5.1	Langmuir-Blodgett films of fatty acids and phospholipids . . . . .	71
5.2	Preparation of layers by LB deposition . . . . .	74
5.3	Fatty acid bilayers structure . . . . .	77
5.4	Fatty acid bilayers temperature-dependent structural change . . . . .	84
5.5	Fatty acid multilayers structure . . . . .	88
5.6	Phospholipid monolayer and bilayer structure . . . . .	92
<b>6</b>	<b>Fatty Acid and Phospholipid Crystalline Adsorbates:</b>	
	<b>Ultrafast T-jump Dynamics</b>	<b>94</b>
6.1	Fatty acids structural dynamics . . . . .	95
6.1.1	Atomic motions in the chain . . . . .	98
6.1.2	Transient structural ordering . . . . .	105
6.1.3	Dynamics at different static temperature . . . . .	108
6.2	Phospholipid structural dynamics . . . . .	109
6.3	Structural dynamics picture . . . . .	113
<b>7</b>	<b>Conclusion</b>	<b>117</b>
	<b>Bibliography</b>	<b>121</b>

# List of Figures

2.1	The chamber system with frame support. . . . .	8
2.2	Schematic diagram of the experimental setup. . . . .	10
2.3	Schematic side view of the sample preparation chamber and the load-lock chamber. . . . .	13
2.4	Schematic view of the goniometer. . . . .	15
2.5	A cut through the electron gun chamber and the scattering chamber. . . . .	16
2.6	A cut through the CCD imaging system. . . . .	18
2.7	Schematic side view of the load lock chamber and the scattering chamber. . . . .	21
2.8	Schematic view of the gas-handling system. . . . .	23
2.9	The optics layout. . . . .	28
3.1	Schematic diagrams of Ewald sphere construction. . . . .	35
3.2	Schematic diagram of RHEED experiment. . . . .	37
3.3	Schematic view of the experiment. . . . .	40
3.4	Electric diagram for the streaking experiment. . . . .	42
3.5	Result of the streaking experiment. . . . .	43
3.6	Schematic diagram of the alignment. . . . .	44
3.7	Schematic diagram of the measurement of excitation laser beam spatial profile. . . . .	47
4.1	Structure of the Si:H(111) crystal. . . . .	52
4.2	Diffraction patterns of Si(111) surfaces. . . . .	53
4.3	The temporal change of the Bragg spot (-4,7). . . . .	55
4.4	UEC of phase transition of the amorphous to liquid state. . . . .	57

4.5	Structure of the GaAs:Cl(111) crystal. . . . .	58
4.6	GaAs:Cl(111) surface lattice structure. . . . .	59
4.7	Static diffraction images of the GaAs:H(111) surface. . . . .	60
4.8	Time dependence of the Bragg reflection center position. . . . .	62
4.9	Fluence dependence of the Bragg reflection center position change. . .	63
4.10	Comparison of the integrated intensity, center position and width change of the Bragg spot. . . . .	65
5.1	Structure of crystalline adsorbates of fatty acids and phospholipids. . .	73
5.2	Structure of the orthorhombic C <sub>2</sub> H <sub>4</sub> subunit cell. . . . .	74
5.3	Directions of dipping, observation and subunit cell orientation. . . . .	76
5.4	Static diffraction patterns of fatty acid bilayers. . . . .	78
5.5	Static diffraction rocking curve of fatty acid bilayers. . . . .	79
5.6	Calculated diffraction patterns. . . . .	81
5.7	Static temperature dependent diffraction patterns. . . . .	85
5.8	Static temperature dependence of diffraction intensity and subunit cell dimensions. . . . .	86
5.9	Schematic view of the static thermal behavior. . . . .	88
5.10	Multilayer diffraction patterns. . . . .	90
5.11	Inclined diffraction patterns for 8-layer samples. . . . .	91
5.12	Static diffraction patterns of DMPA samples. . . . .	93
6.1	Diffraction difference frames of the (002) Bragg spot. . . . .	96
6.2	Full analysis of the (002) Bragg spot. . . . .	97
6.3	Time dependence of the peak shift and the corresponding molecular axial length change for bilayers. . . . .	99
6.4	Dynamics of fatty acid bilayer compared to that of the substrate Si(111) surface. . . . .	100
6.5	Time dependence of the molecular axial length change for 2-, 4- and 8-layer sample. . . . .	102
6.6	Dynamics of the inclined 8-layer sample. . . . .	104

6.7	Relative intensity change $I/I_0$ as a function of time for 2-, 4- and 8-layer samples. . . . .	105
6.8	Schematic view of the transient structural ordering. . . . .	107
6.9	Dependence of the transient dynamics on initial substrate static temperature. . . . .	108
6.10	Static diffraction and diffraction difference patterns of DMPA monolayer and bilayer. . . . .	110
6.11	The axial change $\Delta c_0$ and the normalized integrated intensity of the $(hk2)$ diffraction line as a function of time. . . . .	111

# List of Tables

5.1	Lattice parameters for fatty acid bilayers. . . . .	82
5.2	Lattice parameters for fatty acid multilayers. . . . .	89

# Chapter 1

## Introduction

Structural dynamics is a very important process involving atomic motions, embodied in dynamical structural changes. It happens in all chemical and biological reactions, and many physical phase transitions. These structural changes span a wide time range, from femtoseconds (fs) to seconds or even longer. For example, the timescale of molecular vibrations is  $\sim 100$  fs and the timescale of molecular rotations is from picosecond (ps) to nanosecond (ns) [1]. In liquids, collisions of molecules happen in  $\sim 1$  to 100 fs. In solids, long-wavelength acoustic vibrations can persist for seconds or longer, but oscillations with wavelength at the atomic scale relax in a few picosecond or less. Some biochemical processes, such as conformational changes and local structural changes induced by ligand binding, occur on a fs timescale after external triggering. Within a protein, mechanical perturbations are essentially localized in  $\sim 100$  fs; acoustic dispersion takes place in the ps time range. To understand the mechanism of chemical and biological reactions and physical phase transitions stated above, it is ideal to follow the motion of atoms and identify the intermediate structures as the reactions and phase transitions proceed. As fundamental molecular vibrations and rotations happen in timescale about 100 fs, which corresponds to a distance of a few Å that the atomic nuclei travel, femtosecond and sub-ångström are the ultimate resolution in time and space needed.

Since the first laser realization in 1960, time-resolved experiments have advanced from nanoseconds to attoseconds, thanks to the generation of shorter and shorter pulses. In the last 15 years, with the discovery of fs pulse generation from solid

state Ti-sapphire lasers, femtosecond lasers have become a standard laboratory tool. Femtosecond spectroscopy experiments provided not only better time resolution, but more importantly, new concepts and new phenomena [1]. Slower processes with characteristic times of nanoseconds or longer are governed by random diffusion of atoms and molecules. On the other hand, on the fs timescale, the coherent nuclear motions of nonequilibrium dynamics are observed. For complex processes, simpler events are resolved and transition states are trapped before thermal fluctuations blur the dynamical picture.

By using the fs pulses as a spectroscopic probe, with light wavelengths ranging from the ultraviolet to the infrared and terahertz, or other emissions such as electrons and ions, a great number of systems and processes in biology, chemistry and physics have been studied. The experiments can probe the evolution of the excited electronic states, such as carrier dynamics in metals and semiconductors, electron transfer in breaking and forming chemical bonds, and charge separation in photosynthetic reactions. But when the process under study involves structural change, only indirect structural information can be obtained, for example from frequencies of nuclear vibrations measured by infrared (IR) or Raman spectroscopy [2].

On the other hand, static structures with resolution much less than 1 Å are now routinely solved by diffraction methods [3]. X-rays, high energy electrons and neutrons are common sources to use in diffraction experiments. They have wavelengths comparable to the atomic spacing, and are scattered by the atoms to form diffraction patterns in the far field. In theory, the diffraction pattern is the Fourier transform of the atomic structure in real space. By inverse Fourier transform, the structure can be solved from the diffraction pattern. However, only the intensity of the diffraction pattern is detected in general diffraction experiments, whereas the phase of the diffracted beam cannot be recovered. Therefore more complex mathematical methods are needed to solve the complete atomic structures, such as phase retrieve algorithm and direct methods. In crystal diffraction experiments, molecules arrange in an ordered state in crystals and the repeated units give rise to distinct spots in the diffraction patterns, which makes it easier and more accurate to solve the atomic

structures.

It is natural to see if one can combine the femtosecond time resolution of the ultrafast experiments and the sub-ångström spacial resolution of the diffraction techniques to study the structural dynamics directly. In femtosecond spectroscopy experiments, one general method is the pump-probe configuration. As in a movie, a continuous motion can be broken up into frames and captured with a brief exposure time. In the pump-probe femtosecond spectroscopy experiments, a femtosecond laser pump pulse initiates the process under investigation, and defines an exact time zero,  $t_0$ . Then another femtosecond laser pulse with different wavelength is used as a probe pulse, which arrives at the sample at some later point in time and provides a snapshot of the status of the process at that time. A full sequence of the dynamical process is achieved by using a precisely timed series of these probe pulses. And the individual snapshots combine to produce a complete picture of the continuous time evolution. For ultrafast diffraction experiment, the same method can be used only with a pulsed diffraction source as the probe.

Within the common sources used in the diffraction experiments, X-rays have wavelengths from 2.28 to 0.71 Å with an X-ray tube, and sub eV up to the MeV range with synchrotron radiation. The high energy electrons used in transmission electron microscopy have energies mostly in the range of 100 to 400 keV; with high voltage electron microscopes this range extends to 1 MeV or more. The neutrons used are usually the thermal neutrons from nuclear reactors with average energy  $\sim 0.025$  eV and corresponding wavelength  $\sim 1.5$  Å [3]. X-rays are scattered mostly by the electrons of the atoms, and the diffraction patterns are given by the Fourier transform of the total distribution of electrons. Electrons are scattered by both the electrons and the nucleus of the atoms, or by the potential field of the atoms, so the scattering amplitude is much larger for electrons, six orders of magnitude larger compared to that of X-rays. Neutrons are scattered by nucleus. Although the scattering amplitude for neutrons is small compared to both X-rays and electrons, it does not vary much with atomic weight. This makes neutrons attractive in detecting the positions of light elements, such as hydrogen, in the structure.

All three sources have been used in time-resolved experiments [4]. Especially for the X-rays from synchrotron radiation and the neutrons from the nuclear reactor, the sources are pulsed with pulse duration of nanoseconds. However, only X-rays and electrons have been used for ultrafast diffraction. For recent reviews, see reference [5] for ultrafast X-ray diffraction, and references [6, 7, 8] for ultrafast electron diffraction. Because of the aforementioned larger scattering amplitude, electrons are more sensitive for low density and low dimensional matters, such as gas-phase samples and surfaces. Also, electrons penetrate less and better match the optical penetration depth in most samples. On the other hand, electrons are less damaging to samples for the same diffraction signals (scattering events), especially for biological specimens. The technology for generating, deflecting and focusing the electrons is well developed and allows for “table-top” ultrafast diffraction and imaging experiments. For ultrafast X-ray diffractions, the laboratory size apparatus generates few photons for the diffraction experiments. In contrast, free electron laser (FEL) is very promising, only with very complicated and involved synchrotron technology and the construction is still in progress. There are challenges for ultrafast electron diffraction as well. Space-charge effect in nonrelativistic electron beams limits the electron numbers in the ultrashort pulses and accurate timing on fs timescales can be difficult. However, recent development of single electron diffraction and imaging technique can overcome the space-charge effect and reach fs time resolution [9].

Ultrafast electron diffraction (UED) for gas phase materials has been developed in the Zewail lab at Caltech since the early 1990s and reported on by others [10, 11, 12, 13]. In UED, the ultrafast electron pulses are generated by femtosecond laser pulses through photoelectric effect, and have pulse widths typically in ps with a few thousand electrons per pulse. Because of the homogeneous nature of the gas phase material, the diffraction patterns are composed of concentric rings. The interference is from different atoms in the gas molecules, and the molecular structure (bond distances and angles) can be solved by fitting the one-dimensional curve, which is obtained from radially averaging the diffraction rings. Due to the low density of the gas molecules, the diffraction signals are weak, and the diffraction from the transient species are even

weaker. With tremendous efforts from the researchers here at Caltech, the sensitivity of the UED apparatus is now much improved to allow for the studies of molecules even without heavy atoms [12, 13]. The theoretical analysis and calculations are also highly advanced for better determinations of transient structures, even for complicated large molecules, and for coupling to complex reaction pathways [14, 15, 16]. A number of important photochemical and photophysical problems have been studied, such as the nonconcerted elimination of iodine atoms from  $C_2F_4I_2$  [17, 18], the ring opening of cyclohexadiene ( $C_6H_8$ ) [18, 19] and the ultraviolet excitation of acetylacetone [20, 21]. Recently, the excited-state structures of the aromatic carbonyl molecules benzaldehyde and acetophenone were studied, and a bifurcation of pathways from the excited state was discovered [22, 23].

To study the structural dynamics of surfaces, interfaces, thin films and crystals, ultrafast electron crystallography (UEC) has been developed in this laboratory. Surfaces and interfaces are very important in chemical reactions and nanotechnology. The two-dimensional nature of surfaces and thin films, as oppose to bulk materials, induces interesting physical properties. We are especially interested in studying large molecules, wherein most of them cannot be made into gas phase. The order and repeat units in crystalline sample of the molecules generate three-dimensional diffraction, which allows for determination of the complicated molecular structures, as in steady-state protein crystallography.

In the last five years, UEC apparatus has been designed and assembled in our laboratory. UEC methodology has been developed and demonstrated with many experiments. Semiconductor surfaces were studied as first experiments [24, 25]. Absorbed small molecules, such as water/ice on semiconductor surfaces [26], and self-assembled monolayers of alkanethiols and thio-derivatized hemes on gold surfaces [27], were also studied. Recently, Langmuir-Blodgett films of complicated molecules — fatty acids [28] and phospholipids [29] — were studied, opening the gate to the study of biomolecules.

In the following chapters, the development of the UEC technique and its applications will be reported. Chapter 2 gives a detailed description of the UEC appa-

ratus and the experimental operations with the apparatus. Chapter 3 explains the methodology of UEC, including the experimental aspects and the principles of analysis. Chapter 4 begins the results section with the early experiments on semiconductor surfaces. Studies on adsorbed fatty acids and phospholipids in the crystalline form of Langmuir-Blodgett films are presented in chapters 5 and 6. The steady-state studies of static structure and thermal behavior are described in chapter 5. The structural dynamics studies following a temperature jump induced by femtosecond laser are depicted in chapter 6, based on the static structure determination and are compared to the equilibrium temperature dependence. Chapter 7 concludes the thesis and the perspective of UEC is discussed.

# Chapter 2

## Apparatus \*

The ultrafast electron crystallography (UEC) apparatus in our lab is built for the study of thin crystals and surfaces, based on experience of three generations of gas phase ultrafast electron diffraction (UED). It includes a homemade ultrahigh vacuum (UHV) chamber system, which sits on a supporting frame assembly, and a commercial femtosecond (fs) laser system with optical interfaces (see figure 2.1 and figure 2.2). The fs laser system provides both the laser pulses for the generation of ultrashort electron pulses, and those initiating the reactions to be studied. The UHV chamber system is where the samples are mounted, stored and prepared, and where the experiments take place. It connects to the electron gun and imaging system, where the electron pulses are generated, focused and recorded after they are diffracted by the samples. The experiments are controlled and automated by personal computers with Labview programs developed in UEC laboratory.

### 2.1 UHV chamber system

Since electrons have large scattering cross sections, high vacuum is needed for electrons to travel through without being scattered by the gas molecules. A typical modern transmission electron microscopy (TEM) has a pressure inside the column of  $P \approx 10^{-7}$  torr. However, ultrahigh vacuum (UHV), which refers to pressure  $P$  of  $10^{-9}$  to  $10^{-12}$  torr, is required to carry out the surface experiments. It reduces surface

---

\*This apparatus was constructed in collaboration with Dr. Chong-Yu Ruan, Dr. Franco Vigliotti, and Dr. Vladimir A. Lobastov, see reference [24].

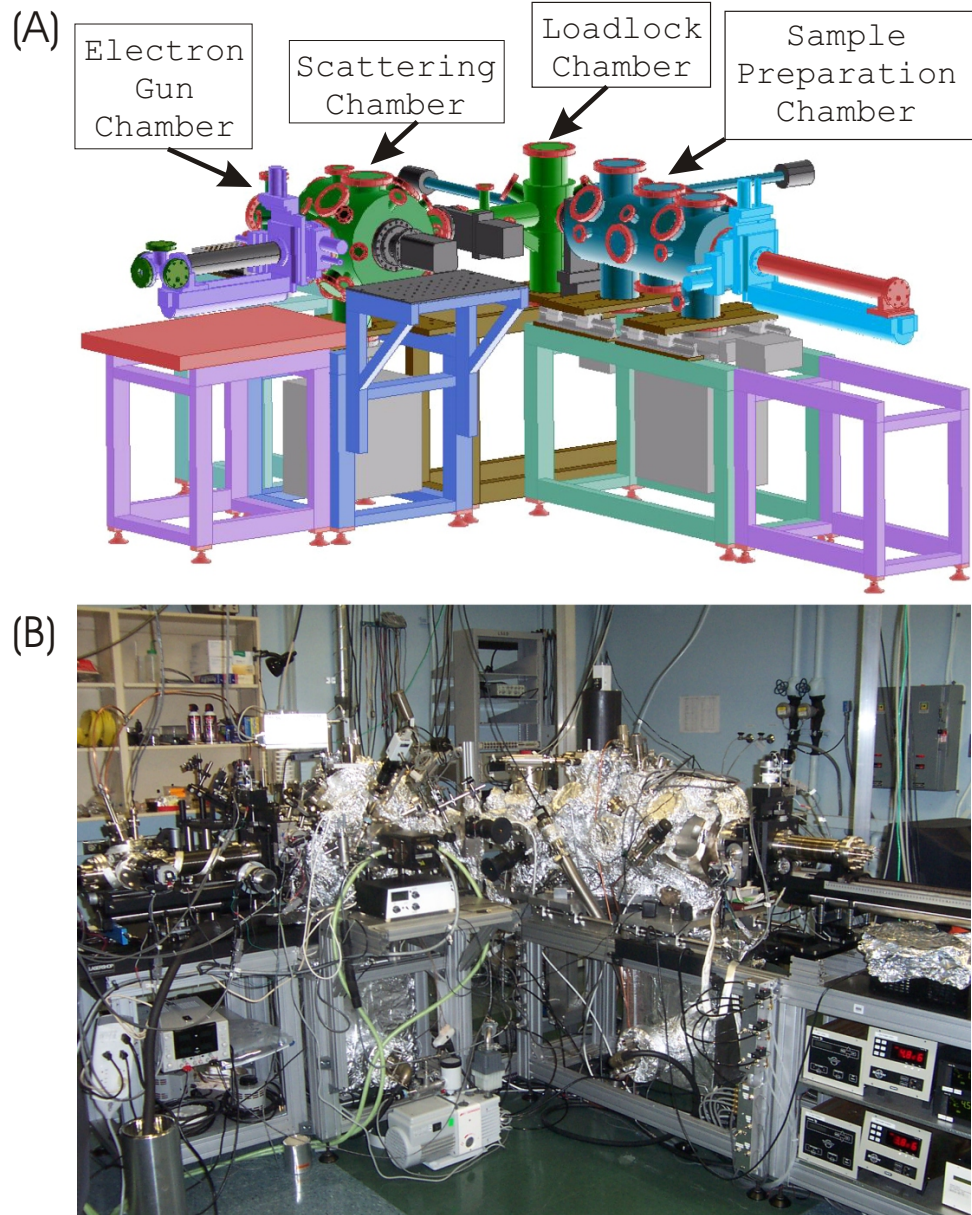


Figure 2.1: The chamber system with frame support: (A) schematic diagram; (B) photo of the same view in the lab.

contamination by reducing the number of molecules reaching the sample over a given time period.

The number of gas molecules hitting the surface per unit time and area is given by

$$\Phi = \frac{1}{4}n\bar{v} \quad ,$$

where  $\bar{v}$  is the average velocity of the gas molecules determined by temperature,  $T$ , and the molecular weight,  $M$ ,

$$\bar{v} = \sqrt{\frac{8RT}{\pi M}} \quad .$$

And  $n$  is the number of molecules per unit volume given by

$$n = \frac{P}{k_B T} \quad .$$

Giving the molar gas constant,  $R$ , and Boltzmann constant,  $k_B$ , the gas impingement flux,  $\Phi$ , is calculated in the unit of  $\text{cm}^{-2}\text{s}^{-1}$

$$\Phi = \frac{P}{\sqrt{mT}} \times 3.51 \times 10^{22} \quad ,$$

where  $P$  is in torr,  $m$  is in amu and  $T$  is in K. The number of adsorption sites, i.e., the number of atoms on the surface, is  $\sim 10^{15} \text{ cm}^{-2}$ . So at  $P \approx 10^{-6}$  torr, it only takes a few seconds for a monolayer to form on the surface. Whereas at  $P$  below  $10^{-9}$  torr, it takes hours or even days for a monolayer to form and effectively reduces the reaction of the sample surface with the gas molecules, thus allowing experiments for the sample surface to be performed.

The chamber system in the UEC lab consists of three integrated main UHV chambers (figure 2.2): the scattering chamber, the sample preparation chamber and the load lock chamber. Two manual gate valves (from MDC Vacuum Products, LLC, Hayward, CA) separate the load lock chamber from each of the scattering chamber and the sample preparation chamber. The scattering chamber is also connected to the electron gun chamber and the CCD (charge-coupled device) imaging system through differential pumping.

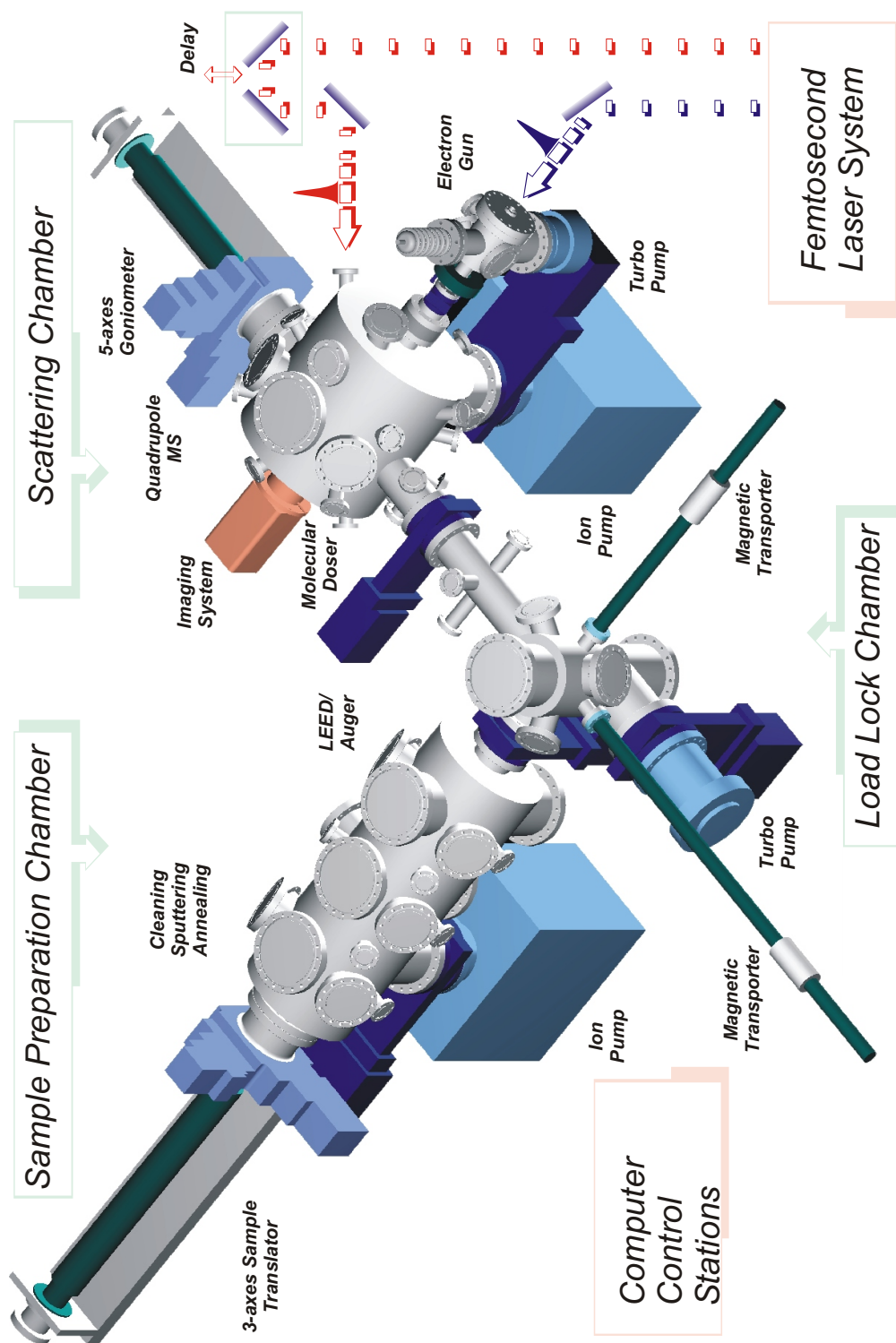


Figure 2.2: Schematic diagram of the experimental setup [24].

There are 3 pumping stages for the main chambers (figure 2.2). The system is rough pumped by a dry mechanical pump (QDP40 Drystar Pump from BOC Edwards, Inc., Wilmington, MA) through a turbomolecular pump (STP451 Seiko Seiki from BOC Edwards, Inc., Wilmington, MA), which is connected through an electropneumatic gate valve (from MDC Vacuum Products, LLC Hayward, CA) to the load lock chamber. This turbo pump provides intermediate pumping for the three main chambers, and can take the load lock chamber alone to low  $10^{-10}$  torr. Two ion pumps connected to the main chambers through electropneumatic gate valves (from MDC Vacuum Products, LLC Hayward, CA) provide fine pumping for the sample preparation chamber and the scattering chamber, respectively. One ion pump (VacIon Plus 500 Diode Ion Pump with Titanium Sublimation from Varian, Inc., Palo Alto, CA) is underneath the scattering chamber. The other ion pump (VacIon Plus 500 Starcell Ion Pump with Titanium Sublimation from Varian, Inc., Palo Alto, CA) underneath the sample preparation chamber has better performance for large amounts of gas. The electron gun chamber and the CCD system are pumped separately and connect to the scattering chamber through differential pumping. The electron gun is pumped by a small turbo pump (Model EXT255H from BOC Edwards, Inc., Wilmington, MA), which is backed by a dry mechanical pump (Model XDS10 from BOC Edwards, Inc., Wilmington, MA). The image intensifier is pumped separately by a mechanical pump (RV5 Rotary Vane Pump from BOC Edwards, Inc., Wilmington, MA). The vacuum is measured by a multigauge system (from Varian, Inc., Palo Alto, CA), which use thermocouple (TC) type gauges for pressure from atmosphere (760 torr) to  $10^{-3}$  torr, and ion gauges for pressure below  $10^{-3}$  torr.

The load lock chamber is used to load the samples from the ambient pressure and store in UHV, and to retrieve the samples from the system. So the sample preparation chamber and the scattering chamber can keep under UHV at most time. It houses a sample cassette (from Transfer Engineering and Manufacturing, Inc., Fremont, CA, see figure 2.3), which has shelves to hold up to 5 sample holders and can be moved up and down by a Z-slide translator underneath. The load lock chamber is relatively small, so the pump down time is fast, usually only takes 4–5 hours to pump from

atmosphere pressure ( $7.6 \times 10^2$  torr) to  $10^{-9}$  torr. With the multiholder cassette, it also allows for minimum exposure of the samples to air before the experiment, and changing samples while the experiment is going on. To mount the sample holders, the load lock chamber is opened by removing the 8" flange on the top and the sample holders are put on the shelves by hand.

The sample preparation chamber is where the sample surface can be prepared *in situ* under UHV and characterized (figures 2.2 and 2.3). It has three sections, and is augmented with LEED/Auger Spectrometer (from SPECS Scientific Instruments, Inc., Sarasota, FL) and sputter cleaning (ion source package and gas inlet system from SPECS Scientific Instruments, Inc., Sarasota, FL) in two sections, with the third one (in the center) open for additional surface techniques. The sample preparation chamber is home to a 3-axis sample translator (from Transfer Engineering and Manufacturing, Inc., Fremont, CA), which allows x, y and z translation of the sample with high precision ( $10 \mu\text{m}$ ). The sample can be moved to different sections, and the position be adjusted for different surface experiments. The sample can also be heated up to  $1000^\circ\text{C}$  through the feed through wires on the sample translator.

The scattering chamber is where the ultrafast diffraction experiments take place (figure 2.2). It connects to the electron gun chamber and the CCD assembly through differential pumping. It encases a 5-axis goniometer (from Transfer Engineering and Manufacturing, Inc., Fremont, CA) on which the sample is mounted, giving the sample high precision in x, y and z translation and in rotation of  $\theta$  and  $\phi$  ( $10 \mu\text{m}$  in translation and  $0.01^\circ$  in rotation), as shown in figure 2.4. The goniometer head (figure 2.4(B)) has two sections, one is the stage for the sample holder and the other has three needles for alignment purposes. For the goniometer, x-axis is along the horizontal direction to the load lock chamber, y-axis is pointing up along the vertical direction, and z-axis is horizontal along the direction from electron gun chamber to the CCD camera. The rotation in the sample plane around the normal of the sample surface is represented by  $\phi$ . And the out-of-plane rotation around x-axis is represented by  $\theta$ . Note that in the figure, the sample holder is in the horizontal position where the y-axis and the axis for  $\phi$  rotation (the normal of the sample surface) is

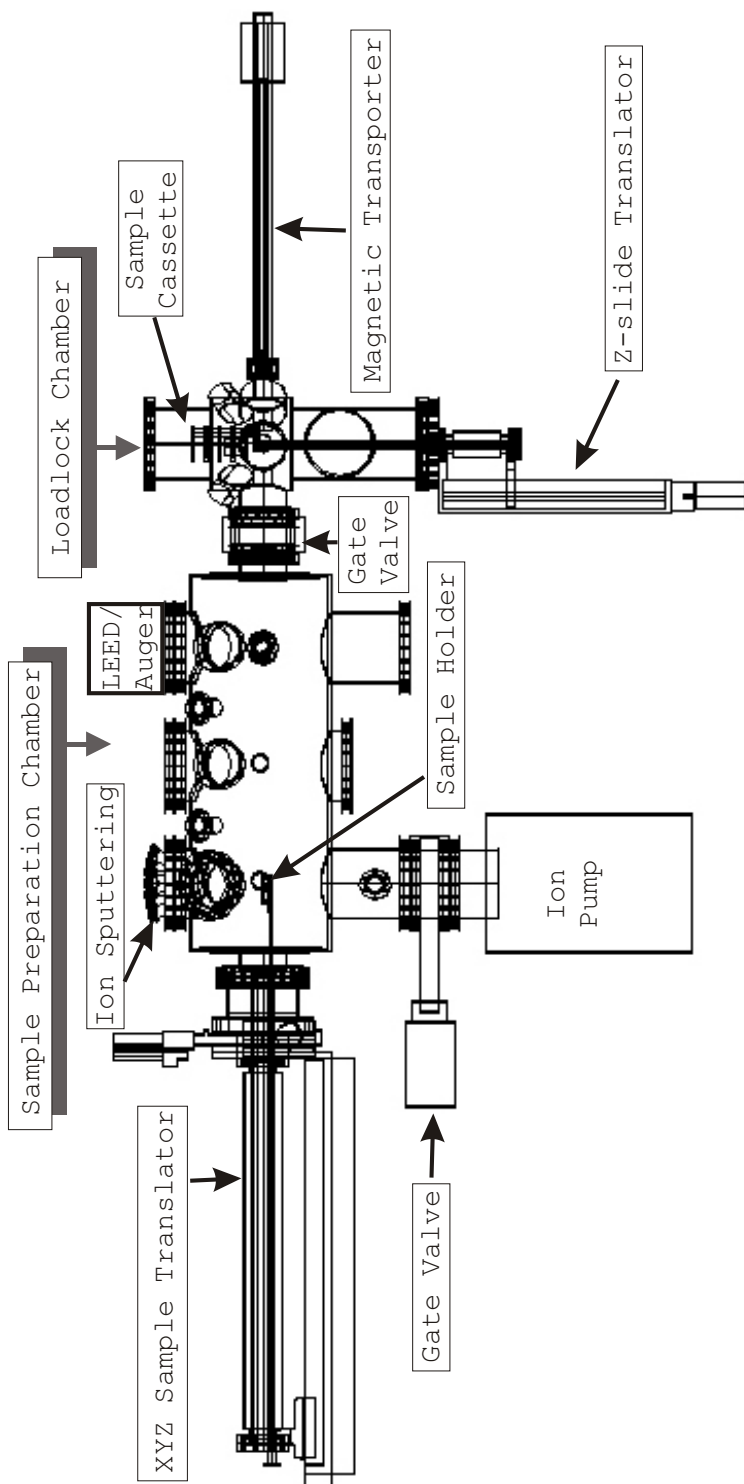


Figure 2.3: Schematic side view of the sample preparation chamber and the load-lock chamber.

the same. In experiments, depending on  $\theta$ , these two axes usually are not the same. The sample holder can be heated to over 200°C through the wires on the goniometer head, and cooled down to  $-180^\circ\text{C}$  through liquid nitrogen ( $\text{N}_2$ ) running in the tubing underneath the stage for the sample holder (not shown in the figure). The temperature of the sample can be measured by the platinum resistance temperature detector (RTD) buried in the stage for the sample holder, or more precisely, using thermocouples directly connected to the sample.

## 2.2 Electron gun system

The ultrafast electron pulses used in the experiments of UEC are generated in the electron gun chamber (see figure 2.2 and figure 2.5) by the fs laser pulses ( $\lambda = 266 \text{ nm}$ ) through photoelectric effect. The photo cathode is made of a thin silver film ( $\sim 45 \text{ nm}$ ) deposited on a sapphire window ( $\sim 16 \text{ mm OD}$  from Rolyn Optics Co. Covina, CA), and is confined in a close-fitting groove on the stainless steel cathode set by conductive silver paste (PELCO Colloidal Silver Paste from Ted Pella, Inc., Redding, CA), which also provides electric contact. The cathode set allows the fs laser illuminate the photocathode from the back through the sapphire window. The anode is made of stainless steel with a gold mesh (Gilder Fine Bar Grids from Ted Pella, Inc., Redding, CA) covered hole at the cathode side to provide a uniform electric field to extract photo-electrons. A  $\mu$ -metal disk (from Magnetic Shield Corporation, Bensenville, IL) on the other side of the anode provides shielding from the electric magnetic field, with a hole of  $150 \mu\text{m}$  diameter to let the electrons pass. The cathode set and the anode are supported and connected to the flange by macor rods, which also serve as electric insulators. The cathode set is connected to the high voltage (30 kV) through vacuum feedthrough, whereas the anode is grounded to the whole chamber system. By adjusting the length of the macor rods, the distance between the cathode and the anode can vary to give different extraction field strength. In our experiments, the field strength is  $30\text{kV}/3\text{mm} = 10 \text{ kV}/\text{mm}$ .

The electron gun chamber is kept in high vacuum with pressure at  $10^{-7}$  torr to

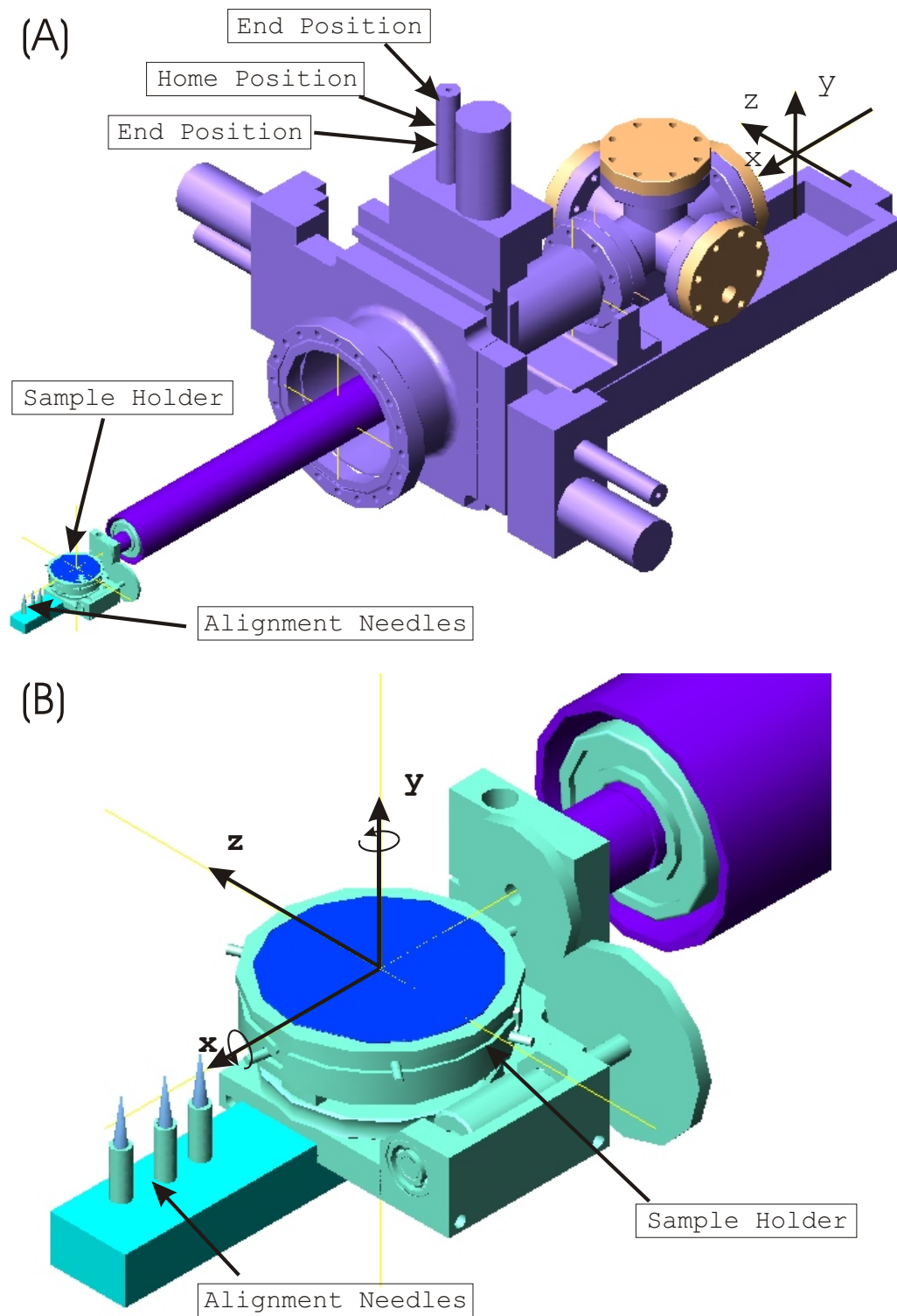


Figure 2.4: Schematic view of the goniometer: (A) the whole body; (B) an enlarged view of the goniometer head. The liquid nitrogen tubing is omitted for clarity.

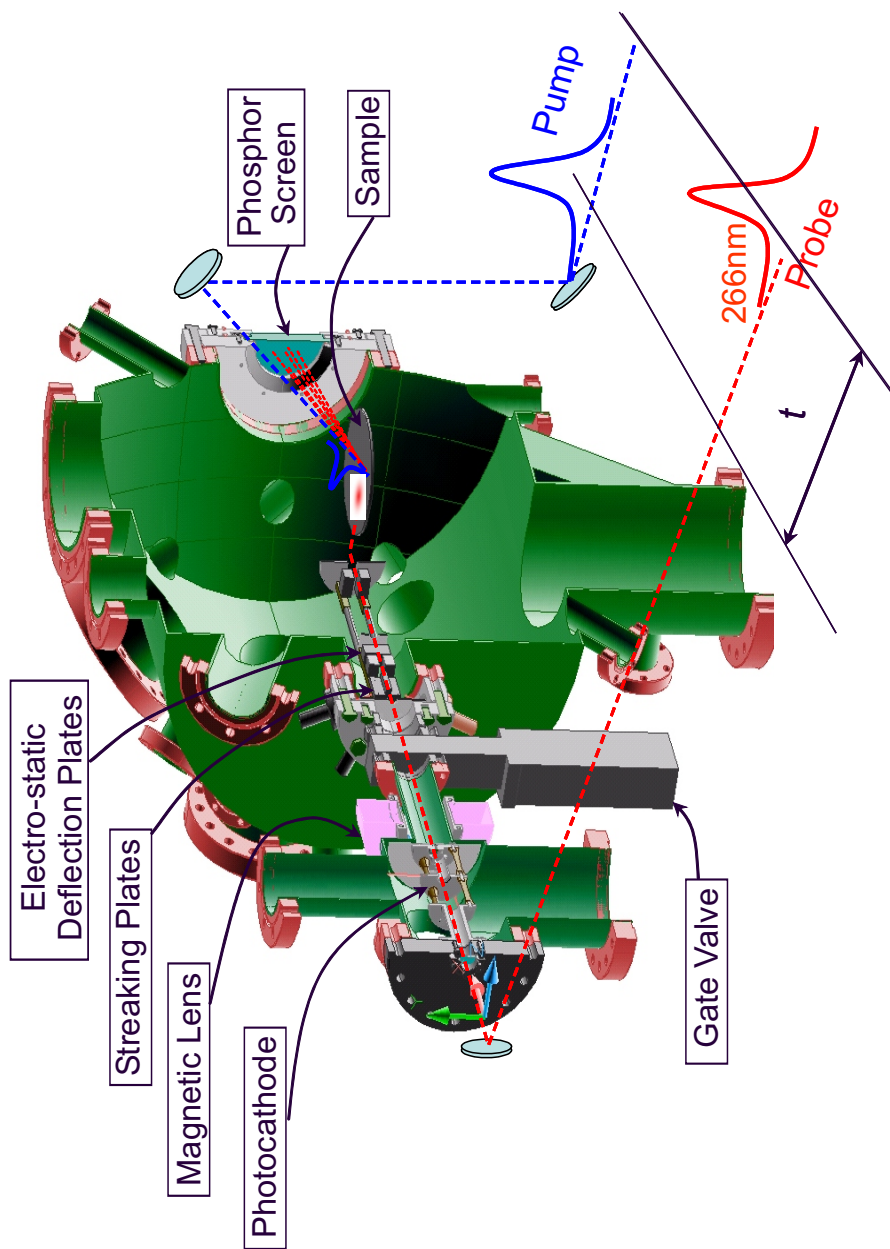


Figure 2.5: A cut through the electron gun chamber and the scattering chamber, showing the paths of the electron pulse and the excitation laser pulse onto the sample. Note that the sample is on the goniometer, which is omitted for clarity. Also the CCD imaging system is omitted; only the phosphor screen is shown.

let the electrons pass without scattered by gas molecules. The high vacuum also provides the insulation between the high voltage (30 kV) cathode and the anode, which is grounded to the rest of the chamber. The electron gun chamber is connected with the scattering chamber through an electropneumatic gate valve (from MDC Vacuum Products, LLC Hayward, CA). When the gate valve is open, a hole with diameter of 5 mm allows the passage of the electrons into the scattering chamber. In the mean time, it keeps the scattering chamber at UHV through differential pumping.

The electrons are focused using a homemade magnetic lens located right after the electron gun chamber. The magnetic lens is a homemade solenoid inside a magnetic coil enclosure (from Magnetic Shield Corporation, Bensenville, IL), and sits outside the vacuum tube where the electron pulses pass (see figure 2.5). It has a weak focusing power on the electrons, with the focusing length determined by the electric current. There are three sets of fine-threaded screws, with two screws in a set at each side of the solenoid, evenly placed around the vacuum tube on the enclosure. By turning the screws, the position and the angle of the magnetic lens can be finely tuned.

There are four sets of electro-static plates inside the scattering chamber. The first set is the streaking plates, used in the streaking experiment to characterize the electron pulses (see section 3.2.1). There are three sets of deflection plates after the streaking plates that can steer the electron beams by electric static force, one in the horizontal direction and two in the vertical direction.

In UEC experiments, the electron pulse is directed onto the sample and scattered to form the diffraction pattern in the far field on the phosphor screen. Figure 2.5 shows the case in reflection mode. In transmission or at low angles in reflection, only some of the electrons get diffracted, and many electrons still go through in the so-called main beam. A beam stopper, which is a grounded metal tube to catch the electron main beam, is put in front of the phosphor screen (not shown in figure 2.5). The beam stopper can be moved around in the plane of the screen through a UHV manipulator system (from MDC Vacuum Products, LLC Hayward, CA).

## 2.3 Imaging system

The electrons and the diffraction patterns are recorded by a homemade intensified CCD imaging system, as shown in figure 2.2 and figure 2.5. Figure 2.6 is a cut view of the CCD imaging system. It is contained in a homemade holder/adaptor. And it consists of four basic components: 1) a phosphor screen (P47 deposited onto fiber-optic faceplate) to convert electrons into photons; 2) a fiber-optic taper (1.5x, from Incom, Inc., Charlton, MA) which optically reduces and transmits the image; 3) an image intensifier (from Hamamatsu Corporation, Hamamatsu City, Japan) to amplify the image signals; and 4) a CCD camera system (Princeton Instruments Medium X-ray Digital CCD Camera System from Roper Scientific, Inc., Trenton, NJ) for digital readout of the image. It is connected to the scattering chamber through a homemade adapter, which houses the imaging system and provides differential pumping between the low vacuum ( $10^{-2}$  torr) required for the image intensifier and the UHV chamber.

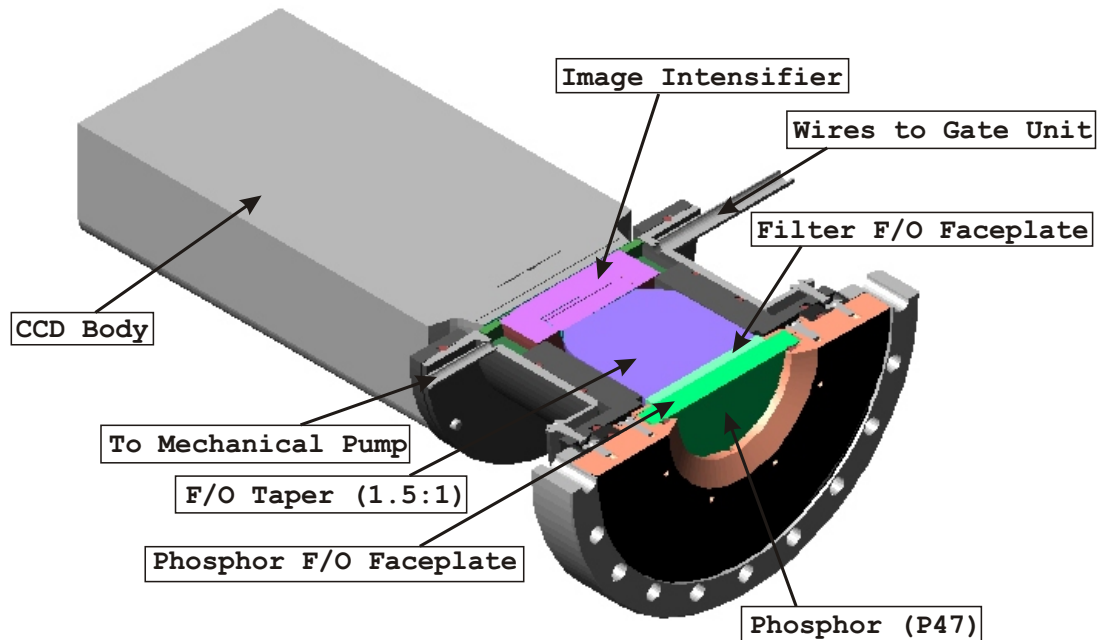


Figure 2.6: A cut through the CCD imaging system.

To minimize the noise generated by the image intensifier, the high voltage is

gated and synchronized to the 1 kHz laser pulse repetition. The image intensifier is controlled by a homemade controller, which provides gated high voltage signals subject to the voltage and the gate width settings.

The CCD camera is a 16-bit digital camera, and the intensity range is 0–65535. It is controlled through a CCD camera controller (from Roper Scientific, Inc., Trenton, NJ) by the software WinView (from Roper Scientific, Inc., Trenton, NJ), which can be programmed using Microsoft Visual Basic or LabView (National Instruments Corporation, Austin, TX). It has 1340 pixels in horizontal direction and 1300 pixels in vertical direction. The pixel size of the CCD camera is measured using a 1951 USAF glass slide resolution target (2" × 2", Edmund Optics, Inc., Barrington, NJ) to be  $44.94 \pm 0.25 \mu\text{m}$  in both horizontal and vertical directions.

## 2.4 Sample translation and manipulation

The samples, with sizes up to 2" in diameter, are placed on the sample holder using either metal (molybdenum) clips or carbon double-sided tape (from SPI Supplies and Structure Probe, Inc., West Chester, PA). The sample holder can be moved under UHV between the load lock chamber and the scattering chamber, and between the load lock chamber and the preparation chamber. The sample holder (from Transfer Engineering and Manufacturing, Inc., Fremont, CA; see figure 2.4(B)) is made of molybdenum or stainless steel, and has six pins distributed evenly at the side. Among the six pins, three pins are at the same lower level while the other three are at higher level.

The sample holder is put on the shelf of the sample cassette in the load lock chamber from the ambient pressure. Under vacuum, the sample holder can be picked up by the magnetic transporter (from Transfer Engineering and Manufacturing, Inc., Fremont, CA; see figure 2.2 and figure 2.3) and moved to the sample preparation chamber. To transfer the sample holder onto the XYZ sample translator in the preparation chamber, the sample holder is placed just above the sample stage of the translator. And then raise the stage until the sample holder sits on top of the stage.

The sample holder can also be transferred between the load lock chamber and the scattering chamber under vacuum, as illustrated in figure 2.2 and figure 2.7. The sample holder is picked up by the magnetic transporter in the load lock chamber and transferred between the sample cassette and the goniometer in the scattering chamber.

As shown in figure 2.4(B), the goniometer head has a sample holder cup, on which the sample holder can sit with its three lower pins fixed through spring-loading in the side groves of the cup. The head of the magnetic transporter is a flipped sample holder cup, with the side groves in the opposite direction (rotation) from the goniometer head cup, which holds the sample holder's three upper pins. To embed the sample holder in the sample holder cup, the sample holder is first put in place (pins inside the groves) by adjusting the position of the goniometer. Afterwards, rotation of the magnetic transporter in one direction will both release the sample holder with the upper pins from the transporter cup and fix it on the goniometer cup through the lower pins. Rotation in the other direction will have the opposite effect, i.e., release the sample holder from the goniometer head and pick it up by the magnetic transporter.

The sample translator in the preparation chamber and the goniometer in the scattering chamber are both driven by stepper motors and automated using LabView programs through electronic control boards. In experiments, the motions are controlled with personal computers through LabView programs.

The ranges in which the translators can travel are restricted by the space of the chambers and the flange sizes. To prevent the translators hit the walls of the chambers, two end positions are set for each translation axis (illustrated for the y-axis stage in figure 2.4), on the axles of the worm gears outside the chamber. The end positions are determined physically when the end plate hit the sensor and triggers the electronic switch. To provide a reference point, a home position is also set for each translation axis within the two end positions. The home position is set through an photoelectric switch where the diode laser is on and sends the beam across two slits. When the edge of the end plate goes through the slits and the beam is blocked, the home signal is given. This provides a very precise home position.

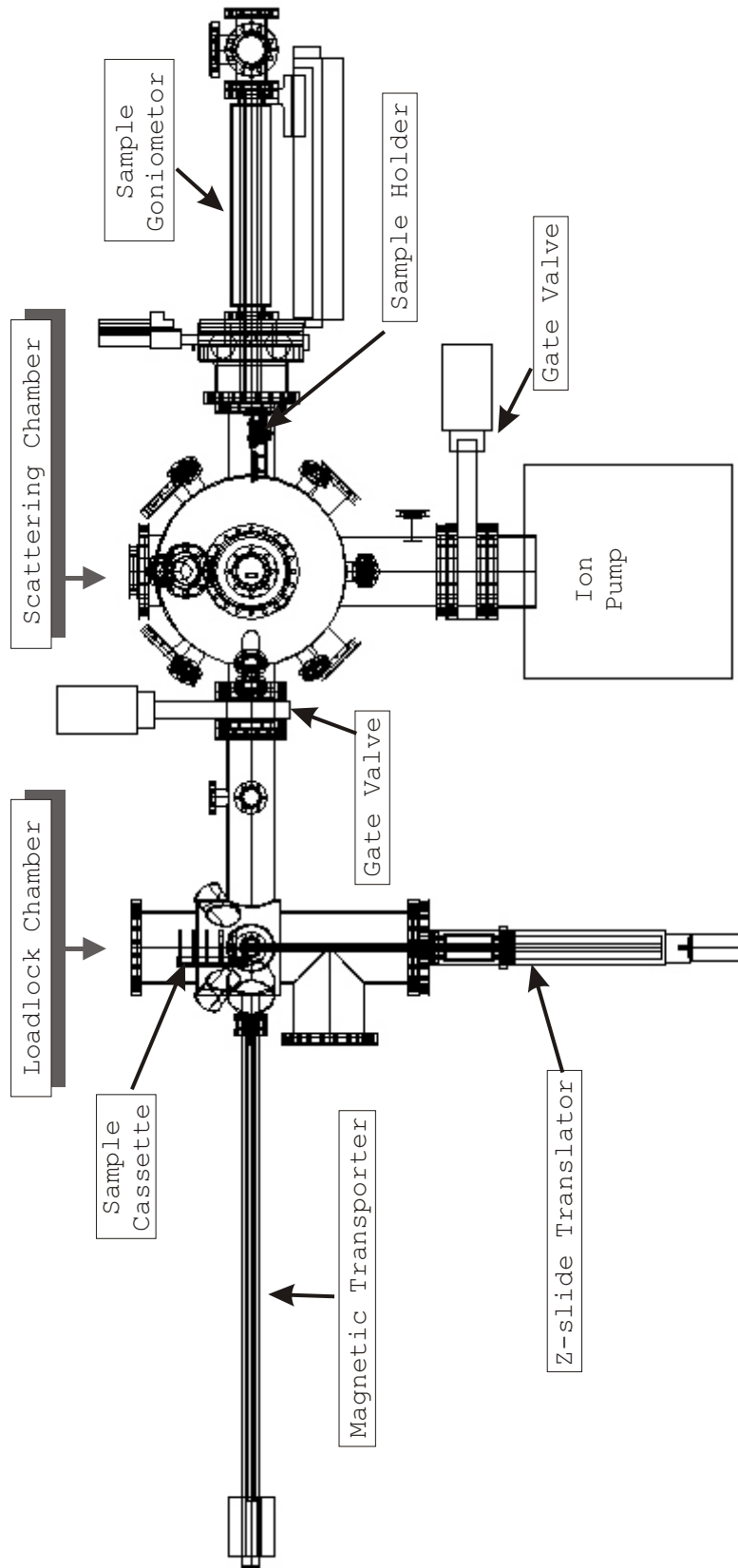


Figure 2.7: Schematic side view of the load lock chamber and the scattering chamber.

The rotations of the goniometer in the scattering chamber are produced through worm gears and worm wheels (figure 2.4(B)). Rotation of  $\theta$  is realized by rotating the tube around the axle inside the tube, and the sample holder is driven to rotate around the axle as well. When the tube is fixed and the wheel #1 is rotated, wheel #2 is driven to rotate around its own axle, and through worm gears and another worm wheel under the sample holder stage, to rotate the sample holder stage with the sample holder around the surface normal and change the  $\phi$  position of the samples. The precision is  $0.01^\circ$  for both the  $\phi$  and  $\theta$  rotation. The  $\theta$  rotation is physically limited by restrictions on the wheel (not shown in figure 2.4(B)) to  $0^\circ$  to  $180^\circ$ . But without the counter balance block (not shown in figure 2.4(B)), the  $\theta$  change should be confined within  $\pm 10^\circ$  around  $90^\circ$ . Outside this region, the precision will be significantly worse. The  $\phi$  rotation is, in principle, without limit. But, because of the presence of the tubes underneath the stage (not shown in figure 2.4(B)), the  $\phi$  rotation is practically restricted to the range of  $\sim 180^\circ$ . The  $\theta$  and  $\phi$  rotations are without reference point in space.  $\theta = 90^\circ$  is set usually to the position where the sample holder is horizontal.

## 2.5 Gas-handling system

To deliver gas adsorbates to the surface in a controlled and quantitative way, a gas-handling system with a microcapillary array beam doser [30] is designed and constructed as shown in figure 2.8. The system contains stainless steel tubes (OD 0.5") connected by Ultra-Torr fitting (from Swagelok Company, Solon, OH) outside the chamber. A homemade stainless steel ballast serves as a gas reservoir of volume  $\sim 1/4$  L. The system can be rough pumped by a mechanical pump and fine pumped by a turbo pump. The inline valves are Nupro 8BG (from Swagelok Company, Solon, OH). A Nupro 4BRG (from Swagelok Company, Solon, OH) controls the flow from the gas bottles and provides some tunability. The gas-handling system connects to the beam doser through a gas feedthrough (from Kurt J. Lesker Company, Pittsburgh, PA) with Cajon VCR fitting inside the chamber.

Figure 2.8(A) shows the design for the microcapillary array beam doser. A stain-

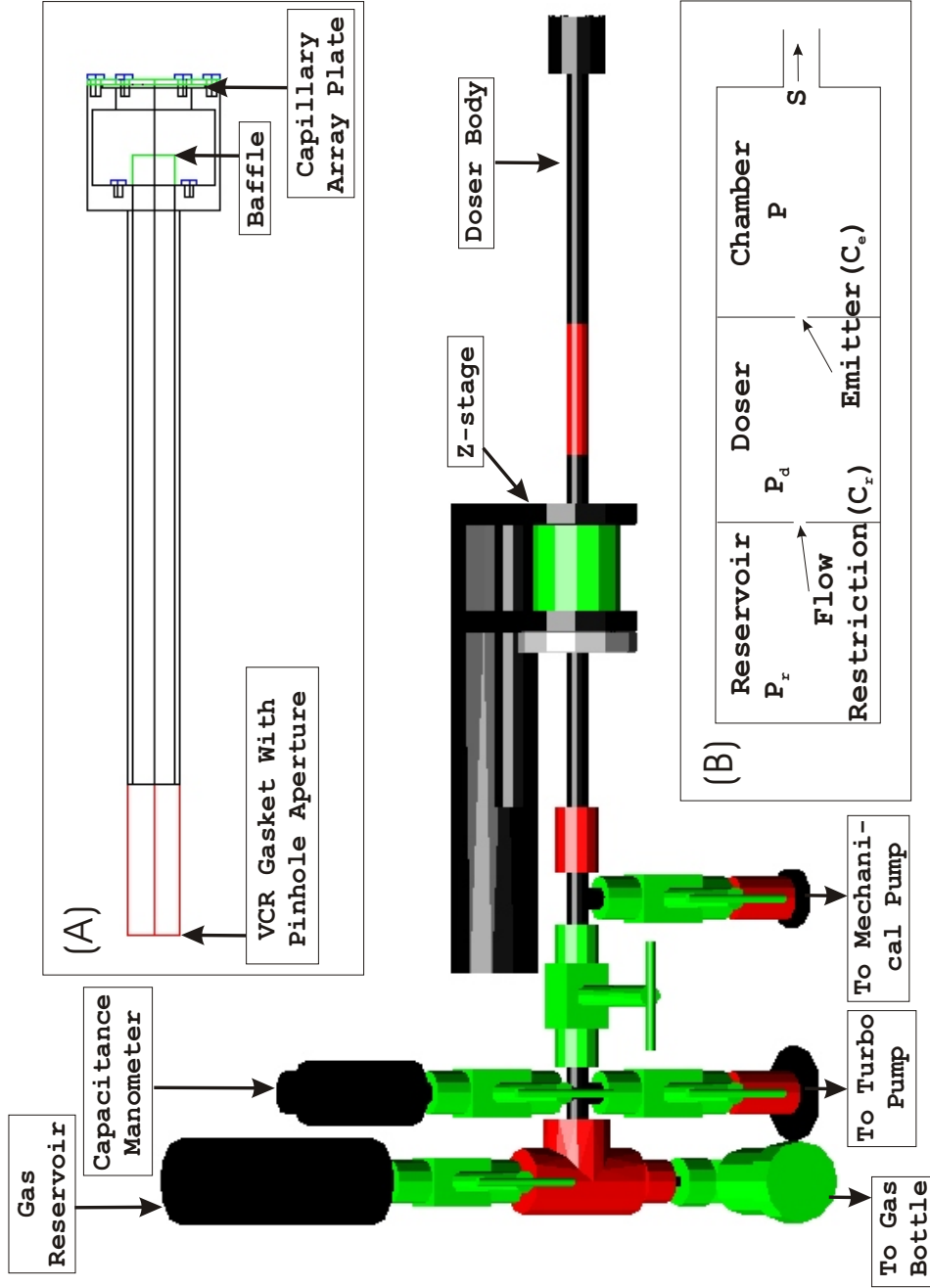


Figure 2.8: Schematic view of the gas-handling system. (A) Sketch of the microcapillary array beam doser. (B) Illustration of the gas flow, here  $P_r$ ,  $P_d$  and  $P$  represent the pressure in the reservoir, doser and chamber, respectively;  $C_r$  and  $C_e$  are the conductance of the flow restriction and the emitter;  $S$  is the pumping speed for the vacuum chamber.

less steel pinhole aperture with 2  $\mu\text{m}$  diameter (Drilled Swagelok VCR gasket from Lenox Laser, Glen Arm, MD) inside the VCR fitting serves as the flow restriction and provides convenient dosing fluxes. The flux of gas travels from the pinhole into the doser body, where it strikes a baffle made of copper shim stock, and the gas molecules' motion is randomized. The baffle is held into the place by the side bending toward the inside wall of the doser body and attached there by two screws. Collimation of the gas occurs in the high density capillary array (glass capillary array plate from Burle Technologies, Inc., Lancaster, PA) with perpendicular capillary size of 10  $\mu\text{m}$  diameter and 800  $\mu\text{m}$  long arranged in a hexagonal close packing arrangement. The capillary plate has a relatively high conductance for gases and is coated with NiCr to avoid charge accumulation. The plate is held in place by a stainless steel cap that, with a clearance of 0.040", confines the edge of the array in a close-fitting groove on the end of the doser body.

To estimate the gas flow quantitatively, the capillary array doser system can be simplified into three parts, reservoir, doser and chamber, as shown in figure 2.8(B). Assume the system in the molecular flow regime, the conductance of the flow restriction is

$$C_r = \frac{\frac{D_r^2}{4} \sqrt{\frac{\pi RT}{2m}}}{1 + \frac{3L_r}{4D_r}} ,$$

where  $D_r = 2 \mu\text{m}$  is the diameter of the pinhole,  $L_r$  is the length of the pinhole and  $L_r \simeq 76 \mu\text{m}$ . For  $D_r$  and  $L_r$  in  $\mu\text{m}$ , temperature,  $T$ , in K, molecular mass,  $m$ , in amu,  $C_r = (2.857 \times D_r^2 \sqrt{\frac{T}{M}} \times 10^{-7}) / (1 + \frac{3L_r}{4D_r})$  in the unit of 1/s. And it gives  $C_r = 4.438 \times 10^{-8}$  1/s for Nitrogen gas ( $\text{N}_2$ ) at room temperature ( $T = 300$  K). The same equation can be used also for calculating the conductance of the emitter, i.e., the capillary array plate, with  $D_r$  replaced by  $D_e$ , the diameter of the whole capillary area,  $D_e = 18$  mm; and  $L_r$  by  $L_e$ , the pore length, i.e., the thickness of the plate  $L_e = 800 \mu\text{m}$ . And it gives  $C_e = 293$  1/s for Nitrogen gas ( $\text{N}_2$ ) at room temperature ( $T = 300$  K).

The gas emitting flux, i.e., the number of gas molecules emitted from the doser in

every second, is given by

$$N_{tot} = \frac{C_e P_d}{k_B T} \quad . \quad (2.1)$$

In the experiment, a fraction of it  $F N_{tot}$  is intercepted by the sample, where the factor  $F$  is determined by the geometry arrangement of the doser emitter and the sample [31]. Let  $S_t$  denotes the sticking coefficient, the number of molecules absorbed on the sample surface is  $S_t F N_{tot}$ , and  $(1 - S_t F) N_{tot}$  molecules get into the chamber. At equilibrium, the rate of the molecules entering the chamber is the same as that of the molecules leaving, i.e.,

$$(1 - S_t F) N_{tot} = \frac{S P}{k_B T} = (1 - S_t F) \frac{C_e P_d}{k_B T} \quad , \quad (2.2)$$

where  $S$  is the pumping speed and  $S = 500$  l/s in the scattering chamber.

An enhancement factor  $E$  is defined as the ratio of the number of total gas molecules hitting the sample surface to the number of those from the background pressure, which is

$$N_{bg} = A P \sqrt{\frac{N_A}{2\pi m k_B T}} \quad ,$$

where  $A$  is the area of the sample surface. The definition of the enhancement factor gives  $E = 1 + \frac{F N_{tot}}{N_{bg}}$ . From equation (2.2), we can get

$$P = P_d \frac{(1 - S_t F) C_e}{S} \quad .$$

So  $E$  is given by

$$E = 1 + \frac{F}{1 - S_t F} \times \frac{S}{A} \times \sqrt{\frac{2\pi m}{RT}} \quad .$$

For  $S$  in l/s,  $A$  in cm<sup>2</sup>,  $m$  in amu and  $T$  in K,

$$E = 1 + 0.275 \times \frac{F}{1 - S_t F} \times \frac{S}{A} \times \sqrt{\frac{m}{T}} \quad .$$

One geometry used in our experiments is the sample has a radius of approximately 5 mm and the distance between the capillary array plate to the sample is about 9 mm,

which yields  $F = 0.6$  [31]. Assuming a sticking coefficient  $S_t = 0.5$  at low temperature  $T = 100$  K, we obtain an enhancement factor of  $\sim 65$  for water vapor.

As shown by equation (2.1), the number of gas molecules emitted from the gas doser, and hence the number of those absorbed by the sample surface are determined by the pressure in the doser  $P_d$ . And  $P_d$  is given by the pressure in the reservoir  $P_r$ ,

$$P_d = \frac{C_r P_r}{C_r + \frac{C_e S}{C_e + S}} .$$

By tuning  $P_r$ , the dosing flux can be precisely controlled. In our setup,  $P_r$  is monitored accurately by a capacitance manometer (Baratron from MKS Instruments, Inc., Wilmington, MA). For the aforementioned case of water vapor at low temperatures, a flux of  $5.1 \times 10^{10}$  molecules per second is obtained for  $P_r = 1$  torr, and the corresponding back pressure in the chamber is  $1 \times 10^{-10}$  torr.

## 2.6 Femtosecond laser system

A commercial amplified femtosecond laser system is used in UEC to provide two laser beams, one to generate ultrashort electron pulses and the other to excite the sample and initiate the dynamics.

The femtosecond laser pulses with wavelength centered at 800 nm and repetition rate of 80 MHz, are first generated by a mode-locked Ti:sapphire oscillator Spectra-Physics Tsunami (from Spectra-Physics Lasers, a Division of Newport Corporation, Mountain View, CA), which is pumped by a continuous-wave (cw) diode-pumped laser Spectra-Physics Millennia (from Spectra-Physics Lasers, a Division of Newport Corporation, Mountain View, CA). These laser pulses are then amplified in a 1 kHz Ti:sapphire amplifier Spectra-Physics Spitfire (from Spectra-Physics Lasers, a Division of Newport Corporation, Mountain View, CA), which is pumped by a diode-pumped, Q-switched Nd:YLF laser Spectra-Physics Evolution-30 (from Spectra-Physics Lasers, a Division of Newport Corporation, Mountain View, CA), to yield an output pulse energy of  $\sim 2$  mJ with pulse length  $\sim 120$  fs. The output fs laser

pulses are monitored by a single shot autocorrelator (Model SSA from Positive Light, Los Gatos, CA).

To generate the ultrashort electron pulses, the fs laser pulses with wavelength of 266 nm are used for photo-electric process in the electron gun chamber (see figure 2.5). As shown in the optics layout in figure 2.9, depending on the excitation wavelength wanted, part or all of the output from the Spitfire is frequency tripled by a tripler (Model TP-1A from U-Oplaz Technologies, Inc., Chatsworth, CA), with an efficiency  $\sim 10\%$  for 3 mJ input. Neutral density filters are used to deliver different powers to the photocathode, therefore to control the electron number and pulse length of the ultrashort electron pulses (see section 3.2.1).

The excitation laser pulses can be 800nm, 266nm or any wavelength from the Optical Parametric Amplifier (OPA-800CF-1 from Spectra-Physics Lasers, a Division of Newport Corporation, Mountain View, CA), which can provide laser wavelength from 1.1 to 3.0  $\mu\text{m}$  with pulse-width  $\sim 130$  fs. The delay line is chosen to be in the path of the excitation through the translation stage (ATS150 series stage with 250 mm of travel from Aerotech, Inc., Pittsburgh, PA), because it is more precise to determine the relative timing of the optical pulses by the distance it travels, compared to determining the relative timing of the electron pulses. As shown in figure 2.9, it is designed so the excitation lasers with different wavelengths can use the same delay stage and go through the same optical path afterwards into the scattering chamber. When doing experiments under different wavelengths, the appropriate mirrors and lenses need to be added or changed to suit specific wavelength, while their positions only need to be adjusted slightly with the help of pinholes on the way. The optical path is experimentally determined to match the time deference between laser pulses of different wavelengths, in order to keep the time zero between the excitation laser and the electron pulses similar regardless of the wavelength of the excitation.

For example, to use 800nm excitation, 80% of the beam is reflected through BS2 (BS1 is removed from the beam path, see figure 2.9) from the output of the Spitfire before it enters the tripler, and sent into the chamber through the delay line. The rest 20% of the beam is frequency tripled and follow the beam path to the photocathode.

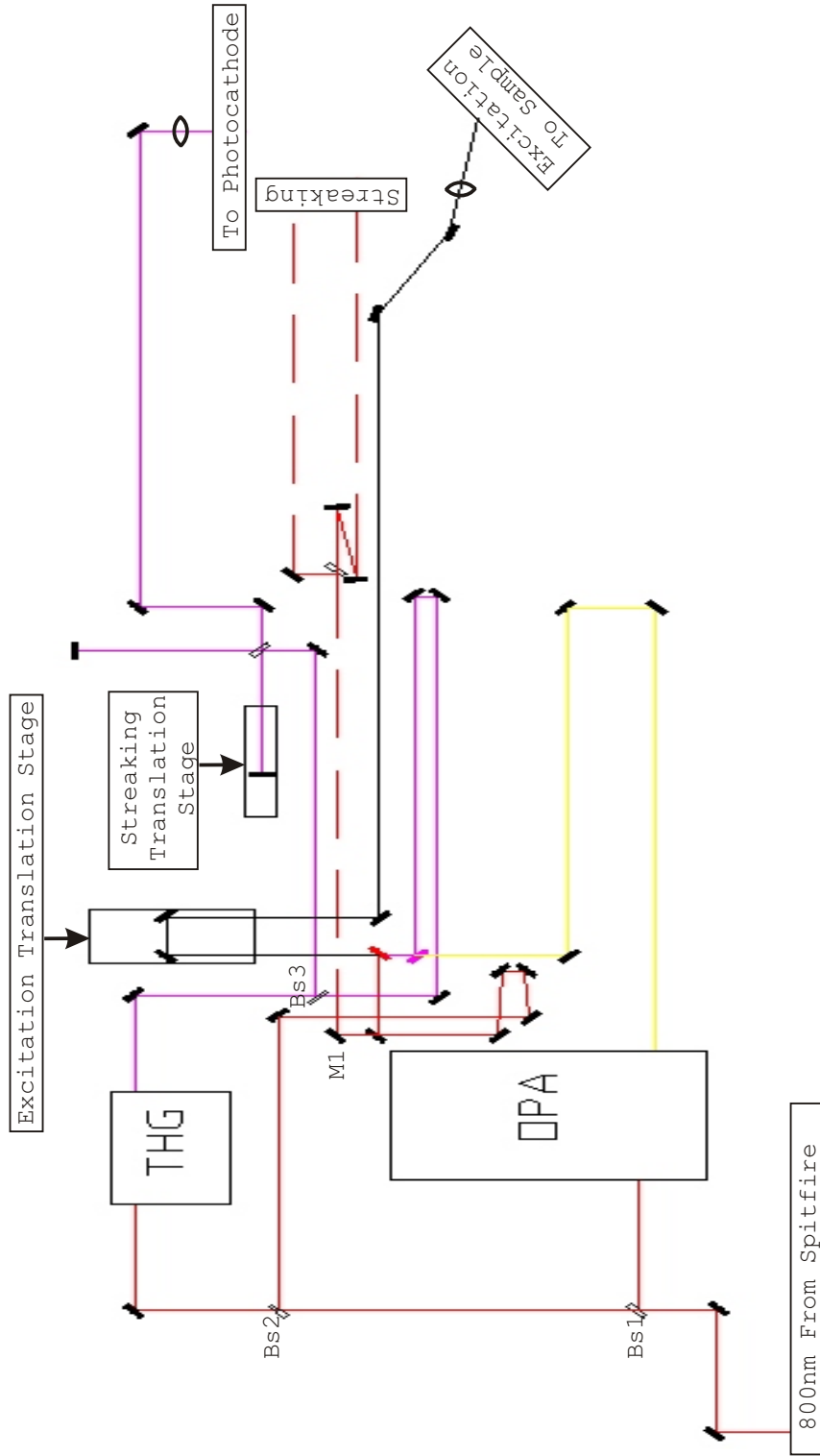


Figure 2.9: The optics layout.

For 266nm excitation, both BS1 and BS2 are removed and all the output of the Spitfire is frequency tripled. Then 50% of the beam is split through BS3 from the output of the tripler as excitation.

To minimize the damage caused by the fs excitation laser on the sample, an electronic shutter (IES electronic shutter with 1.6–25.4 mm clear aperture from Melles Griot, Inc., Rochester, NY) is used at the output of the Spitfire (not shown in figure 2.9). The shutter is synchronized with the CCD camera and controlled to open only when acquiring images.

The optics layout (figure 2.9) also contains the optical path for the streaking experiment, which characterizes the ultrashort electron pulses (see section 3.2.1). Instead of traveling into the scattering chamber as excitation, the 800nm laser is redirected by M1 to provide two pulses simultaneously to activate the two photoconductive switches in the streaking circuit (see section 3.2.1 and figure 3.4). The 266nm laser goes through a Michelson interferometer and gives two pulses in sequence with adjustable delay,  $\tau$ , between them, to generate from the photocathode an identical pair of ultrashort electron pulses with delay  $\tau$ . Additional to the streaking experiment, this configuration can also be used to do autocorrelation of the electron pulses [32].

# Chapter 3

## Methodology

### 3.1 Electron crystallography

The electron wave function  $\Psi(\vec{r}, t)$  satisfies the Schrödinger wave equation,

$$-\frac{\hbar^2}{2m}\nabla^2\Psi + V(\vec{r})\Psi = i\hbar\frac{\partial\Psi}{\partial t} \quad . \quad (3.1)$$

In free space the potential  $V(\vec{r}) = 0$ , the electron energy eigenfunction has the form of a plane wave propagating in the direction of wave vector  $\vec{k}$  as

$$\Psi = \Psi_0 \exp(2\pi i(\vec{k} \cdot \vec{r} - \omega t)) \quad , \quad (3.2)$$

where  $h\omega = E$  is the electron kinetic energy and  $k = 1/\lambda$  is the electron wave number.

In high-energy electron diffraction studies, the electrons used have velocity between  $0.1c$  and  $0.99c$ , where  $c$  is the speed of light and the relativistic effects are not negligible. Equation (3.1) can be corrected for relativistic effects by replacing the electron rest mass by its relativistic mass, and the energy  $E$  by  $E \left(\frac{m_0}{m}\right) \left(1 + \frac{E}{2m_0c^2}\right) = \frac{h^2k_0^2}{2m}$ , where  $\vec{k}_0$  is the relativistic wave vector. The wavelength  $\lambda$  is thus given by

$$\lambda = \left[ \frac{2m_0E}{h^2} \left( 1 + \frac{E}{2m_0c^2} \right) \right]^{-1/2} = \frac{12.2643}{\sqrt{E + 0.97845 \times 10^{-6} E^2}} \quad . \quad (3.3)$$

In our UEC experiment, the electrons generated from the electron gun have energy  $E = 30$  keV, and their wavelength is  $\lambda = 0.0698$  Å from equation (3.3).

For an incident plane wave of the form (3.2), in the kinematic approximation, the wave function at a distance far from the sample ( $r \gg r'$ ) is [3, 33, 34]

$$\Psi(\vec{r}) \approx \Psi_0(\vec{r}) + \frac{\exp(2\pi i k_0 r)}{r} f^{(B)}(\vec{k}, \vec{k}_0) \quad ,$$

where  $f^{(B)}(\vec{k}, \vec{k}_0) = f^{(B)}(\vec{k} - \vec{k}_0)$  is the Born or the kinematic scattering amplitude given by the Fourier transform of the potential  $V(\vec{r})$ ,

$$f^{(B)}(\vec{q}) = -\frac{m}{2\pi\hbar^2} \int V(\vec{r}') \exp[-2\pi i \vec{q} \cdot \vec{r}'] d\vec{r}' \quad ,$$

here  $\vec{q} \equiv \vec{k} - \vec{k}_0$ . The space spanned by all  $\vec{q}$  is the reciprocal space, in respect to the real or direct space of  $\vec{r}$ .

In principle, if the Born scattering amplitude could be obtained from the diffraction experiment, an inverse Fourier transform would give the real space potential distribution. Since the potential is generated by the electrons and nuclei, the position of the atoms in real space could then be solved. However, in real experiments, only the intensity of the electron beam is obtained, i.e., only  $|\Psi^*(\vec{r})\Psi(\vec{r})|$  is known, and the phase of the diffracted beams cannot be directly obtained. There are considerable efforts to solve for the phase by indirect experimental and mathematical methods.

For a single atom, the atomic scattering factor  $f^{(e)}(s)$  is the Fourier transform of the atomic potential  $\varphi(\vec{r})$ ,

$$f^{(e)}(s) = \frac{2\pi m e}{h^2} \int \varphi(\vec{r}) \exp(2\pi i \vec{q} \cdot \vec{r}) d\vec{r} \quad ,$$

where  $s = 2\pi |\vec{q}|$  is conventional for gas diffraction. The atomic scattering factor is tabulated in the International Tables for Crystallography. Alternatively, it can be calculated using an analytical fit of the form

$$f^{(e)}(s) = \sum_{j=1}^n a_j \exp(-b_j s^2) \quad ,$$

where  $a_j$  and  $b_j$  are fitting parameters, and  $n=3, 4$  and  $5$  has been used in literature

[34].

For a collection of atoms such as molecules or a unit cell in the crystal, if the effect of redistribution of valence electrons due to chemical bonding is neglected, the kinematic amplitude of scattering is given by the Fourier transform of the sum of the potential field from single atoms,

$$F(\vec{q}) = \sum_j f_j^{(e)}(s) \exp(-2\pi i \vec{q} \cdot \vec{r}_j) \quad . \quad (3.4)$$

And the diffracted electron intensity is given by

$$I(\vec{q}) = F^*(\vec{q})F(\vec{q}) = \sum_i \sum_j f_i^*(s) f_j(s) \exp[2\pi i \vec{q} \cdot (\vec{r}_i - \vec{r}_j)] \quad . \quad (3.5)$$

Gases, liquids and amorphous solids are statistically isotropic. They are described by interatomic distances  $\vec{r}_{ij} = \vec{r}_i - \vec{r}_j$ , which can be assumed to take all orientations in space with equal probability. The diffracted intensity given by the time-averaged, spherically symmetrical distribution is

$$I(q) = \sum_i \sum_j f_i^*(s) f_j(s) \frac{\sin sr_{ij}}{sr_{ij}} \quad .$$

This is the Debye scattering equation. The sum of the terms with  $i = j$  is the so-called atomic scattering background, which is a smoothly falling intensity from all atoms considered separately,  $\sum_i |f_i(s)|^2$ . The sum of the terms with  $i \neq j$  give oscillations of the molecular scattering denoted by  $I_m(s)$ , experimentally obtained by subtraction of the smooth background. The Fourier transform of this function gives the radial distribution function

$$D(r) = \int_0^\infty s I_m(s) \sin(sr) ds \quad ,$$

which directly shows the distribution of probabilities for the occurrence of the interatomic distance  $r$ , weighted by the scattering strengths of the contributing atoms. From this, the interatomic distances and hence the structure may be derived.

In a crystal, a unit cell is repeated in a periodic array in three dimensions. The unit cell may contain single atom, group of atoms or molecules. Let  $\phi(\vec{r})$  denotes the potential in the unit cell, the potential of the entire crystal is then given by

$$V(\vec{r}) = \sum_{n_1} \sum_{n_2} \sum_{n_3} \phi(\vec{r} - n_1\vec{a} - n_2\vec{b} - n_3\vec{c}) \quad ,$$

where  $\vec{a}$ ,  $\vec{b}$  and  $\vec{c}$  are the lattice vectors. The kinematic scattering amplitude is the Fourier transform of this potential, namely

$$f(\vec{q}) = F[\phi(\vec{r})] \times F[L(\vec{r})] = \frac{1}{\Omega_0} F(\vec{q}) \sum_h \sum_k \sum_l \delta(\vec{q} - h\vec{a}^* - k\vec{b}^* - l\vec{c}^*) \quad , \quad (3.6)$$

where  $\Omega_0$  is the volume of the unit cell, and  $F(\vec{q})$  is the kinematic scattering amplitude of the unit cell.  $F(\vec{q})$  is called the structure factor and given by equation (3.4), where the summation is performed over all the atoms in the unit cell. The vectors  $\vec{a}^*$ ,  $\vec{b}^*$  and  $\vec{c}^*$  are called reciprocal lattice vectors, and related to the lattice vector  $\vec{a}$ ,  $\vec{b}$  and  $\vec{c}$  by

$$\vec{a}^* = \frac{\vec{b} \times \vec{c}}{\vec{a} \cdot (\vec{b} \times \vec{c})}, \quad \vec{b}^* = \frac{\vec{c} \times \vec{a}}{\vec{a} \cdot (\vec{b} \times \vec{c})}, \quad \vec{c}^* = \frac{\vec{a} \times \vec{b}}{\vec{a} \cdot (\vec{b} \times \vec{c})} \quad .$$

The equation (3.6) describes a three-dimensional lattice in the reciprocal space. It can be interpreted in the following way. The diffracted amplitude has a nonzero value only when  $\vec{q}$  coincides with one of the vectors

$$\vec{g} = h\vec{a}^* + k\vec{b}^* + l\vec{c}^* \quad . \quad (3.7)$$

This is known as the Laue condition. The three indices  $h$ ,  $k$  and  $l$ , when having no common factors larger than 1, are called Miller indices.  $(hkl)$  denotes the family of lattice planes perpendicular to  $\vec{g}$ , and the space between the planes is equal to  $d = 1/|\vec{g}|$ . The notation  $\{hkl\}$  denotes all planes that are equivalent to  $(hkl)$  by the symmetry of the crystal. In addition,  $[hkl]$  denotes a direction in the basis of the direct lattice vectors instead of the reciprocal lattice, and  $\langle hkl \rangle$  denotes all

directions that are equivalent to  $[hkl]$  by symmetry.

Another commonly used interpretation for diffraction from the crystals is Bragg's law. It views the diffracted waves as scattered from different crystallographic planes and construction interference occurs when

$$2d_{hkl} \sin \theta = n\lambda \quad ,$$

where  $\theta$  is the angle between the incident wave and the family of lattice planes  $(hkl)$  and  $d$  is the distance between the planes. And the angle,  $\theta$ , which satisfies this equation is called the Bragg angle. It is easy to show that Bragg's law is equivalent to the Laue condition.

The geometry of the diffraction pattern formation can be expressed by the Ewald sphere construction in reciprocal space as shown in figure 3.1(A). The wave vector  $\vec{k}_0$  of the incident electron beam is drawn from point P to the origin O in the reciprocal space. A sphere of radius  $k$  is drawn centered at P. Then for any point Q on the sphere, the reciprocal vector it represents satisfies the relation  $\vec{q} = \vec{k} - \vec{k}_0$ , where the radial vector from P to Q represents the wave vector  $\vec{k}$  of the diffracted beam. The intensity of this diffracted beam is proportional to  $|f(\vec{q})|^2$ , with  $f(\vec{q})$  as scattering amplitude in the reciprocal space at the point Q. This sphere is called Ewald sphere, and it gives both the directions and intensities for all kinematic diffracted beams from a given incident beam.

In the case of diffraction by a single crystal, the scattering amplitude  $f(\vec{q})$  is given by equation (3.6) and is nonzero only on the node of the reciprocal lattice. That means, the diffracted beams are only in the directions where the reciprocal lattice points lie on the Ewald sphere. It is easy to show that this is the necessary and sufficient criterion for the Bragg or Laue condition. For high energy electrons, the wavelength is short, e.g., 0.0698 Å in our experiment, and the radius of the Ewald sphere is large ( $k = 1/\lambda = 14.33 \text{ \AA}^{-1}$ ) compared to the distance between the adjacent points of the crystal reciprocal lattice, which is on the order of  $0.1 \text{ \AA}^{-1}$ . As shown in figure 3.1, given the spread out of the scattering amplitude and the Ewald sphere

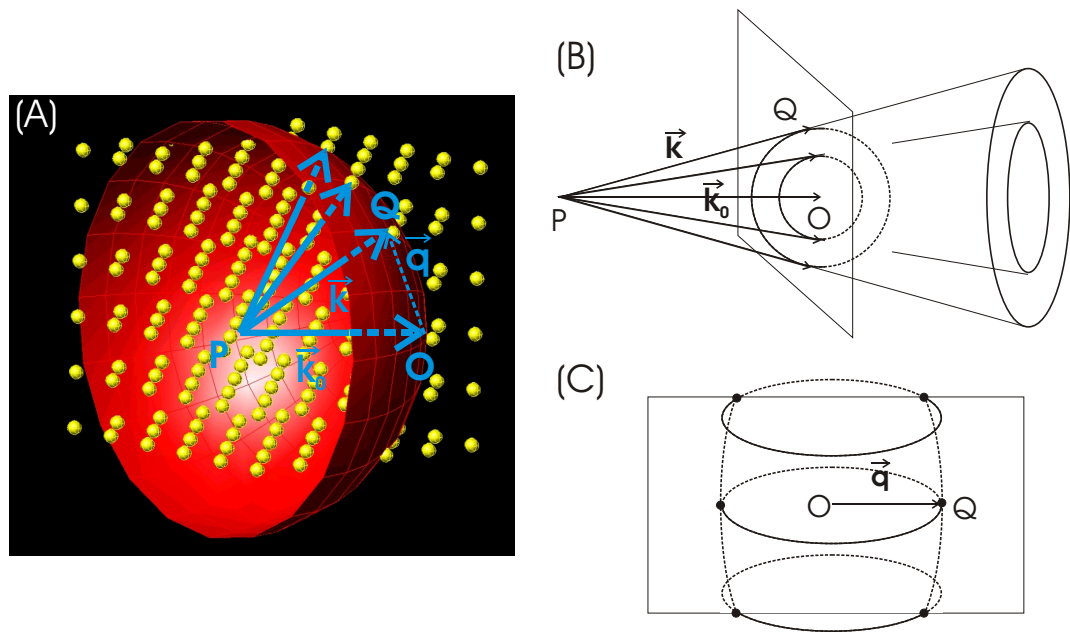


Figure 3.1: Schematic diagrams of the Ewald sphere: (A) for a single crystal in three-dimensional reciprocal space, only half of the Ewald sphere and part of the reciprocal lattice are shown for clarity, also note the reciprocal lattice has intensity modulations as well as systematic absences; (B) for polycrystals; (C) for textured materials.

due to the experimental conditions, a small region around the reciprocal space origin is on the Ewald sphere and represents an almost planar section. The diffraction pattern may thus be recorded on a plane perpendicular to the incident beam and the scatterings which are of interest are predominantly through small angles.

When a diffraction pattern involves multiple electrons, the intensities, not the amplitudes, of individual electron wave function are added. The interactions between different high energy electrons are not coherent [35]. The coherence length of the electron beam is given by the energy and the angular spread [36]. The coherence length of our electrons parallel to the beam direction is given by  $l_{\parallel} = 24.5\sqrt{E}/\Delta E = 420$  nm, estimated from the energy spread of  $\Delta E = 1$  eV and for the electron energy  $E = 30$  keV. The coherence length perpendicular to the beam direction is estimated to be  $l_{\perp} = \lambda/\Delta\theta = 1$  nm from the angular spread  $\Delta\theta = 7 \times 10^{-3}$  rad. The angular spread also affects the coherence length  $l_{\parallel}$  as  $l_{\parallel} = \frac{1}{k \sin \theta_i \Delta\theta} = 57$  nm for incidence angle  $\theta_i = 1^\circ$ , and is the dominant factor.

An ideal polycrystalline material is an assembly of large numbers of randomly oriented crystallites, and is macroscopically isotropic. The effect of randomness is that the reciprocal lattice vectors for a polycrystalline sample lie on a sphere, rather than a set of discrete points for single crystals, as shown in figure 3.1(B). Given by the intersection of these reciprocal spheres with the Ewald sphere, The resulting diffraction pattern is a series of concentric circles around the incident electron direction, which are called Derby-Scherrer rings. Similar to the analysis method introduced previously for gas-phase samples, the radial distribution function for polycrystals can be obtained and gives the distances between the different crystal planes. From these distances, the structure of the crystallites may be derived.

A textured material is a polycrystalline material with intermediate degree of randomness, where the crystallites have some preferential orientation. For example, as often happens in thin films, the crystallites have the same orientation perpendicular to the sample surface, i.e., share a common  $c$ -axis. The reciprocal space representation of such a texture consists of a series of rings, and the intersections of the Ewald sphere with the rings form a pattern of spots lying on a series of ellipses (see figure

3.1(C)).

For crystal surfaces and thin films, the lattice is two-dimensional in the surface plane, while the third dimension perpendicular to the surface is very limited. In reciprocal space, the reciprocal lattice is also two-dimensional, as the lattice points elongate in the out-of-plane direction and become lattice rods (figure 3.2). The crystal surfaces are most stable on the dense packed crystal planes (low-indices crystal planes). The surface crystal structure is usually presented following the crystal bulk structure. But the atoms or molecules on surfaces usually reconstruct or relax due to the truncation of the crystal at surfaces and for different adsorbates presented on the surface.

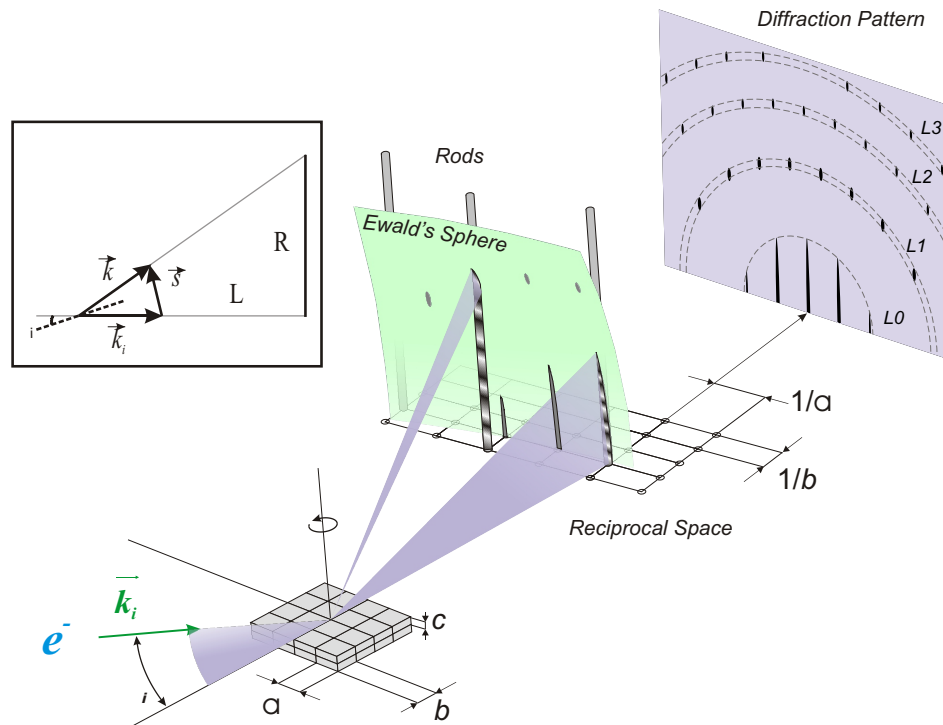


Figure 3.2: Schematic diagram of RHEED experiment, both the Ewald sphere and Laue zones (L0, L1, ...) are displayed [24]. Inset: simplified kinematics of the electron scattering [29].

Because of the large scattering cross section of the electrons, they are ideal for diffraction studies of the surfaces and thin films. When the electron beam incident

at a glazing angle  $\theta_i$ , which is between the electron beam and the sample surface and usually between  $0^\circ$  and  $8^\circ$ , the electrons penetrate only a few atomic layers into the sample and the diffraction pattern formed by the scattered electrons show the surface structure. This is called reflection high energy electron diffraction (RHEED), a powerful technique to study the surface structures, especially in thin film deposition [37, 38, 36]. With ultrashort time resolution, a whole additional dimension is added for several reasons. First, surface structural changes or restructuring can be probed directly in real time. Second, there is a separation in time scales for motion in the surface layer and perpendicular to it, and initial nonequilibrium (not that of the diffusive regime) structures can be isolated [24]. Third, when the surface is used as a template, substrate-enhanced interferences can be exploited for mapping structural dynamics.

The Ewald sphere construction in RHEED geometry is shown in figure 3.2. The direction of the incident electron beam is defined with respect to a specific crystal orientation (zone axis), where  $\phi$  is the angle between the projection of the electron beam on the sample surface and the zone axis. For a monolayer of atoms in two-dimension, the reciprocal space exhibits “rods” separated by the inverse lattice distances ( $a$  and  $b$  in figure 3.2). The rods represent the constructive coherent interferences of waves. However, as this monolayer turns into a crystal slab, the rods become modulated, caused by the interlayer spacing ( $c$  in figure 3.2). For electrons, Ewalds sphere is large and the diffraction pattern, depending on the incidence angle  $\theta_i$ , exhibits both the streaks at low scattering angles and Bragg spots at higher angles in Laue zones.

The diffraction intensity can be simulated by using equation (3.5) or (3.6), in which the summations are over the penetrated regions (a few atomic layers) [38, 36]. In practice, a much simplified kinematic scheme of the electron diffraction is often used for crystal surfaces [39], as illustrated in the inset of figure 3.2. The momentum transfer  $\vec{s} \equiv \vec{k} - \vec{k}_0$  in reciprocal space satisfies the Laue condition  $\vec{s} = h\vec{a}^* + k\vec{b}^* + l\vec{c}^*$ , where integers  $h$ ,  $k$  and  $l$  are the Miller indices, and  $\vec{a}^*$ ,  $\vec{b}^*$  and  $\vec{c}^*$  are reciprocal lattice constants. The value of  $s = |\vec{s}|$  is given by  $s = 2k \sin(\theta_i)$ , and  $\tan(2\theta_i) = R/L$ , where  $R$  is the distance between the diffraction spot and the main beam position on

the screen and  $L$  is the distance between the sample and the screen, i.e., the camera length. When the diffracted angle  $\theta_i$  is very small, which is the case in RHEED,  $\sin(\theta_i) \approx \theta_i$  and  $\tan(2\theta_i) \approx 2\theta_i$ , and the momentum transfer is simply

$$s = k \cdot R/L \quad . \quad (3.8)$$

In RHEED geometry, transmission diffraction through three-dimensional islands or sharp edges is possible [37]. The transmission diffraction patterns are from the bulk reciprocal lattice, have different arrangements of diffracted beams and different behavior as a function of incidence angle comparing to the reflection diffraction. It was observed in our experiments of Langmuir-Blodgett films, as shown in chapter 5.

As a result of the strong interaction between a crystal and high energy electrons, multiple scattering of electrons can not be neglected for the quantitative analysis of the diffraction intensities. The dynamical theory, based on a Bloch-wave solution of the Schrödinger equation for one electron and a crystal potential, has to be utilized, with absorption effects taken into account as the imaginary part of the crystal potential [3, 33, 34, 36].

## 3.2 Pump-probe experiment

UEC is a pump-probe experiment, as illustrated in figure 3.3. We use a femtosecond laser as pump pulse to initiate the dynamics and to define the zero point in time. The ultrafast electron pulse is used as the probe pulse, which comes in at delay time  $\Delta t$ . Because the interaction of the electrons and sample atoms is very short even on the ultrafast time scale, the diffraction pattern generated by the electron pulse is from the sample atoms at time  $\Delta t$  and represents the dynamical structure at that time. By varying the delay time  $\Delta t$  between the laser pump pulse and the electron probe pulse, a series of the diffraction patterns are recorded. And the analysis of the diffraction patterns map out the structural dynamics as it happens.

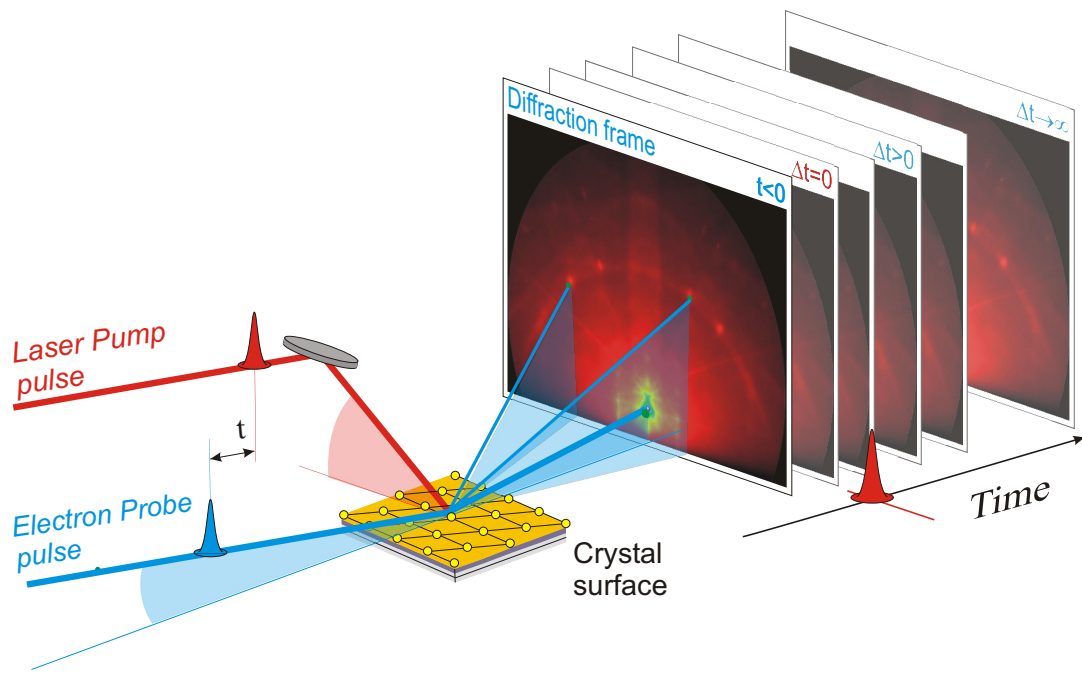


Figure 3.3: Schematic view of the experiment, showing the laser pump and the electron probe pulses, together with typical diffraction frames [25].

### 3.2.1 Characterization of the electron pulses

The number of electrons in each pulse is linear to the total intensity ( $I_{et}$ ) of the electron pulse recorded on the CCD camera,  $N = I_{et}/I_{es}$ , where  $I_{es}$  is the intensity produced by a single electron. The intensity  $I_{es}$  is a function of the voltage of the image intensifier and is measured as follows. After attenuate the laser (266nm) on photocathode to very low fluence, only a few electrons are generated per pulse and most of them arrive at well separated region on the CCD camera. The intensity of a single electron,  $I_{es}$ , is then measured on the screen and statistically satisfies Poisson distribution.

The spatial profile of the electron pulse is measured on the CCD. The electron beam profile on the CCD is Gaussian, and the general diameter (width in one dimension) of the electron beam in UEC experiments is about 500  $\mu\text{m}$  on the CCD.

The temporal width of the electron pulses is characterized in the streaking experiments. Just like in a streak camera, the temporal profile of the electron pulses is transformed into a spatial profile on the CCD, by deflection under a time-varying electrical field, as shown in the inset of figure 3.4. The resulting image forms a “streak” of electron pulses, from which the temporal width is inferred.

In our setup, the time-varying field is provided in the deflection plates (see figure 2.5) through the RC circuit shown in figure 3.4. To get the streaking speed on the order of 1 kV/ns, the resistor  $R$  is chosen to be 2 M $\Omega$ , and the capacitor  $C \simeq 0.01 \mu\text{F}$ . The photo-conductive switch is homemade by GaAs semiconductor wafer. When the 800nm laser pulse illuminate the wafer (see the optics layout in figure 2.9), the large electric field breaks the semiconductor and it becomes conducting.

The result of the streaking experiment for our electron gun is shown in figure 3.5. The linear relationship between the electron pulse length and the electron density (see figure 3.5(B)) shows that our electron pulse length is mainly restricted by the space charge effect. This curve only depends on the electron gun configuration, and the fitting line is characteristic of the electron gun. To determine the electron pulse length  $\tau$  of each experiment, the electron numbers are counted for single pulses. The

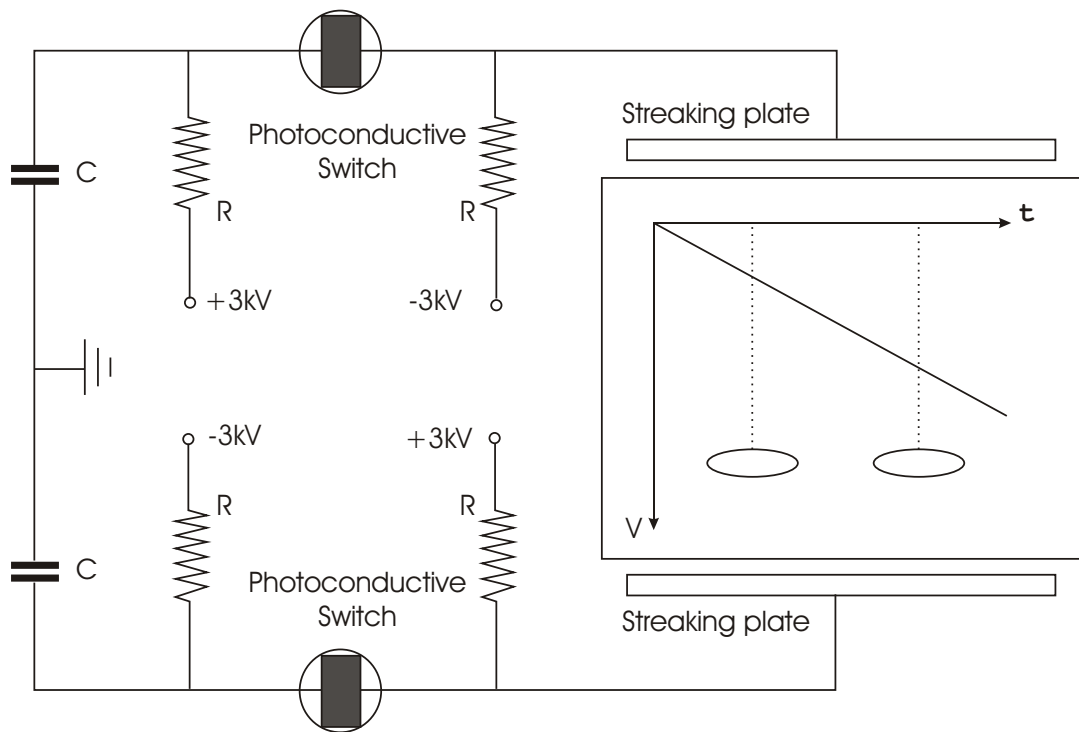


Figure 3.4: The electric diagram for the streaking experiment, the inset inside the streaking plates showing schematic view of streaking.

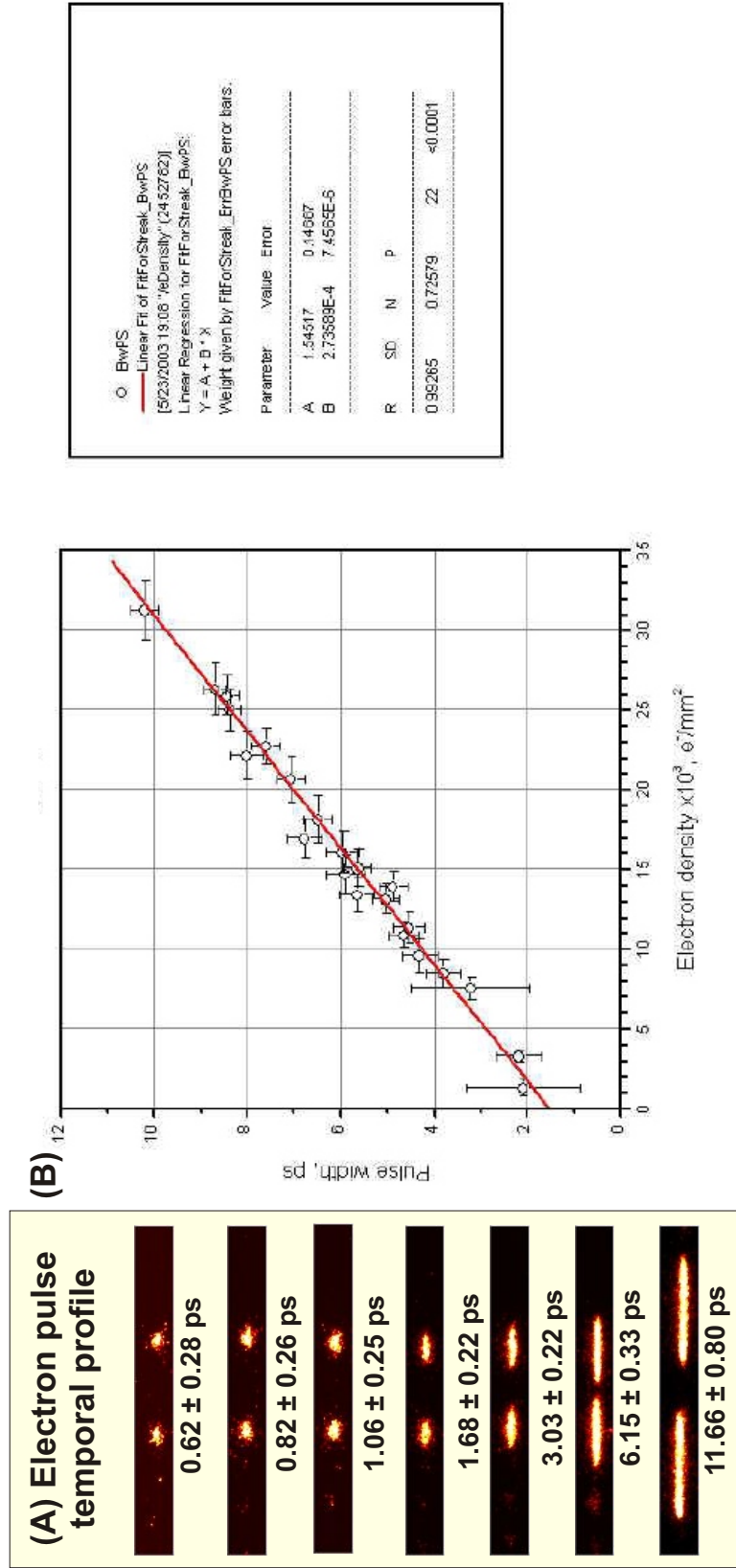


Figure 3.5: Result of the streaking experiment: (A) the streaked electron pulses are displayed for different pulse length [24]; (B) the electron pulse length as a function of the electron density.

electron density per pulse is derived from the electron numbers and the averaged electron spatial area on the CCD.  $\tau$  is determined by interpolation on the line given by the streaking experiment. On the other hand, in order to get different electron pulse length, the power of the 266nm laser for the electron gun is varied to obtain corresponding electron numbers.

### 3.2.2 Alignment of the laser and electron beams

Because the electron beam is invisible on the sample, a stainless steel needle and two diode lasers (from Lasermate Group) are used to help to spatially overlap the ultrafast laser beam and the electrons on the sample, as shown in figure 3.6(A). The stainless steel needle is inside the chamber and at the side of the sample holder (see figure 2.4). The needle tip defines a point in space where the two diode lasers shooting from two different directions, the ultrafast laser beam and the electrons are brought on respectively.

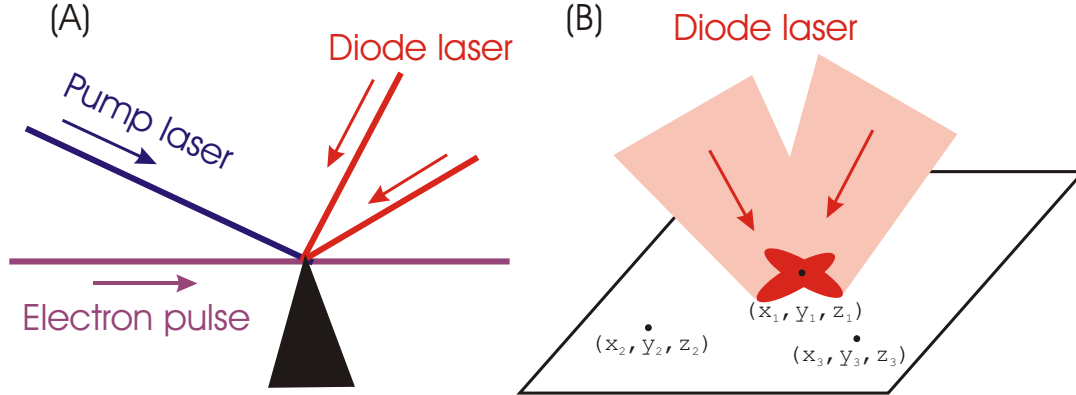


Figure 3.6: Schematic diagram of the alignment: (A) the overlap of the electron beam, the fs laser beam and two diode laser beams on the tip of the needle; (B) three-point alignment of the two diode laser to determine the sample surface plane.

After all four beams overlap on the needle tip, the sample is moved in position. The diode laser beams shoot on the sample and leave two prints (figure 3.6(B)), which are monitored through a viewport by a color CCD camera (JAI high resolution CCD camera with 75 mm focusing lens from Edmund Optics, Inc., Barrington, NJ) outside

the chamber. The sample has five degrees of freedom. They are three in translation,  $x$ ,  $y$  and  $z$ ; out of plane rotation  $\theta$  and in plane rotation  $\phi$ . With fixed  $\theta$  angle, the sample surface is a fixed plane in space. At the fixed position  $x$  and  $z$ , varying  $y$  can bring the two diode laser beams to overlap on the sample. This position on the sample surface is the same position where the needle tip was, and where the electron beam and the excitation fs laser beam overlap in space. This position is now defined by the coordinate  $(x_1, y_1, z_1)$ . Move the sample to another position with different  $x$  and  $z$ , and by changing  $y$  again bring the two diode laser beams overlap on the sample surface. This determines the second point  $(x_2, y_2, z_2)$ . Following the same procedure, a third point can also be determined at  $(x_3, y_3, z_3)$ . These three points thus define the sample surface plane at angle  $\theta$ .

Using the same method, a plane at a different  $\theta$  angle can also be found. The crossing line of these two planes is the axis around which  $\theta$  is rotated. Thus we find the relationship between the goniometer motion system and the overlap of the electron beam and the excitation fs laser beam in space. At any point on the sample surface when the sample is at any given  $\theta$ , we can calculate the coordinate which is required for the  $x$ ,  $y$ ,  $z$  motion to bring it to the overlap with the electron beam and the laser beam. We call this the three-point alignment.

In practice, we do the alignment at three different angles to check the relative accuracy of the determination. When doing experiments, after finding dynamics, we can move  $y$  a little bit to optimize for the overlap by optimizing the change of diffraction patterns.

### 3.2.3 Measuring the laser fluence on the sample

In order to determine the excitation laser fluence at the sample position, the laser power and the area of the laser illumination on the sample are measured individually.

Without the sample, the excitation laser power is measured right before entering the vacuum chamber ( $I_{total}$ ) and right after shooting out from the other side ( $I_{out}$ ) to determine the absorption  $I_a$  of the vacuum chamber windows  $I_a = (I_{total} - I_{out})/2$ . With the sample, the laser power  $I_{total}$  and  $I_{out}$  (after reflection) are measured again.

And the excitation laser power absorbed by the sample surface is given by  $I = I_{total} - I_{out} - I_a$ .

To measure the area of the laser illumination on the plane of the sample surface, the needle used for alignment is utilized. As shown in figure 3.7, assuming a round beam cross section with the radius  $r$  being the full width at half maximum (FWHM) of the Gaussian profile, the laser footprint on the  $xz$  plane (sample surface) is an ellipse with area

$$A = (\pi r^2) / \sin \theta \quad ,$$

where  $\theta$  is the angle between the laser beam and the  $xz$  plane. The needle is in the  $xy$  plane as shown in figure 2.4. By moving the needle in  $x$  direction, with enough height in  $y$  direction, the laser beam is blocked by the needle, starting from position  $x_1$  and ending at  $x_2$ . It is calculated that the relationship between the measured length  $l_x = x_2 - x_1$  and  $r$  is

$$2r = l_x \sin \Phi \quad , \quad (3.9)$$

where  $\Phi$  is the azimuthal angle in the  $xz$  plane (see figure 3.7). The calculation is not straightforward although the result is simple. The needle measures the projection of the laser on the  $xy$  plane, which is an ellipse with angles  $\theta'$  and  $\Phi'$  where  $\sin \theta' = \cos \theta \sin \Phi$  and  $\sin \theta = \cos \theta' \sin \Phi'$ . The equation of the ellipse in the  $xy$  plane is  $(x \cos \Phi' + y \sin \Phi')^2 \sin^2 \theta' + (y \cos \Phi' - x \sin \Phi')^2 = r^2$ . And the point of  $x_1$  and  $x_2$  satisfy the equation  $(x \cos \Phi' + y \sin \Phi') \sin^2 \theta' \sin \Phi' + (y \cos \Phi' - x \sin \Phi') \cos \Phi' = 0$ . The result (3.9) is obtained by solving the above equations.

### 3.2.4 Determining time resolution and time zero

The time resolution of UEC is determined by the laser pulse duration, electron pulse duration and the geometrical effect. Because of the group velocity dispersion, after traveling through the beam path (figure 2.9), the 120 fs laser ( $\lambda = 800$  nm) pulse broaden to approximately 200–300 fs. Since the electron pulse is generated by the fs laser pulse, its pulse length is equal to or larger than the fs laser pulse length. But our electron pulse length is limited by the space charge effect, as shown by our streaking

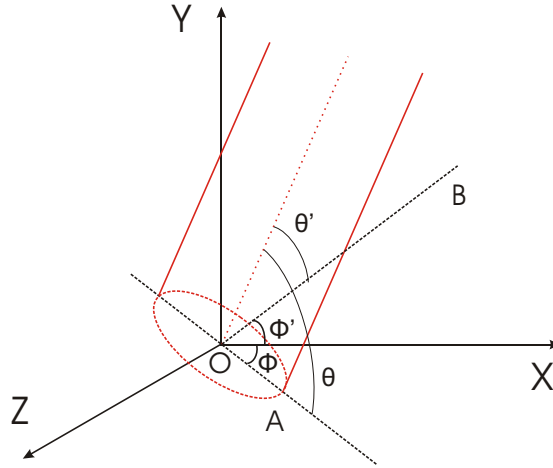


Figure 3.7: Schematic diagram of the measurement of excitation laser beam spatial profile.

experiment (see 3.2.1). In typical UEC experiments, electron pulses of 4–5 ps are used with  $\sim 3000$  electrons per pulse. So the electron pulse width and the geometrical effect are determining factors.

In the case of transmission, the sample is very thin ( $\sim 100$  nm). The time it takes for the electrons to travel through the sample is 1 fs for the  $1/3$  speed of light, which is the speed for our 30 keV electrons. So the time resolution is determined by the electron pulse duration. In this case, because of the high density of the atoms, fewer electrons can be used to get relatively good diffraction patterns. That brings shorter pulses and so better time resolution.

In the case of reflection, however, the geometrical effect is more important. The beam profile at the sample is about  $250 \mu\text{m}$ . At the incidence angle of  $1^\circ$ , the electron beam on the sample is 14 mm long. The laser beam profile on the sample, i.e., the excited area, is about 1 mm, which yields a group velocity dispersion (GVD) of 10 ps. To increase the time resolution, one way is to reduce the GVD by reducing the spatial extent of the sample by masking techniques [25]. With convolution and the strong level of signal from crystal surfaces, we readily obtained a 1-2 ps response. Another

way is to match the group velocity of the excitation laser pulse with the GVD of the electron pulse [32].

The time zero is determined *in situ*. However, it obscures any delay that may exist between the fs laser excitation and the start of the structural changes, as for example observed in InSb [40, 41]. Another method to determine time zero is to use the plasma lensing effect from the stainless steel needle [42, 43, 32]. It is shown that after the fs laser shoot on the needle, there is a charging effect which shifts the electron beam. It can determine the time zero to within 1 ps, but needs a lot of laser power and can destroy the needle tip.

### 3.3 Analysis of the diffraction patterns

The diffraction pattern recorded on the CCD represents an almost planar section in the reciprocal space. The corresponding reciprocal space distance to the distance on the screen is given by equation (3.8). The camera distance  $L$ , is the distance between the footprint of the incidence electron beam on the sample and the phosphor screen. It is determined *in situ*, by the crystal substrate diffraction patterns at varied incidence angles, with known lattice constants for the substrate (in our cases silicon). The direct beam position, i.e., the incidence beam on screen corresponding to  $s = 0$  (origin) in reciprocal space, is also determined *in situ* from the substrate diffraction patterns.

Depending on the sample surface crystallinity, the diffraction patterns are very different. The single-crystal or textured surface give diffraction spots or lines, whereas the polycrystal or amorphous surface give Debye-Scherrer diffraction rings. The analysis is different in the two cases.

When the sample surface is single-crystal or textured, the diffraction patterns contain diffraction spots or lines. The positions of the spots are determined by the crystal structure and the sizes (or the widths) show the states of defects in the crystal. The structural dynamics can be revealed by following the change in the positions and the sizes of the spots. To determine the position and the width accurately, especially

in the case when the change is very small, the spot or the line is fitted by a Voigt peak function in the direction of interest. Voigt function is the convolution of a Lorentz function and a Gaussian function. It is the best fit of our diffraction peak in general, though with different coefficient, sometimes the peak is more Lorentzian or Gaussian. The full width at half maximum (FWHM) of a Voigt function is given approximately as

$$(2\omega)^2 \simeq \frac{(2\omega_G)^2}{\ln 2} + (2\omega_L)^2 \quad ,$$

where  $2\omega$ ,  $2\omega_G$  and  $2\omega_L$  are the FWHM of the Voigt function, the Gaussian and the Lorentz function [44, 45].

When the sample surface is polycrystal or amorphous, the diffraction patterns contain diffused diffraction rings (half ring or curves on the ring above the shadow edge) with the same center, which is the direct beam position. Similar to the analysis of gas-phase material, the intensity is averaged on the curve (angularly) to get the diffraction intensity as a function of reciprocal space distance  $I(s)$ .

The intensity of the diffraction spots or rings are usually the first sign of structural change. In thermal equilibrium states, the intensity change with temperature is explained by Debye-Waller effect [34]. In reciprocal space, the effect of thermal vibration on the average potential can be described by

$$F_s = \sum_j f_j^{(e)} T_j \exp(i\vec{s} \cdot \vec{r}_j) \quad .$$

The temperature factor  $T_j$  is given by  $T_j = \exp(-\frac{1}{2} \langle (\vec{s} \cdot \vec{u}_j)^2 \rangle)$ , where  $\vec{u}_j$  denotes the instantaneous displacement of the  $j$ -th atom from its equilibrium position, and  $\langle \dots \rangle$  is averaging over thermal equilibrium. For isotropic thermal vibrations,  $\langle (\vec{s} \cdot \vec{u}_j)^2 \rangle = \frac{1}{3} s^2 \langle \vec{u}_j^2 \rangle$  and

$$T_j = \exp[-B_j s^2 / (16\pi^2)] \quad ,$$

where  $B_j = \frac{8}{3} \pi^2 \langle \vec{u}_j^2 \rangle$  is the Debye-Waller factor and  $B$  of many materials have been determined by theories and experiments. For a lot of simple crystals,

$B(T) \simeq a_0 + a_1 T$ . The total integrated intensity of a diffraction spot then satisfy the relationship

$$\ln\left(\frac{I(T)}{I(T_0)}\right) = -2[B(T) - B(T_0)]s^2 \quad .$$

However, since UEC is used to study the structural dynamics, the diffraction patterns are of samples in highly nonequilibrium state. So it could be questionable using the Debye-Waller coefficients, which are determined in the static temperature dependence experiments, to relate the intensity change with the thermal temperature change. Nevertheless, the intensity change gave insights on the orderness of the crystal structure, especially when combined with the widths change of the diffraction spots or rings.

The change with time is fitted with multiple exponential functions [46]. While the state of different structures are straightforward, it is assumed that the change is homogeneous in the probing area. The assumption is valid in the case when the probing area is much smaller than the excited area. In principal, a better theoretical analysis would be simulations using molecular dynamics to determine the atomic structure, and fit the whole diffraction pattern intensity using dynamical theory.

## Chapter 4

# Studies of Single-Crystal Surfaces with Small Adsorbates \*

The UEC experiments for surface studies were first demonstrated on semiconductor surfaces, such as silicon and GaAs. They are ideal systems because the surfaces can be relatively easily prepared with different adsorbates, and their crystalline and physical properties are well studied. There have been a wide range of ultrafast optical experiments (for reviews, see reference [47, 48]), as well as recent ultrafast X-ray experiments revealing bulk lattice dynamics following fs laser excitation (see reference [5] for a review). It has been shown that the energy transfer to the lattice on the ps time scale by electron-phonon coupling, first to optical phonons then to acoustic phonons, and the stress created by impulsive excitation leads to lattice waves. However, the ultrafast X-ray experiments could not probe the surface owing to the large penetration depth into the crystal, typically up to several  $\mu\text{m}$ , which is also much larger than the nm scale penetration depth of the pump laser. On the other hand, optical techniques that probed the surface on the scale of a few nm and matched the exact pumped region, could not directly determine the structure with atomic-scale resolution, but gave valuable information on the response of the dielectric function and lattice disordering [49, 50, 48]. The large scattering cross section of electrons combined with ultrafast time resolution allows the bridging of this gap in addressing the dynamics of surface structures in real time, and provides new insight to the dynamics of the surface adsorbates.

---

\*This chapter is based on the work presented in references [24, 25].

## 4.1 Silicon(111) surface

Silicon crystal structure is the diamond tetrahedral type [51] and the (111) surface is the most densely packed crystal plane, as depicted in figure 4.1. The bare surface is not stable in air because of the dangling bond and is easily oxidized. The Si(111) surface can be hydrogen terminated by standard method, or be terminated by other atoms or molecules, such as the halogens or a methyl group [52]. In our experiments, Si(111):H surfaces were prepared from wafers, first by cleaning and oxidation with an RCA-1 solution, then by etching in a 40%  $\text{NH}_4\text{F}$  solution for 15 to 20 minutes. And the surface quality was independently checked by LEED and Auger Spectroscopy.

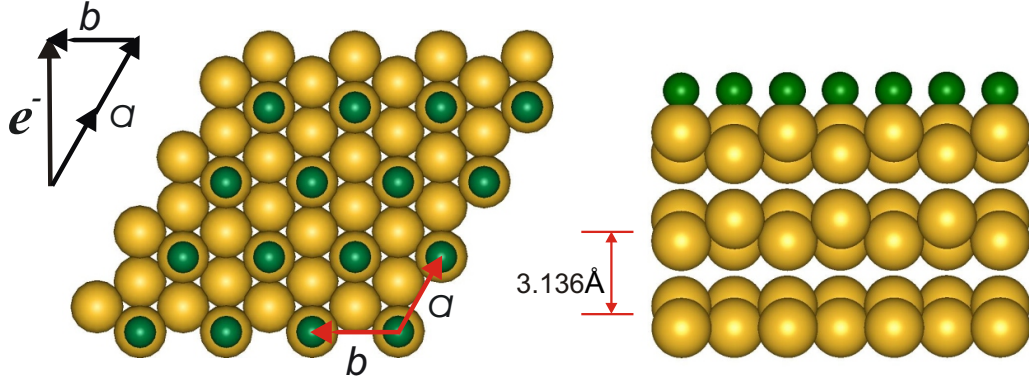


Figure 4.1: Structure of the Hydrogen-terminated Si(111) crystal, with the bilayer spacing of  $3.136 \text{ \AA}$  [24].

Figure 4.2 shows the static diffraction patterns of different Si(111) surfaces, obtained by using the ultrashort electron pulses, but without the initiating pumping laser pulse. And it is equivalent to the diffraction patterns obtained when the electron pulse arrive before the laser pulse, i.e.,  $t < 0$ . Figure 4.2 displays the very strong (0,0) streak, and other Bragg reflections in zero and first Laue zones, from a hydrogen terminated Si(111) surface. It demonstrates the high quality of the single-crystal surface, and the surface structure is determined to be  $(1 \times 1)$  Si(111). The rocking curves are obtained by varying the incidence angle  $\theta_i$ , as part of the rocking curve is shown in figure 4.3. From the Bragg angles the bilayer distance is determined.

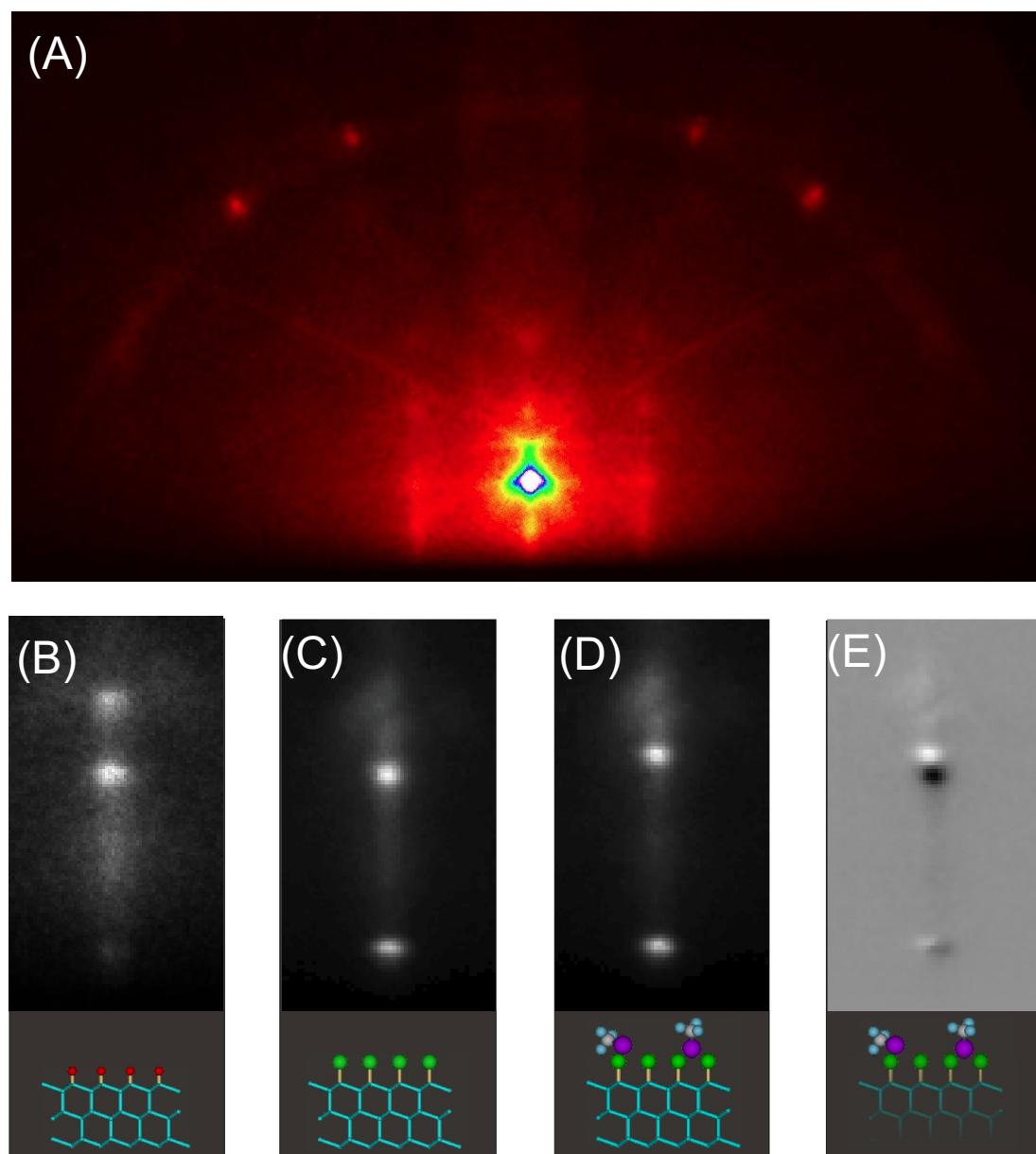


Figure 4.2: Diffraction patterns of Si(111) surfaces. (A) The pattern of hydrogen-terminated silicon in the in-phase condition. (B) A close-up of the (0,0) streak in the out-of-phase condition. Also shown are the changes in the streak region for chemisorbed chlorine (C) and physisorbed trifluoroiodomethane (D). The difference (D)-(C) enhances the diffraction change purely induced by coverage of trifluoroiodomethane (E) [24].

It is shown that in the out-of-phase condition, i.e.,  $\theta_i$  does not equal the Bragg angle, in the low angles ( $\theta_i < 2^\circ$ ) the intensity of the (0,0) streak is modulated to show two peaks. These two peaks are very sensitive to the surface condition, as shown in figure 4.2, and changes from hydrogen terminated to chlorine terminated, to a physisorbed trifluoroiodomethane structure, which was obtained by continuously dosing 99% pure gaseous trifluoroiodomethane at  $\sim 10^{-6}$  torr at the sample through the gas doser. As such, they are also very sensitive to the surface structural change in the ultrafast time scale. To calculate the diffraction intensity modulation requires the inclusion of multiple scattering in a dynamical theory. However, the kinematical modeling can reproduce the basic features of the (0,0) streak [24]. For hydrogen termination, it is calculated from the diffraction pattern that the silicon atoms of the top bilayer on the surface contract by 0.08 Å from that of the bulk, in agreement with *ab initio* theoretical analysis [53].

Figure 4.3 displays the time dependent rocking curves of the Bragg spot (-4,7), which is a side peak at the first Laue zone and the notation follows the chosen  $\vec{a}$  and  $\vec{b}$  in figure 4.1. As shown in figure 4.3(A), at higher  $\theta_i$ , the side spot's position changes as an effect of the incidence Bragg angle. Figure 4.3(B) shows that the shift and width of the Bragg peak behave differently but consistently, with the delay needed for the creation of the lattice phonons [48]. The width increases to its maximum value ( $\Delta\theta = 0.08^\circ$ ), but then decays with the time constant indicated (40 ps). The shift, however, has a finite rise comparable to the time it takes the broadening to lose almost 80% of its maximum value. Accordingly, the initial stress created in the substrate leads to an inhomogeneous compression and expansion which result in the known broadenings (by coherent phonons [54]) of the rocking curves. As the lattice reaches its maximum expansion, with the decay of inhomogeneity due to the loss of coherence of acoustic phonons, the shift reaches its maximum value; at longer times, both broadening and shift recover the values of the equilibrium structure. The maximum expansion, following the decay of acoustic phonons, is observed at  $\theta_i = 3.06^\circ$ , which corresponds to a 1.7% (0.04 Å) increase for the Si-Si distance at 2.35 Å. Even at the maximum shift, there is still an interplay between energy redistribution

and cooling. At the point of levelling off (figure 4.3(B)), the shift ( $0.015 \text{ \AA}$ ) defines a lattice temperature of  $\sim 1500 \text{ K}$ , just below melting ( $1687 \text{ K}$ ).

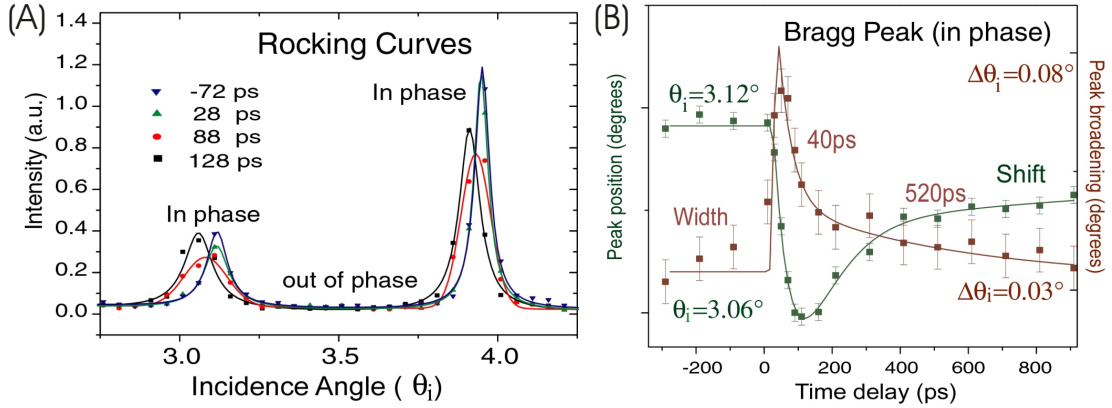


Figure 4.3: The temporal change of the Bragg spot (-4,7). (A) The temporal profile of the rocking curves for the (-4,7) Bragg spot. Note only four data points are shown to illustrate the dynamical changes. (B) The brown and green curves give the time-dependence of the angular width and position of the Bragg spot (-4,7) by following the rocking curves in panel (A) [24].

These studies were also extended to chemisorption (hydrogen and chlorine atoms) and physisorption (trifluoriodomethane molecules) on silicon surfaces in order to elucidate the effect of surface motion and the potential of the absorbed atoms or molecules. On going from hydrogen to chlorine, the amplitude of the atomic motion decrease to  $\sim 0.1 \text{ \AA}$ . The temporal response of the chlorine system is similar in trends to that of hydrogen but significantly slower to be 110 ps. Two processes might be in effect here; first the heavier mass of chlorine compared to hydrogen, and second the high electronegativity. Trapping of electrons, with the change in the available energy, modifies the potential and also requires additional nuclear motions of the adsorbates. The adsorption of molecular trifluoriodomethane shortens the decay, consistent with a reduced effective electronegativity due to the physisorption of the molecules.

The structural changes involved in phase transitions were studied, when the temperature of the lattice is high enough to cause large amplitude disorder. This critically depends on the density of the excited carries. Studies were performed at different excitation fluences (800nm and 266nm), and it was found that the maximum impulsive

surface motion of atoms emerges when the carrier density is about a factor 2–5 below  $10^{22} \text{ cm}^{-3}$ , the threshold for melting. At carrier densities of  $5 \times 10^{20} \text{ cm}^{-3}$  and below, the surface response is slower and the amplitude of structure change is linear with energy fluence. From bulk structural point of view, melting is defined by the Lindemann limit [55] which sets a 10% lattice change as the threshold for disorder. However, it is not clear that the limit is applicable to surface and mesoscopic melting [56]. In UEC experiments, irradiation of crystalline silicon with infrared pulses for a few hours, just below the damage threshold, results in amorphous silicon. The loss of the crystalline to the amorphous structure was evident in the disappearance of the intense Bragg spots and the appearance of smooth rings in our diffraction images (figure 4.4(A)).

Infrared fs pulse excitation of this amorphous structure gives new diffraction ring patterns, which we followed as a function of time. The instantaneous structural change is a phase transition to the liquid state. This is evident in the change of the radial distribution function, as we observe a depletion of the density of the second coordination shell at  $\sim 4.3 \text{ \AA}$ , while the density of the first coordination shell at  $2.35 \text{ \AA}$  remains the same. Unlike crystalline silicon, amorphous silicon is best described by a continuous random network model [57], in which atoms are topologically connected with fourfold coordination, but with the bond angles fluctuating substantially around  $109.5^\circ$ , the tetrahedron angle. And the first two coordination shells of the radial distribution function around  $2.4$  and  $4 \text{ \AA}$ , respectively [58]. In the liquid phase, the bond angle fluctuations are further enhanced, and the radial distribution function shows almost no second coordination shell [59].

The amorphous-to-liquid phase transition occurs in  $\sim 10$  ps and the amorphous structure is recovered on a much different time scale (figure 4.4(C)). However, the liquid phase persists for  $\sim 100$  ps, as evident from the plateau. The persistence of the liquid phase indicates that the surface layers probed by the electrons remain very hot, being unable to dissipate the thermal excess energy. We note that the time scale reported here for the phase transition is different from that of the crystalline-to-liquid silicon, measured by reflection methods [60] and that the restructuring occurs on a

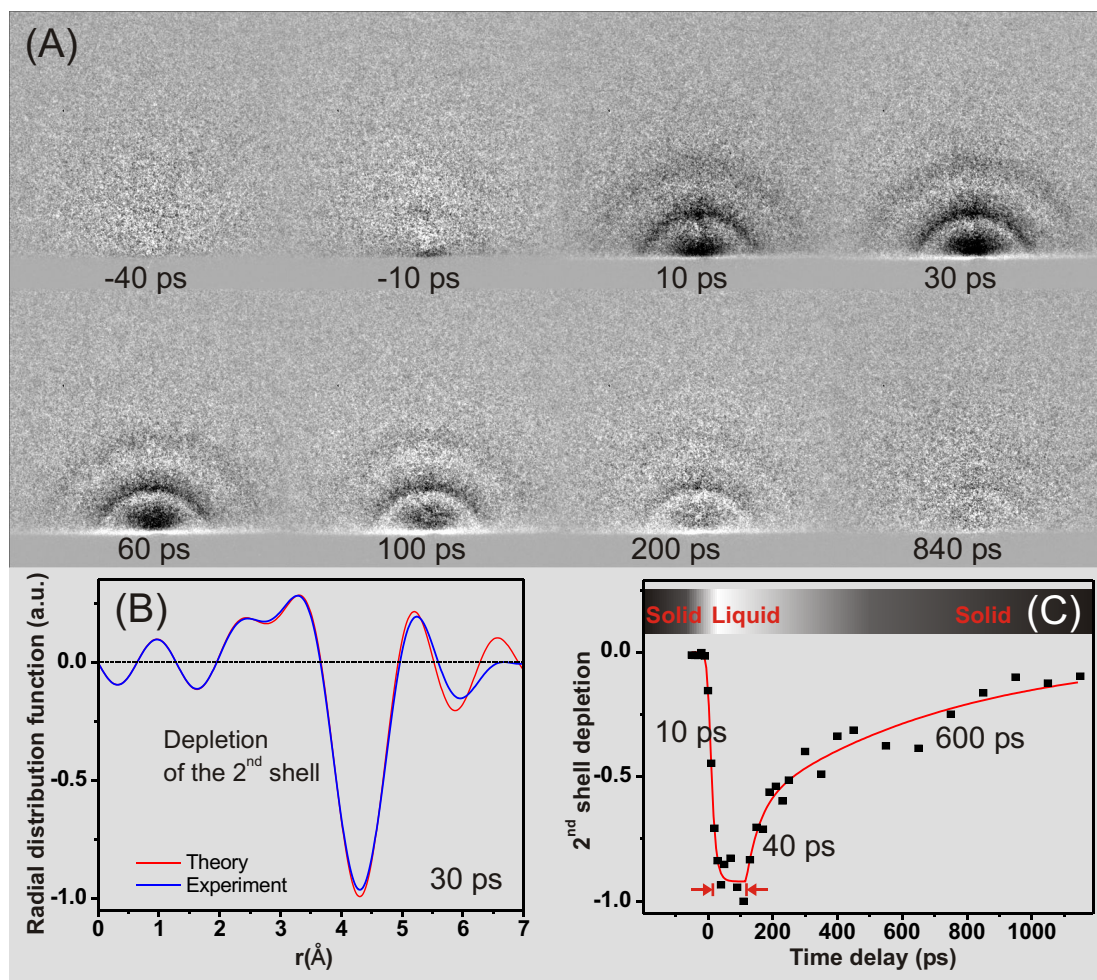


Figure 4.4: UEC of phase transition of the amorphous to liquid state. (A) Diffraction difference patterns at various time delays. From the patterns, we obtained a “molecular” scattering function and by Fourier transform the radial distribution function (shown in (B) for  $t = +30$  ps). (C) The time dependence of the depletion and recovery of the second shell shows the ultrafast melting, followed by a  $\sim 100$  ps plateau, and later by resolidification ( $\sim 40$  ps and  $\sim 600$  ps) [24].

time scale much shorter than typically reported for equilibration (ns or longer)[61]. Recent *ab initio* molecular dynamics simulations of silicon melting [62] have elucidated that ultrafast structural changes can lead to a new liquid structure characterized by a high coordination number and strong reduction of covalent bonding. This leads to significant changes in the shape of the pair correlation function  $g(r)$  around  $\sim 4$  Å. We have observed the time evolution of the peak at  $\sim 4.3$  Å toward shorter distances (the second shell is at 3.8 Å in the amorphous solid and 3.6 Å in the liquid [58, 59]).

## 4.2 GaAs(111) surface

The GaAs is of Zinc Blend structure. Unlike Silicon, it is a semiconductor with direct bandgap [63]. The GaAs(111) surface was prepared following the procedure of reference [64]. The semi-insulating GaAs(111) crystals were terminated by a monolayer of chlorine with a Cl atom atop each Ga atom, saturating the otherwise dangling bond of Ga (figure 4.5). The surface retained its integrity throughout the experiments, as evidenced by the unchanged quality of the diffraction patterns.

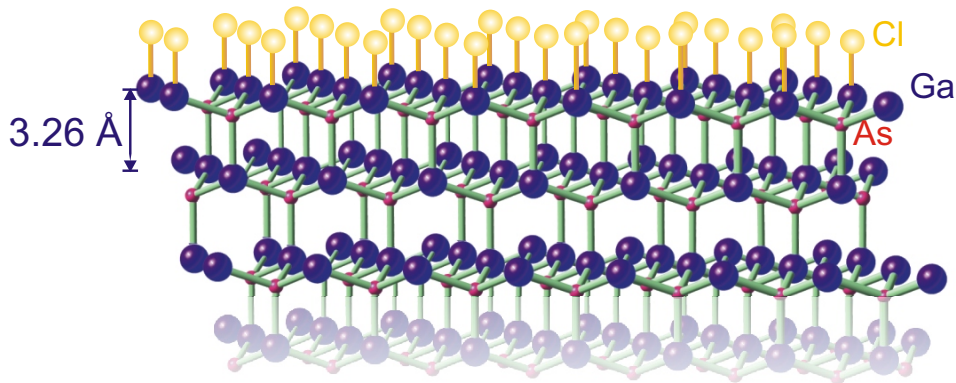


Figure 4.5: Structure of the chlorine-terminated GaAs(111) crystal, with the bilayer spacing of 3.26 Å [25].

The two-dimensional surface structure is shown in figure 4.6. Figure 4.6(A) displays the real space crystal lattice, with the atomic spacing of  $a = b = 4.00$  Å. The

samples were positioned to allow the electron beam to impinge at the chosen incidence angle ( $\theta_i < 5^\circ$ ), azimuthally along the  $\langle 11\bar{2} \rangle$  direction. Figure 4.6(B) displays the corresponding reciprocal lattice, with  $a^* = b^* = 0.289 \text{ \AA}^{-1}$ . The lattice basic vectors can also be chosen as  $\vec{X}$  and  $\vec{Y}$ , and the reciprocal vectors are  $\vec{X}^*$  and  $\vec{Y}^*$ , where  $\vec{X}^*$  is perpendicular to the electron incidence and  $\vec{X}^* = \sqrt{3}a^* = 0.499 \text{ \AA}^{-1}$ . The Ewald sphere of radius  $k = \lambda^{-1} = 14.33 \text{ \AA}^{-1}$  intersects with the reciprocal lattice as shown in figure 4.6(B). LZ0, LZ1 and LZ2 refer to the zero-order, first-order and second-order Laue zones.

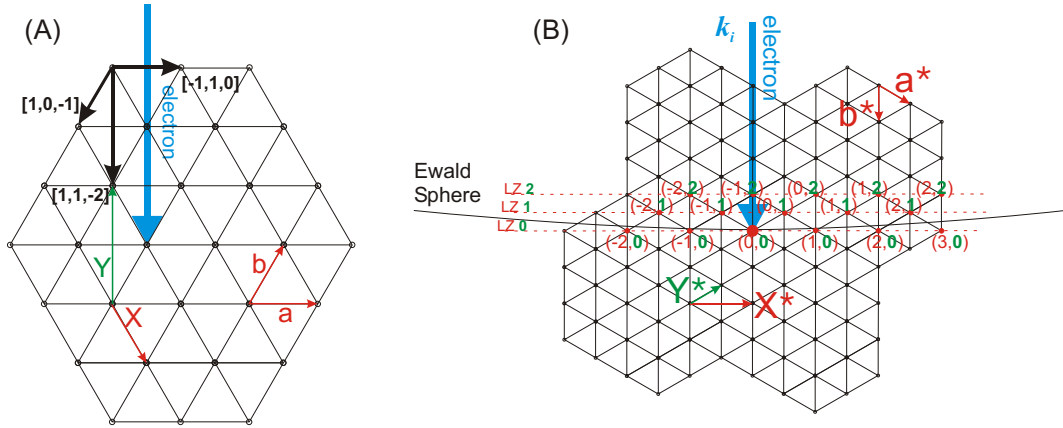


Figure 4.6: GaAs:Cl(111) surface lattice (A) in real space and (B) in reciprocal space.

Figure 4.7 presents a typical static diffraction image, which displays the very strong (0,0) and other Bragg reflections. Figure 4.7(A) shows a diffraction pattern, with such incidence angle as to reveal higher order diffraction peaks as well as diffraction streaks in the zero-order Laue zone. These and similar data allow for the precise determination of the camera distance from the scattering position ( $170 \pm 1 \text{ mm}$ ).

By gating the detection on the (0,0) Bragg spot and following the diffraction position as a function of the incidence angle, we also obtained the experimental rocking curve, which gives the GaAs lattice periodicity along the (111) direction ( $n = 1, 2, \dots$ ). This is shown in figure 4.7(B), where the incidence angle was varied over several degrees. The experimental periodicity in  $\theta_i$  of  $0.60^\circ \pm 0.02^\circ$  is in quantitative agreement with the expected value of  $0.61^\circ$  obtained for the lattice bilayer

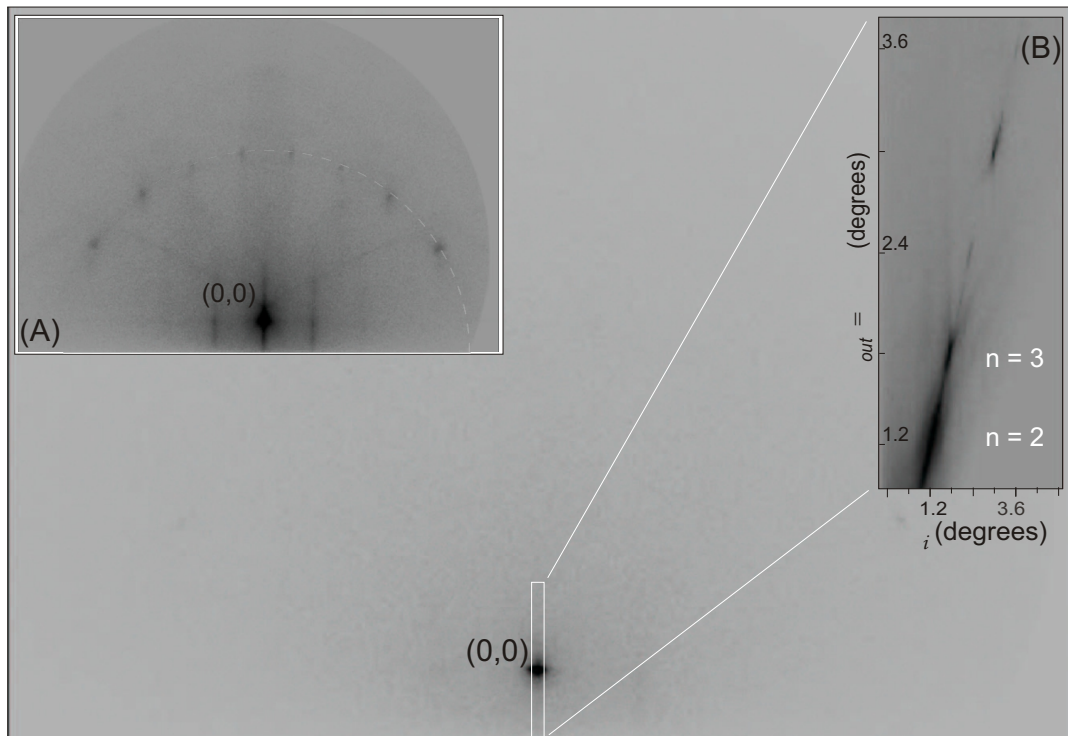


Figure 4.7: Static diffraction images of the GaAs:H(111) surface obtained by the ultrashort electron pulses. (A) Diffraction image showing the intense (0,0) in-phase reflection, together with the streaks and spots in the Laue zones. (B) Experimental rocking curve for the (0,0) reflection — (111) lattice planes. Note the image intensity is inverted [25].

spacing of 3.26 Å.

In the time-resolved experiment, the excitation laser of 266nm (400  $\mu$ J, <300 fs) is used. This UV pulse at  $t = 0$  defines the initial temperature and structural change. We follow the center position, intensity and the width of the  $n = 2$  (0,0) Bragg spot as a function of time.

The change of the peak center position maps out the change of lattice spacing in the (111) direction, as shown for two different laser excitation powers in figure 4.8. Results are shown for fluences of 9% and 45% of the experimentally determined 4.5 mJ/cm<sup>2</sup> damage threshold at 266nm. The angular deviation ( $\Delta\theta$ ) of the Bragg spot directly gives the change in lattice spacing ( $\Delta d_{111}$ ), from the relation  $\Delta d_{111} = -\frac{\Delta\theta \cdot d_{111}}{2\sin(\theta/2)}$  here  $\theta$  is the total scattering angle. A deviation to larger or smaller angles ( $\Delta\theta > 0$  or  $\Delta\theta < 0$ ) is therefore the signature of lattice contraction or expansion.

From the results shown in figure 4.8, it is evident that, following excitation at  $t = 0$ , the top surface layers of the crystal immediately contract. The amplitude of this initial contraction is given for two fluences, but the complete fluence dependence is presented in figure 4.9. After the initial contraction (-0.015 Å), the system expands to a maximum amplitude: +0.025 Å for fluence of 2 mJ/cm<sup>2</sup> and +0.005 Å for fluence of 0.4 mJ/cm<sup>2</sup>. As can be seen from figure 4.9, the maximum expansion amplitude strongly depends on the fluence: the larger the fluence the more ample the expansion. The data also show that both the onset time and the velocity of the expansion ( $\sim$ m/s) strongly depend on the fluence: expansion occurs earlier and faster at the higher fluences. After reaching its maximum expansion, the system contracts again toward the original lattice spacing on a much longer time scale, beyond 50 ps, but a finite smaller expansion persists for at least several ns. Observations were also made for 800nm fs excitation at various laser fluences and the behavior is similar, namely an initial contraction, followed by an expansion and the subsequent return toward the initial lattice spacing. This similarity in form indicates that the observed structural dynamics is not dominated by a charging of the surface by photoemission, since excitation at 800nm and/or at low fluences gives similar behaviors.

The transient temperature is evident in the change of the diffraction integrated

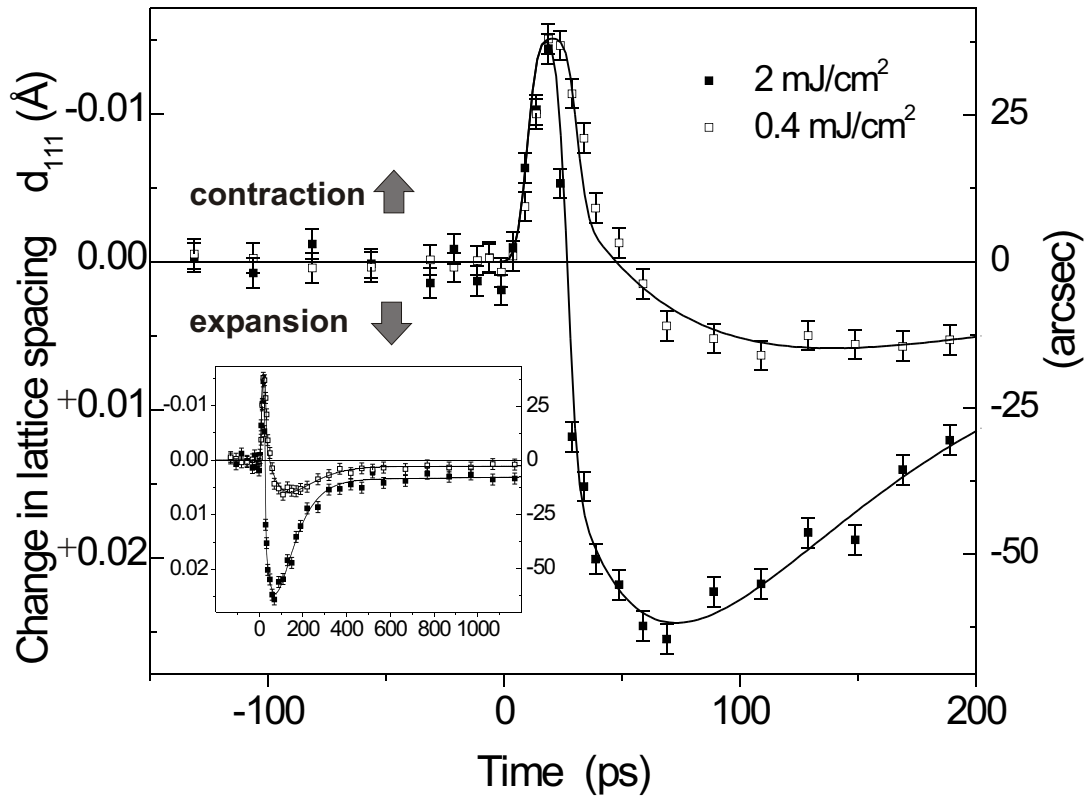


Figure 4.8: Center position of the Bragg spot as a function of time and fluence. The vertical axis on the right gives the angular deviation and the left axis shows the corresponding change in lattice spacing, perpendicular to the (111) surface plane. The inset shows the evolution at long time [25].

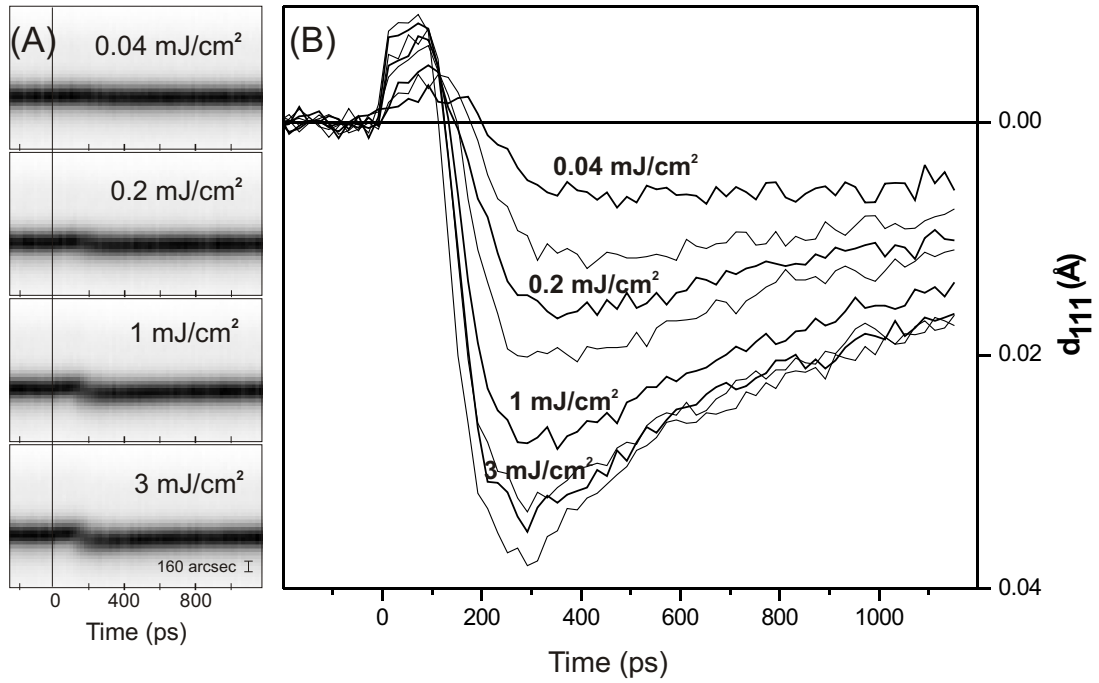


Figure 4.9: Fluence dependence of the Bragg reflection center position change. (A) Experimental traces for a set of data at the indicated fluences. (B) Time dependence of  $\Delta d_{111}$ , corresponding to the Bragg reflection center position change, at different excitation fluences [25].

intensity with time. This is presented in figure 4.10, for excitation at 45% of damage threshold ( $2 \text{ mJ/cm}^2$ ), by plotting the evolution of the integrated intensity of the Bragg spot as a function of time. Using the tabulated Debye-Waller factors for bulk GaAs [65], and taking into account the two-dimensionality of the surface [66], we obtained an initial temperature jump to  $1565 \pm 83 \text{ K}$ . The system cools down on the time scale of a few hundreds of ps to reach  $\sim 510 \text{ K}$  after 1 ns. The initial temperature jump has a rise time of 7 ps (10 ps before deconvolution). This was made possible by reducing the spatial extent of the sample to  $400 \mu\text{m}$  by masking (i.e., scratching the other surface area to remove the crystal surface), resulting in a transit time of 4 ps and temporal cross-correlation of 7 ps. This rise time is in perfect agreement with results from fs optical studies of the dielectric function [50, 48]. Moreover, the maximum temperature reported above is close to the value (range of 1300 to 1500 K) extrapolated from these optical studies at corresponding fluence. For the lower fluence regime ( $0.4 \text{ mJ/cm}^2$ ) presented in figure 4.8, we find a temperature jump to  $420 \pm 18 \text{ K}$ , with a decay leveling off at  $320 \pm 5 \text{ K}$  after 1 ns. In this case too, the rise time and the maximum temperature are consistent with the optical study.

The evolution of the lattice expansion and that of the temperature are compared juxtaposed in figure 4.10, together with the width for the data set obtained at  $2 \text{ mJ/cm}^2$ . Strikingly, the temperature evolution precedes the lattice expansion and we measured a delay of 13 ps between the rise of the temperature and that of structural expansion. This lag in structural expansion provides a direct evidence for the proposed delayed lattice changes following an impulsive initial temperature [50, 48]. We note that the temperature jump to  $1565 \pm 83 \text{ K}$  is similar to (or even exceeds) the 1513 K melting point [63], while the excitation fluence is only half of the damage threshold. However, as evident from figure 4.10, the peak temperature does not persist for a long time and the system does not lose its crystalline structure.

The lagged structural change reaches its maximum expansion of  $+0.025 \text{ \AA}$  at a temperature of  $\sim 1000 \text{ K}$  (figure 4.10). This lattice expansion in nm-scale structure may now be compared with the expansion in bulk GaAs. From the linear expansion coefficient of bulk crystal [63], a temperature of 1000 K would correspond to a linear

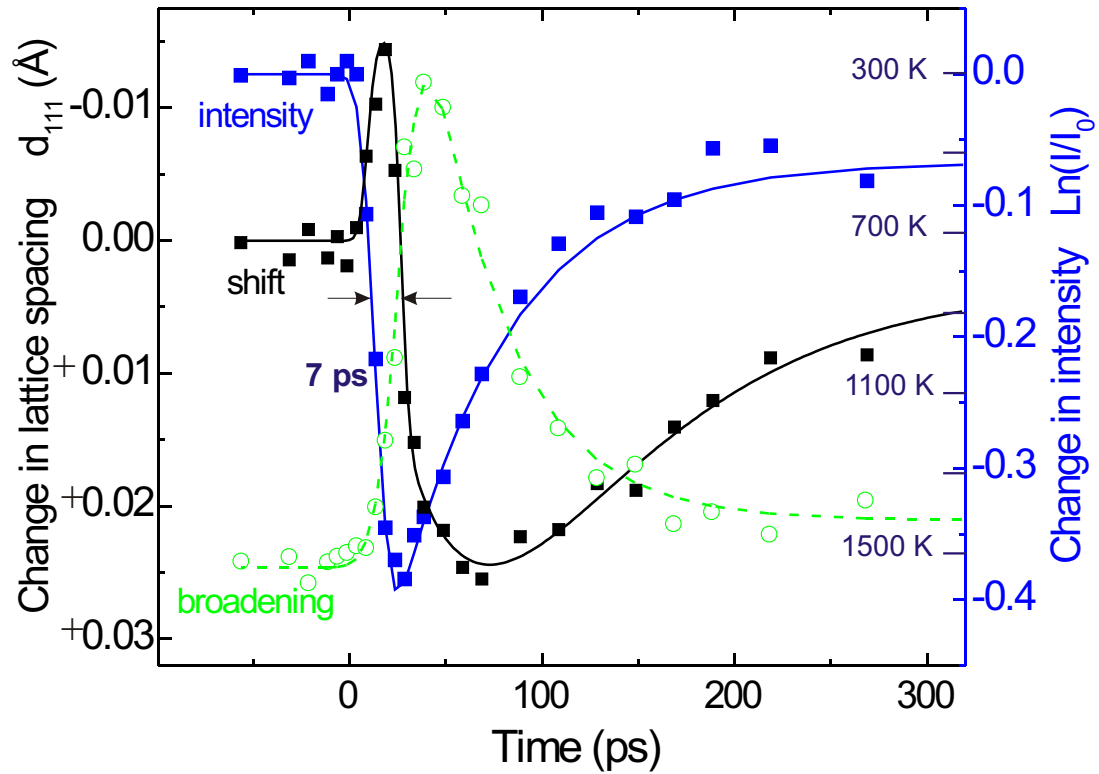


Figure 4.10: Comparison of the integrated intensity of the Bragg spot (temperature) with the change in lattice spacing for the data set obtained at  $2 \text{ mJ/cm}^2$ . The right axis gives the ratio of the time-dependent integrated intensity of the Bragg spot ( $I$ ) to its counterpart at negative delay ( $I_0$ ) on a logarithmic scale, from which the temperature scale is obtained. The lattice expansion is also shown with its scale on the left axis, together with the broadening of the Bragg spot, depicted by the dashed line. The apparent delay between the temperature rise and the lattice expansion is noted by the two arrows [25].

lattice expansion of  $0.013 \text{ \AA}$ , and this value differs by a factor of two from our experimental value of  $0.025 \pm 0.001 \text{ \AA}$ . At much longer times ( $\sim 1 \text{ ns}$ ), when the change in expansion levels off, the temperature of  $510 \text{ K}$  would correspond to a linear expansion of  $0.0038 \text{ \AA}$  and our experimental value is  $0.0032 \pm 0.0005 \text{ \AA}$ . This temporal decrease of the disparity in spacing is indicative of the change of surface to bulk-type behavior. From modeling of strain propagation in X-ray studies, a  $0.0082 \text{ \AA}$  surface strain amplitude was inferred for GaAs [67]. Our measurement indicate a deformation larger by a factor of three.

Because of their small incidence angle, the probing electrons have a very small penetration depth ( $\sim 7 \text{ \AA}$ , for  $30 \text{ keV}$  electrons at  $\theta_i \simeq 1^\circ$ ) and thus probe only the very top surface layers of the crystal; in the geometry of our experiment, the excitation pulse ( $30^\circ$  incidence angle) has a vertical penetration depth also of nm scale ( $3.5 \text{ nm}$  at  $266 \text{ nm}$ ). These small and comparable penetration depths for the photons and for the electrons provide a unique condition for monitoring local structural dynamics of these surface layers. In X-ray experiments, a heating pulse typically has an absorption length of  $0.3 \text{ }\mu\text{m}$ , and the probing X-ray pulse has a  $\mu\text{m}$ -scale penetration depth. Such scales require consideration of strain propagation in the bulk [67]. Clearly, direct probing of the surface motions of atoms is critical to the understanding of the surface initial dynamics and to the connection to bulk propagation at different temperatures (fluences).

Additional experiments were carried out on silicon to both isolate the effect of chlorination, and also to test the generality of the approach and the scope of application. Both chlorinated and nonchlorinated silicon (111) surfaces were subjected to the same experimental conditions (excitation wavelength and fluence). Similar behavior to that of GaAs was found — while hydrogen-terminated silicon did not present noticeable surface contraction preceding the expansion ( $+0.06 \text{ \AA}$ ), the chlorinated surface showed a prompt contraction ( $-0.03 \text{ \AA}$ ), which precedes the expansion ( $+0.07 \text{ \AA}$ ).

A general structural dynamics picture now emerges from the observations of the structure changes and the time scales of the motion, and from the observations on

silicon surfaces. In the nonthermal regime, the initial fs transient excitation, which creates the electron-hole pairs, distorts the potential, and on the ultrashort time scale, structural changes occur by this deformation prior to significant motion in the lattice (phonons), as experimentally verified above. This highly nonequilibrium state of the solid is followed by energy dissipation and redistribution, which ultimately lead to expansion of the lattice and restructuring at longer times. With this in mind, only an expansion of the surface atoms would be expected, contrary to the observation made here of contraction and expansion. However, for the chlorine-terminated surface, the large electronegativity shifts the electronic charge distribution towards the chlorine (ionic potential). The ensuing Coulomb interaction with the underlying layers contracts the interatomic layers, as observed in the early-time ultrafast rise of the contraction, and on this time scale, the dynamics is driven by the potential change. Along with the observations made in the case of silicon and supporting this proposed mechanism for contraction, we note that atomic chlorine chemisorbed on GaAs was found to be an electron acceptor [68].

Following the contraction, expansion proceeds and on a similar time scale. Through Auger processes (at density of  $\sim 10^{21} \text{ cm}^{-3}$ ), which take place in a few ps, the carrier density decreases, but the total electronic energy remains unchanged [69, 70]. The drop in the Coulombic potential along with electron-phonon coupling now drives the system in a reversed motion towards expansion. The expansion of the lattice requires 7 ps to define surface layers temperature and this is evident in the rise of the intensity profile (figure 4.10); only after this rise can we define the temperature acquired through electron-phonon coupling. The structural change (expansion) follows the temperature rise, but after an apparent delay of  $\sim 15$  ps, reaching its maximum of  $+0.025 \text{ \AA}$  expansion at yet longer time. This thermal expansion in the (111) direction must be due to anharmonicity of lattice vibrations. Remarkably, the width of the Bragg spot reaches its maximum before the peak of structural lattice expansion. Lattice dynamics is first driven by coherent collective phonons followed by the isotropic expansion that ensues when anharmonicity becomes effective. This nascent lattice expansion must first overcome the persisting contraction. From our data, we

obtained an onset for the expansion of  $\sim 5$  ps after the temperature has risen to half of its maximum and an additional delay of  $\sim 10$  ps to overcome the initial contraction. It should be noted that this picture of structural dynamics is robust at lower fluences (figure 4.9). However, in the lower fluence regime, the initial temperature is decreased, electron-phonon coupling dominates, and at longer times diffusive processes become pronounced.

The return to the original structure is observed in the decrease of  $\Delta d_{111}$ , from  $+0.025$  Å to  $+0.003$  Å, but this restructuring takes place on a much longer time scale. We note that diffusive processes must begin beyond 50 ps, as up to this time  $\Delta d_{111}$  continues to increase — cooling down the surface by diffusion leads to decrease in  $\Delta d_{111}$ . Thus, the structure at the expanded value of  $\Delta d_{111} = 0.025$  Å is vibrationally in a nonequilibrium state of collective modes, which cools down by energy redistribution and diffusion at longer times. Theoretical calculations of the heat diffusion using the known thermal properties of GaAs (heat capacity and thermal conductivity [63]) gave a good match to the temperature behavior from the point of leveling off shown in figure 4.10.

### 4.3 Surfaces with adsorbates

The single-crystal surfaces provide a template for UEC experiments to study the ultrafast dynamics of molecular adsorbates, following the ultrafast infrared (IR) laser induced temperature jump in the substrate. We studied physisorbed trifluoroiodomethane on Si(111):H surfaces, water/ice on hydrophilic surfaces (chlorine terminated Si(111)) [24], and self assembled monolayer of 2-mercaptoacetic acid and iron hemes on Au(111) surfaces [27].

In the water experiment [24], we observed the coexistence of ordered surface water and crystallite-like ice structures on the nm scale, evident in the superposition of Bragg spots and Debye-Scherrer rings. The structures were determined to be dominantly cubic, but each undergoes different dynamics after the ultrafast substrate temperature jump. From changes in local bond distances with time, we elucidated

the structural changes in the far-from-equilibrium regime at short times and near-equilibration at long times. However, for trifluoriodomethane on Si(111):H surfaces or self assembled monolayer on Au(111) surfaces [27], only the modulations on the substrate surface diffraction pattern were observed. Although the diffraction difference images show some structural features, it is hard to relate it to structural changes.

The challenge with these experiments is that the low density and disordering of the adsorbates, comparing to the single-crystal substrates, prevent the formation of a diffraction pattern clearly showing the structure of the molecules. While qualitatively, the diffraction patterns were shown to differ from the substrate surfaces, it is very difficult to extract quantitative structural information from the diffraction patterns. Because of the small differences, dynamical scattering theory has to be taken into account in order to analyze the diffraction patterns or to do theoretical modeling.

## Chapter 5

# Fatty Acid and Phospholipid Crystalline Adsorbates: Steady State Studies \*

To study the structural dynamics of molecular adsorbates on the surfaces, we used the Langmuir-Blodgett (LB) films. The LB technique was first introduced by Irving Langmuir and Katharine B. Blodgett in the 1930s [72, 73, 74]. Since then, it has proven powerful in the preparation of two-dimensional crystalline films [75, 76]. It allows for a controlled layer-by-layer deposition of ordered molecular films, and many different kinds of molecules have been successfully made into LB films. Because of the resemblance to naturally occurring biological membranes, lipid Langmuir films at water surfaces and Langmuir-Blodgett (LB) films often serve as a model system for studying membrane structures and properties under controlled conditions, such as head group organization and hydration [77], phase transitions [78], interactions with membrane proteins [79, 80], and proton diffusion [81]. And they are important in many other applications of technology developments, such as molecular electronics [82], biological sensors [83] and nonlinear optics [84]. The higher order and definite crystalline structure of LB films, compared with self-assembly, make them ideal for UEC studies.

However, the selective preparation of adsorbates with well-defined structures by means of the LB technique is not a trivial task [85, 86]. There was and still is

---

\*This chapter is based on the work presented in references [28, 29, 71].

considerable effort in understanding the structure of even the “simplest” of all LB films, fatty acids and fatty acid salts (see reference [87, 88] for reviews). A plethora of powerful techniques (e.g., electron diffraction, neutron scattering, X-ray techniques, atomic force microscopy, FTIR, Raman spectroscopy, NMR) have been utilized to study the effect of the substrate [89, 90, 91], dipping conditions (for example, pH-value [86, 92, 93], pressure [94, 95, 96, 92, 97, 98], counterion [89, 90]) and the effect of the surfactant itself on the resulting film structure. Of particular interest are the tilting of fatty acids [94, 95, 97], structural differences in mono- and multilayers [99, 100, 101], epitaxial growth of fatty acids [102, 103, 104], and thermal annealing effects [103, 104, 105].

Phospholipids are the main building blocks of biomembranes and their molecular structures are similar to those of fatty acids. Although more complex and less studied, the structure of phospholipids LB films have been probed by a variety of techniques, including electron diffraction [106, 107, 108], X-ray diffraction [109, 77], infrared spectroscopy [110, 111], scanning tunneling microscopy (STM) [110, 112] and atomic force microscopy (AFM) [113].

## 5.1 Langmuir-Blodgett films of fatty acids and phospholipids

In general, fatty acid molecules (see for example the arachidic acid molecule shown in figure 5.1(A)) in LB films arrange in the following fashion: the long aliphatic chains pack with their axes parallel to each other but not necessarily perpendicular to the substrate surface (see figure 5.1(B)), as discussed in several articles [114, 96], reviews [87, 88] and monographs [75, 76, 115]. The  $C_2H_4$  units form a sub-lattice with three possible different symmetries: orthorhombic (R), monoclinic (M) or triclinic (T). There are a number of possible variations of the sub-cell structure depending on the relative displacement of adjacent molecules, labeled by Miller indices of the interface layers. Moreover, depending on the nature of the substrate (for example, hydrophobic

or hydrophilic), and methods of interfacial preparation (for example, pH-value) the structure can vary.

The molecular structure of phospholipids (see for example dimyristoyl phosphatidic acid, i.e., DMPA, shown in figure 5.1(A)) is similar to that of fatty acids, but with some differences: two aliphatic chains instead of one, and a different head-group. It is found that phospholipids organize in a two-dimensional hexagonal lattice where the aliphatic chains pack parallel to each other and perpendicular to the surface [106, 107, 108, 110, 111], as shown in figure 5.1(B). The structure of the  $C_2H_4$  subunit cell is similar to that of the fatty acids.

Our observed diffraction patterns for these LB films of fatty acids and phospholipids are directly the result of the  $C_2H_4$  subunit cell because of the covered  $s$ -range,  $s$  being the magnitude of the momentum transfer vector between the incident electron and the scattered electron. Different arrangements of the subunit cell can be uniquely distinguished by the measured lattice parameters and systematic absences of certain Bragg spots. In this way we are able to establish the subunit cell structure, the in-plane orientation of the subunit cell with respect to the silicon surface and the out-of-plane direction of the aliphatic chains (i.e., inclination). Figure 5.2 depicts a schematic view of an orthorhombic  $C_2H_4$  subunit cell — the depicted structure is from our diffraction analyses given below.

The thermal behavior of such films is of particular interest, especially when considering their two-dimensional structure on the substrate. Early studies of fatty acids have shown the onset of melting far below the bulk melting temperature and in multiple steps [116, 117, 118, 119, 120, 121, 122]. AFM has elucidated the two-dimensional melting and the structures involved [123, 124]. Multiple step melting was also observed in X-ray diffraction studies [125]. The transition from two-dimensional to three-dimensional melting in these fatty acid films, upon increasing the number of deposited layers, has been examined in a number of studies [126, 127, 128].

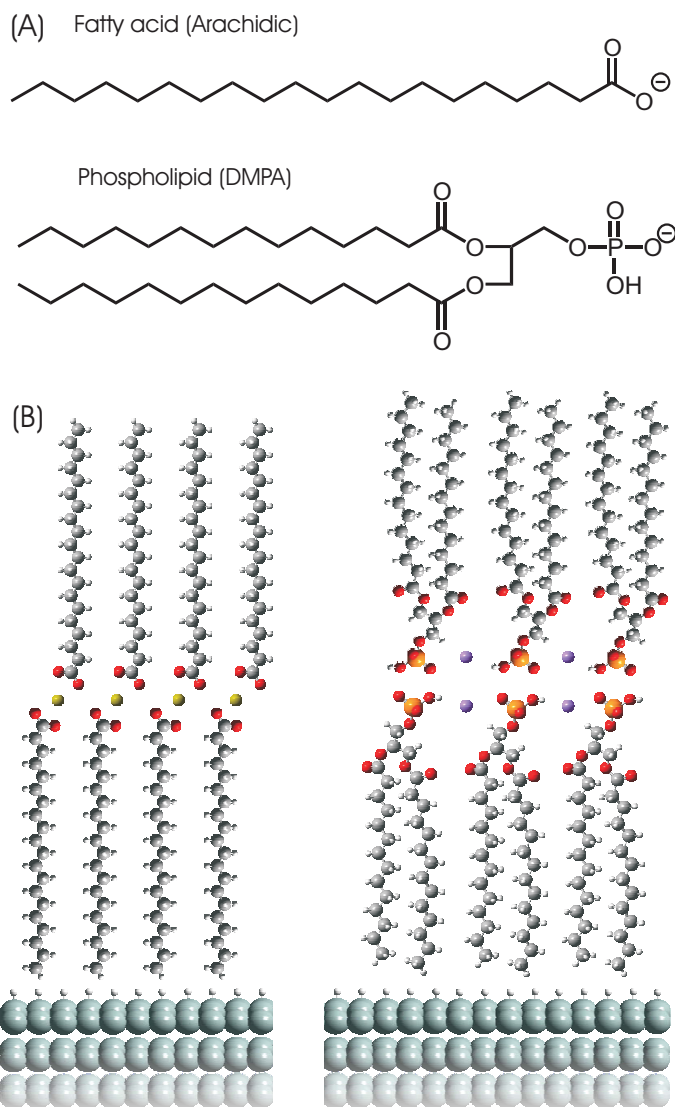


Figure 5.1: Structure of crystalline adsorbates of fatty acids and phospholipids. (A) The molecular structure of arachidic acid and DMPA. (B) Schematic side view of the two adsorbates on a hydrogen-terminated silicon(111) substrate. For the phospholipid and fatty acid, we show the bridging through the ions (salt); for the fatty acid, depending on pH, both the neutral and salt forms are present in the film [28, 29, 71].

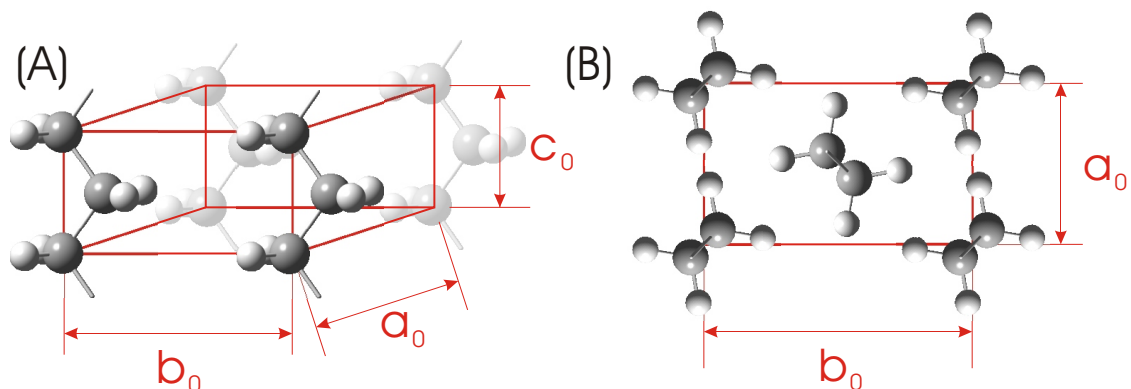


Figure 5.2: Structure of the orthorhombic  $C_2H_4$  subunit cell. (A) The orthorhombic  $C_2H_4$  subunit cell of aliphatic chains with lattice parameters  $a_0$ ,  $b_0$  and  $c_0$ . The chain at the center was omitted for clarity. (B) Top view of the orthorhombic subunit cell with lattice parameters  $a_0$  and  $b_0$  [28, 29, 71].

## 5.2 Preparation of layers by LB deposition

The substrate for all investigated samples was silicon(111). The surface was treated just before deposition, to be either hydrophilic or hydrophobic according to standard methods. Hydrophilic silicon surfaces were prepared by cleaning and oxidation with an RCA-1 solution. For the hydrophobic surfaces, subsequent etching of the oxide surface was made in a 40%  $NH_4F$  solution for 15–20 minutes in order to obtain the Si(111):H surface.

The deposition of the fatty acids and the phospholipids are in the so-called Y-geometry, i.e., head-to-head and tail-to-tail. For a hydrophilic surface, the first layer is attached to the surface by its hydrophilic head group; whereas for a hydrophobic surface, the first layer is attached by its hydrophobic tail. Since the film is always terminated by a hydrophobic tail, only odd numbered multilayers can be obtained for a hydrophilic substrate and even numbered multilayers for a hydrophobic substrate. We found that in order to achieve good film quality it was mandatory to prepare the LB films immediately after hydrogen-termination, because the hydrophobic silicon surface is unstable in air.

Arachidic acid (eicosanoic acid,  $C_{19}H_{39}COOH$ ) was purchased from Aldrich and used without further purification (see figure 5.1(A)). The fatty acids were spread

from a chloroform solution. Prior to compression to the final deposition pressure, we allowed 20 minutes for complete evaporation of the solvent. For all samples the deposition took place in a NIMA LB trough at a dipping speed of 1 mm/min. The used subphase was an aqueous  $\text{CaCl}_2$  solution ( $c[\text{CaCl}_2] = 0.5$  mmol/liter, Millipore Water), which was adjusted to the desired pH value with aqueous diluted NaOH.

To study the influence of film thickness and dipping conditions, we prepared multiple samples of LB films at different pH values and dipping pressure. Two deposition pressures,  $\pi = 10$  mN/m and  $\pi = 29$  mN/m, were chosen for bilayer deposition. Although they gave the same condensed phase for the Langmuir films, it is found that deposition of fatty acid films with more than two layers failed at  $\pi = 10$  mN/m. Here, we present selected bilayer samples deposited at  $\pi = 10$  and 29 mN/m, and pH = 6.4,  $\sim 7$  and 9; and selected samples of 4- and 8-layer films deposited at  $\pi = 29$  mN/m, and pH = 6.4,  $\sim 7$  and 9. At the pH values of 6.4 and 7, about 60% to 80% of the arachidic acid is deposited as the corresponding calcium salt, while at pH = 9, 100% of the arachidic acid is deposited as the salt [129].

To ensure a high sample quality the isotherms for the precursor Langmuir film and the transfer ratios upon deposition were routinely recorded. Furthermore, the morphology of the Langmuir film at the air-water interface was monitored with a Brewster Angle Microscope. For our dipping conditions, the Langmuir films were very uniform and did not show any macroscopic holes or multilayer islands.

In general, we recorded diffraction patterns of the LB films along two directions, which are perpendicular to each other. These correspond to the  $[11\bar{2}]$  and  $[\bar{1}10]$  zone axes of the underlying silicon substrate (see figure 5.3(A)), as evidenced from the diffraction patterns at high  $\theta_i$ 's. We denote these two directions with the azimuthal angle  $\phi = 0^\circ$  for  $[11\bar{2}]$  and  $\phi = 90^\circ$  for  $[\bar{1}10]$ , respectively. Note, however, that we also have the ability to record diffraction patterns around these  $\phi$  values in a range of at least  $\pm 30^\circ$ . The deposition of the LB films was along either of these fundamental axes and accordingly we can distinguish a parallel ( $\parallel$ ) or a perpendicular ( $\perp$ ) dipping direction (see figure 5.3(B)). However, it is the silicon surface, rather than the dipping direction, which determines the structure and orientation of the fatty acid subunit

cell on the substrate, as discussed below.

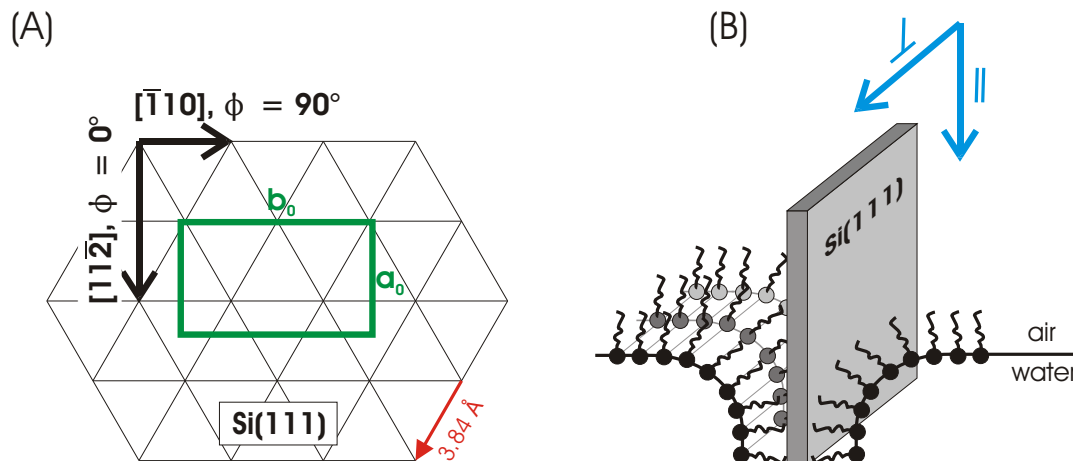


Figure 5.3: Directions of dipping, observation and subunit cell orientation. (A) Si(111):H surface lattice and the fatty acid  $C_2H_4$  subunit cell, as observed in the diffraction experiments. (B) Deposition of a LB film results in two distinguishable directions: parallel ( $\parallel$ ) and perpendicular ( $\perp$ ) to the dipping direction [71].

For the phospholipids, 1,2-Dimyristoyl-*sn*-glycero-3-phosphate monosodium salt (dimyristoyl phosphatidic acid, DMPA) was purchased from Aldrich and used without further purification (see figure 5.1(A)). The lipids were spread from a chloroform/methanol (3:1) solution, and the subphase used was Millipore water containing sodium ions at pH = 5.5. The deposition took place in a NIMA LB trough at a dipping pressure of  $\pi = 29$  mN/m and a dipping speed of 1 mm/min. Film quality measurements were routinely recorded, as described above.

We prepared monolayers of dimyristoyl phosphatidic acid (DMPA) on a hydrophilic surface; the polar head groups are involved in bonding to the substrate. For the bilayers of DMPA, a hydrophobic substrate was utilized, in a similar fashion to the fatty acid samples. We used a hydrophilic oxide-terminated silicon(111) surface for the deposition of the monolayer and hydrophobic hydrogen-terminated silicon(111) surfaces for the bilayer. As in the case of the fatty acids, the deposition is in the Y-geometry.

Immediately after deposition the samples were transferred to ultrahigh vacuum

(UHV,  $\sim 10^{-10}$  torr), where all the experiments were carried out. The LB films are stable under electron exposure, as evidenced by the absence of change or deterioration in the quality of the static diffraction patterns. However, prolonged laser irradiation and increased static sample temperature can lead to change or even loss of the diffraction patterns, as described below.

### 5.3 Fatty acid bilayers structure

The static diffraction patterns of bilayer films are shown in figure 5.4(A), (B) and (C). The panels are for LB films prepared at different conditions but all observed by UEC, i.e., recorded with ultrashort electron pulses, but without the laser heating pulse. The top panels show the diffraction patterns observed at  $\phi = 0^\circ$ , while the bottom ones show diffraction patterns observed at  $\phi = 90^\circ$ , all at low incidence angles  $\theta_i < 1^\circ$ . Panel (A) displays the diffraction patterns for the bilayer deposited at pH = 9 and  $\pi = 10$  mN/m when dipping occurred along the  $[11\bar{2}]$  direction of silicon. Panel (B) displays diffraction patterns for the bilayer deposited at pH = 6.4 and  $\pi = 29$  mN/m when dipping occurred along the  $[\bar{1}10]$  direction of silicon. Panel(C) displays diffraction patterns for the bilayer deposited at pH  $\simeq 7$  and  $\pi = 29$  mN/m when dipping occurred along the  $[\bar{1}10]$  direction of silicon.

The diffraction patterns are all composed of well resolved Bragg spots. This is the result of a high quality crystalline structure of the bilayers. The rectangular arrays of spots are perpendicular to the shadow edge. It follows that the aliphatic chains pack with their chain axes parallel to each other and perpendicular to the substrate surface.

In figure 5.4, the bright spots above the shadow edge (not indexed) are due to the main reflection beam Si(00) from the substrate silicon. This was confirmed from the  $\theta_i$  dependence (rocking curve) which shows large changes for these bright spots but not for the bilayer adsorbate. Figure 5.5 depicts this behavior for the substrate and for the bilayer deposited at  $\pi = 10$  mN/m and pH = 9, and whose static diffraction patterns at small  $\theta_i$ 's are shown in figure 5.4(A). It is clear that while the LB(002)

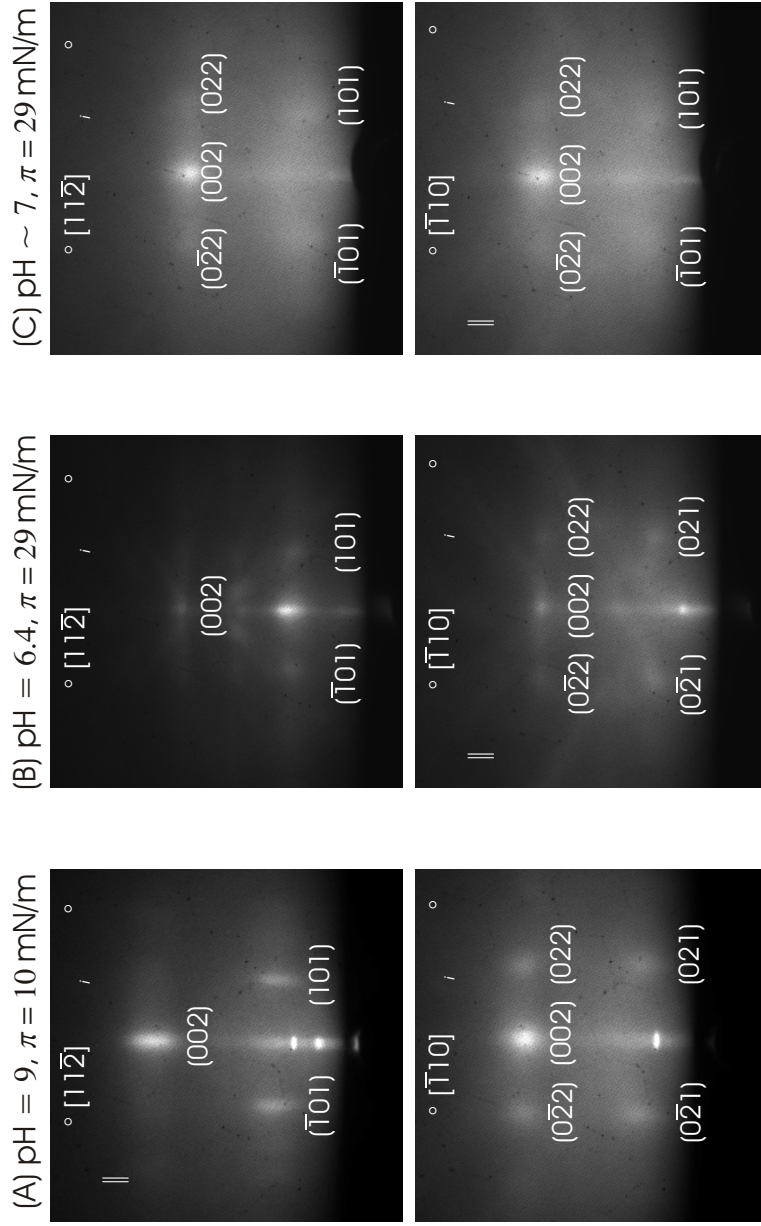


Figure 5.4: Static diffraction patterns of fatty acid bilayers at  $T = 295$  K. The  $s$  range for all diffraction patterns is from  $-0.6$  to  $+0.6 \text{ \AA}^{-1}$  in the horizontal direction and from  $0$  to  $+1.2 \text{ \AA}^{-1}$  in the vertical direction. (A) Diffraction patterns for the bilayer deposited at pH = 9 and  $\pi = 10$  mN/m, where the incidence angle is  $\theta_i = 0.8^\circ$  for  $\phi = 0^\circ$  and  $\phi = 90^\circ$ . (B) Diffraction patterns for the bilayer deposited at pH = 6.4 and  $\pi = 29$  mN/m where the incidence angle is  $\theta_i = 0.8^\circ$  for  $\phi = 0^\circ$  and  $\theta_i = 0.9^\circ$  for  $\phi = 90^\circ$ . (C) Diffraction patterns for the bilayer deposited at pH  $\simeq 7$  and  $\pi = 29$  mN/m where the incidence angle is  $\theta_i = 0.4^\circ$  for  $\phi = 0^\circ$  and  $\phi = 90^\circ$ [71].

spot remains at the same  $s$  position (near  $s = 0.8 \text{ \AA}^{-1}$  in figure 5.5), the Si(00) peak position changes periodically with  $\theta_i$ , showing the higher orders of the Si(111) Bragg diffraction.

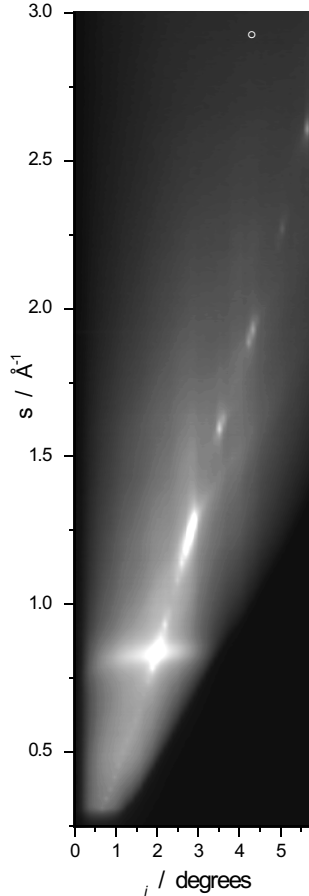


Figure 5.5: Experimental rocking curve for the  $z$ -component of the scattering vector  $s$  (from  $+0.25$  to  $+3.0 \text{ \AA}^{-1}$ ) vs. incidence angle  $\theta_i$  ( $0$  to  $5.85^\circ$ ) at  $\phi = 90^\circ$ , showing the (002) peak (see diffraction near  $s = 0.8 \text{ \AA}^{-1}$ ) of the bilayer and (00) peak of the Si(111) surface (at higher  $s$ -values) [28, 71].

The rocking curves —  $\theta_i$  changes — give insight into the overall order of the bilayer, and similarly the  $\phi$  changes. The patterns do not change considerably when rotated in a range of  $\pm 14^\circ$  about both  $\phi = 0^\circ$  and  $\phi = 90^\circ$  direction. The Bragg spots remain at their positions as shown in figure 5.4; only the intensities undergo a small change. Further increase of the angle  $\phi$  results in extension of the Bragg spots into lines parallel to the shadow edge. These behaviors, as well as the rectangular arrays of the spots suggest that the diffraction patterns are formed by electrons transmitted

through the bilayer (see section 3.1). It also infers that the fatty acid bilayers are textured samples. There are small domains of the crystalline fatty acid molecules. While they have the same out-of-plane direction with all the chains perpendicular to the substrate surface, they have slightly different in-plane orientations.

The rocking curve indicates two important points to be made regarding differences in two-dimensional and three-dimensional crystal behavior. First, at large  $\theta_i$  values, the electrons penetrate the bulk and we observe the higher orders of Bragg diffraction of the substrate. In fact it is from these high-order diffractions that we can determine the lattice spacing of the used substrate. At lower values of  $\theta_i$ , the spots are stretched diagonally, making the substrate spacing less accurate to determine. At the lowest  $\theta_i$ , the pattern is dominated by the adsorbate diffraction features. The behavior with  $\theta_i$  of an adsorbate spot shows insensitivity in the region of  $\theta_i$  studied.

This brings to focus the second point regarding measurements of rocking curves. Unlike three-dimensional crystals, two-dimensional systems exhibit “rods” in the diffraction reciprocal space. As the layers build up in thickness, the rods are modulated by the inverse chain distance of  $c_0$ . Thus, for two-dimensional systems the intensity should not change drastically with  $\theta_i$ , while for three-dimensional systems they will. From the horizontal width of our diffraction ( $\Delta s \simeq 0.06 \text{ \AA}^{-1}$ ), we obtain a nm scale coherence length. Moreover, the vertical width of  $\Delta s$  gives a maximum inhomogeneity in  $-\text{CH}_2-\text{CH}_2-\text{CH}_2-$  distances of  $\sim 20\%$ , relative to the  $2.54 \text{ \AA}$  distance of  $c_0$ .

From the positions of the Bragg spots (including systematic absences), the subunit cells were determined to be orthorhombic, with short notation of R(001). Accordingly, “R” represents the orthorhombic symmetry and (001) is for denoting the ( $ab$ ) plane of the  $\text{C}_2\text{H}_4$  subunit cell which is parallel to the substrate Si(111) surface. Basically, the vertical  $s$  spacing gives the  $c_0$  values while side diffractions give  $a_0$  and  $b_0$  for the two  $\phi$ 's, respectively. Note that the direct beam is located below the shadow edge.

Figure 5.6 shows the simulated diffraction patterns of an orthorhombic, infinite crystal of aliphatic carbon chains for the [100] and [010] direction, which are the two directions studied in the experiments. Indeed the patterns show the characteristic

spots as in figure 5.4, with the same symmetry, spacings and absences. Although the intensities of the calculated Bragg spots, especially for  $(\bar{2}02)$  and  $(202)$ , do not reproduce those measured. This is because the calculation was made for an infinite array of chains in the crystal and the underlying substrate and the headgroups were not taken into account, and it was not scaled with the  $s$ -decay of diffraction.

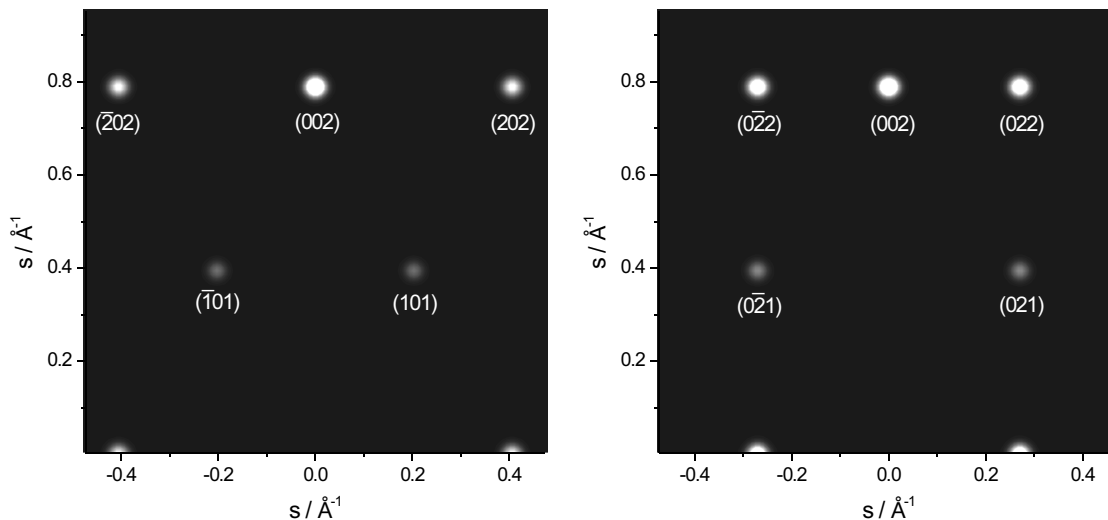


Figure 5.6: Calculated diffraction patterns of an orthorhombic, infinite crystal of aliphatic carbon chains observed along the  $[100]$  and  $[010]$  direction, respectively. The subunit cell lattice parameters used are  $a_0 = 4.93 \text{ \AA}$ ,  $b_0 = 7.4 \text{ \AA}$  and  $c_0 = 2.534 \text{ \AA}$ . The space group is  $V_h^{16}$  (Pnam) [71].

The determined lattice parameters of the different bilayer structures are summarized in Table 5.1. The lattice parameters  $c_0$ , which result from the vertical  $s$ -spacing of the Bragg spots, have the same magnitude for all three samples. They agree well with the theoretical value of  $2.54 \text{ \AA}$ , which follows from a simple geometrical consideration for an aliphatic chain with bond distances  $r_{c-c} = 1.53 \text{ \AA}$  and angle  $\angle_{c-c-c} = 112^\circ$ . The  $c_0$  value represents the distance between  $\text{CH}_2$  planes, and it holds true for the 4- and 8-layer samples, as shown below.

The determined  $a_0$  and  $b_0$  values vary for different conditions and range for  $a_0$  from  $4.7$  to  $4.9 \text{ \AA}$ ; and for  $b_0$  from  $8.0$  to  $8.5 \text{ \AA}$ . These values differ somewhat from the theoretical values of  $a_0 = 4.96 \text{ \AA}$  and  $b_0 = 7.4 \text{ \AA}$  [115], which were estimated, by

	<b>pH = 9,</b> $\pi = 10$ mN/m <b>(figure 5.4(A))</b>	<b>pH = 6.4,</b> $\pi = 29$ mN/m <b>(figure 5.4(B))</b>	<b>pH <math>\simeq 7</math>,</b> $\pi = 29$ mN/m <b>(figure 5.4(C))</b>
$\mathbf{a}_0/\text{\AA}$	4.7	4.9	4.7
$\mathbf{b}_0/\text{\AA}$	8.0	8.3	8.5
$\mathbf{c}_0/\text{\AA}$	2.54	2.59	2.57

Table 5.1: Lattice parameters determined for the fatty acid bilayer samples prepared differently.

purely geometrical considerations, for the ideal case of closest packed arrays of infinite aliphatic chains. The difference can be explained by the fact that the theoretical values do not take into account the carboxylic end groups of fatty acids. Moreover the substrate and the deposition conditions all have an important role in the order at the interface.

While the parameter  $a_0$  has a similar value for all bilayer samples,  $b_0$  is slightly larger for the samples prepared at lower pH values (pH = 6.4 and  $\sim 7$  vs. pH = 9) and higher pressures ( $\pi = 29$  mN/m vs.  $\pi = 10$  mN/m). Though the pressure has little effect on the molecular packing in this range, as observed in the  $\pi$ -area isotherm, it has been observed that the pH value has a rather strong influence on the overall packing of the LB film. An increase of the pH value is believed to pull the head-groups closer together and support a nontilted LB film structure [92]. In the sample deposited at pH = 9, virtually all fatty acid molecules are in their salt form, which leads to a slightly closer packing compared to the deposited structures at lower pH values, where only 60%–80% of the fatty acids are in their salt form [129].

By comparing figure 5.4(A) and (B) we notice that the orthorhombic subunit cell is always aligned with its  $b_0$ -axis along the  $[\bar{1}10]$  direction of the Si(111) surface and, thus, the  $a_0$ -axis is along the  $[11\bar{2}]$  direction, regardless of the dipping direction. This influence of the substrate is expected and has been noted for hydrogen-terminated Si(111) [130]. In this context, it is worth noting that the structure of the precursor Langmuir film, i.e., the monolayer on water, has relatively less influence on the structure of deposited LB films [102, 88, 131].

The influence of the substrate explains the orientational ordering of the adsorbate

on the substrate, as is illustrated in figure 5.3(A). The length of one repetitive unit along the  $[\bar{1}10]$  and  $[11\bar{2}]$  direction of silicon substrate, which are 3.84 and 6.65 Å in real space, respectively, are to be compared with  $b_0$  and  $a_0$  of the adsorbate layer. Two repetitive units along the  $[\bar{1}10]$  direction correspond to 7.68 Å, a value which is close to the observed  $b_0 = 8.0$  Å (and 8.3 Å). The length mismatch is only 4% (and 8%). If  $b_0$  was oriented along the  $[11\bar{2}]$  direction, then, because the distance of repetitive units is 6.65 Å, the mismatch would be 20% to 25%. The disagreement between  $a_0$  of the orthorhombic subunit cell and the lattice parameters of silicon is  $> 20\%$  in either orientation. It is therefore reasonable to explain, because of this length correlation, the  $b_0$  axis alignment along the  $[\bar{1}10]$  direction of the substrate, and thus the orientation is independent of the dipping direction and the precursor Langmuir film structure.

This orientation is also sensitive to substrate structure. In figure 5.4(C), the observed diffraction patterns form no “perfect” rectangular array of Bragg spots and the diffraction patterns in the two distinct directions of  $\phi = 0^\circ$  and  $\phi = 90^\circ$  are similar and differ only in intensity and sharpness of the spots. This is in stark contrast to the distinct diffraction patterns in the two directions for the samples shown in figure 5.4(A) and (B) and the predicted patterns in figure 5.6. Close inspection of the diffraction patterns in figure 5.4(C) reveals that they result from a superposition of the two diffraction patterns ( $\phi = 0^\circ$  and  $90^\circ$ ) displayed in figure 5.6. This loss of preferred orientation is consistent with the fact that the diffraction patterns do not change their general form upon rotation in a range of at least  $\phi = \pm 30^\circ$  in both directions. In this particular sample the absence of the alignment is believed to originate from a partial oxidization of the surface prior to dipping; hydrogen-terminated silicon surfaces are known to be easily oxidized in air.

In summary, calcium arachidate bilayers form orthorhombic structure on the hydrophobic Si(111) substrate, with the fatty acid chains aligned perpendicular to the surface. The  $C_2H_4$  subunit cell is determined to be R(001) and all the lattice parameters are extracted. Samples prepared at higher pH values showed a closer packing of the fatty acid. The substrate surface has a large influence on orientation, and in

this case the  $b_0$ -axis is along the  $[\bar{1}10]$  direction of the hydrogen-terminated Si(111) surface and the  $a_0$ -axis along the  $[11\bar{2}]$  direction.

## 5.4 Fatty acid bilayers temperature-dependent structural change

Following characterization of structures we studied the effect of substrate temperature. For the bilayer sample deposited at  $\pi = 29$  mN/m and  $\text{pH} \simeq 7$ , diffraction patterns at  $\phi = 0^\circ$  were recorded at different temperatures in the range from  $T = 100$  to 380 K; representative examples of diffraction patterns are shown in figure 5.7 for  $T = 100, 295, 333$  and 370 K. The patterns are indexed as described above and displayed on the  $T = 100$  K pattern. The diffraction pattern shows Bragg spots as in figure 5.4 and is very clear at 100 K. The patterns become more diffuse with increasing temperature; the intensity of Bragg spots decreases while the background gains intensity. At 370 K, just below the melting temperature of arachidic acid salt LB films of  $\sim 383$  K [120], the characteristic features of spots are barely visible in the patterns. This shows that the temperature increase is responsible for the enhanced thermal and inhomogeneous disorder, leading ultimately to a total randomness and breakdown of the bilayer structure at the melting point.

The relative (integrated) intensity change  $I/I_0$  of the (002) Bragg spot as a function of temperature is shown in figure 5.8(A). An intensity drop is expected by the Debye-Waller effect due to increased thermal motions of the scattering atoms with increasing temperature. These motions have direct influence on structural factors. However, it is remarkable that the intensity drop shown in figure 5.8(A) features certain temperature points at which the slope abruptly changes (shown in the inset). Such a thermal behavior is different from conventional melting of isotropic bulk materials and could be related to phase transitions, as observed with AFM [123, 124], of two-dimensional, anisotropic LB films.

In diffraction, besides the Debye-Waller intensity drop, one expects a sharp de-

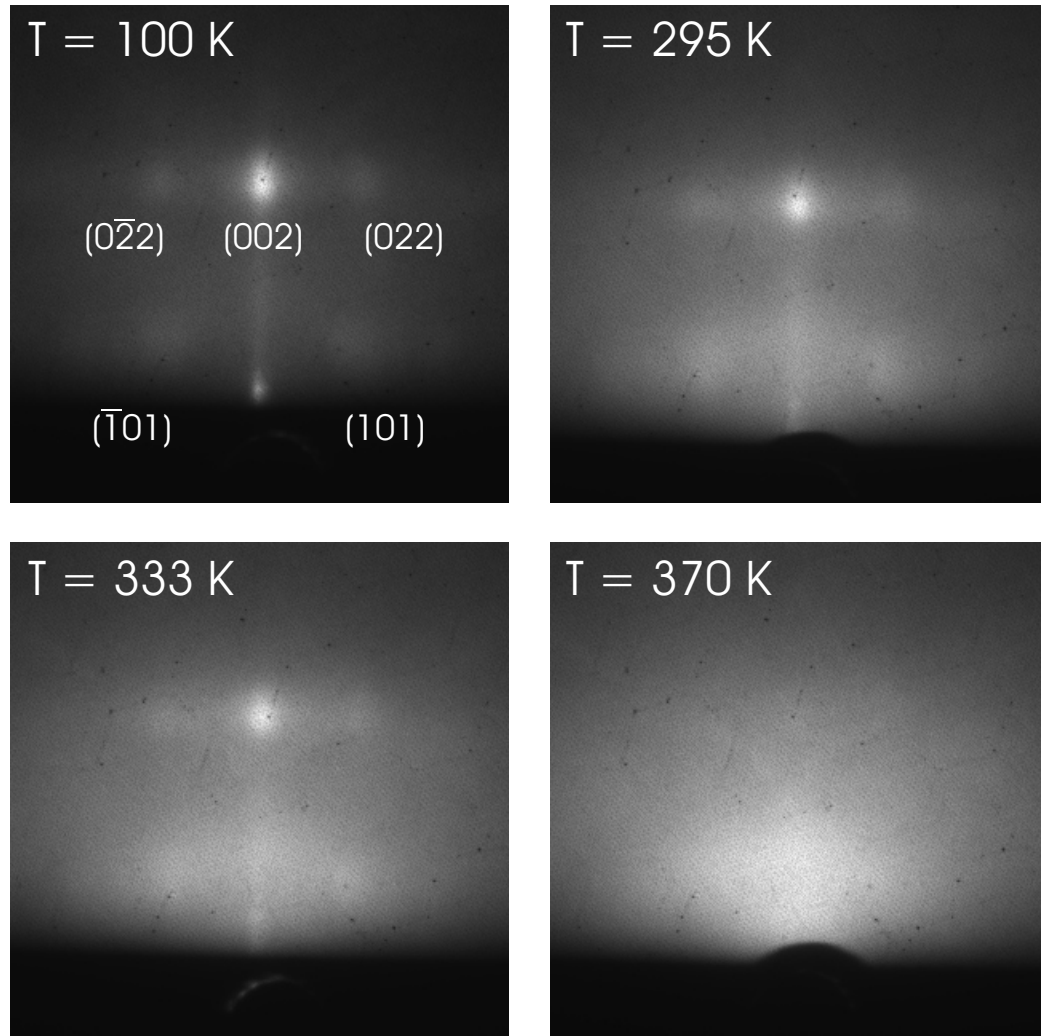


Figure 5.7: Static temperature dependent diffraction patterns for the calcium arachidate bilayer deposited at  $\text{pH} \simeq 7$  and  $\pi = 29 \text{ mN/m}$  at  $T = 100, 295, 333$  and  $370 \text{ K}$ . The patterns are observed at  $\phi = 0^\circ$  and  $\theta_i = 0.4^\circ$ . The  $s$  range for all diffraction patterns is from  $-0.6$  to  $+0.6 \text{ \AA}^{-1}$  in the horizontal direction and from  $0$  to  $+1.2 \text{ \AA}^{-1}$  in the vertical direction [71].

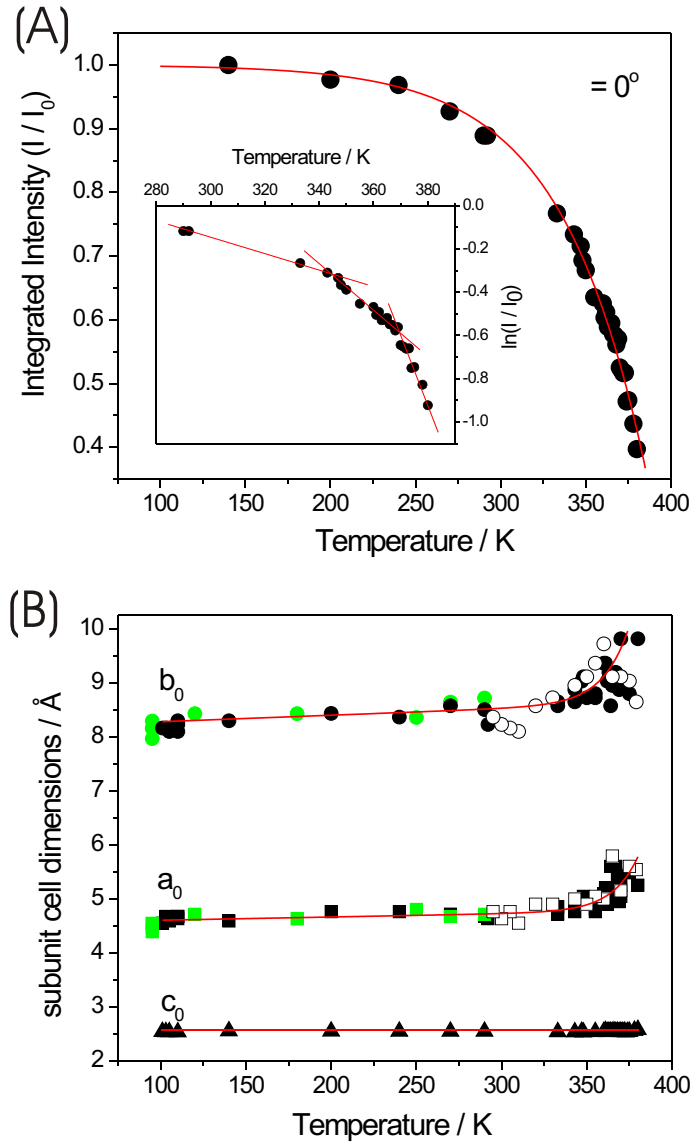


Figure 5.8: Static temperature dependence of diffraction intensity and subunit cell dimensions ( $\text{\AA}$ ) for the calcium arachidate bilayer deposited at  $\text{pH} \simeq 7$  and  $\pi = 29$  mN/m. (A) Relative intensity change  $I/I_0$  of the (002) spot in the temperature range from  $T = 140$  to 380 K observed at  $\phi = 0^\circ$  and  $\theta_i = 0.4^\circ$ . The inset emphasizes the abrupt slope changes in a plot of  $\ln(I/I_0)$  against temperature in the range from 280 to 380 K. (B) Change of the subunit cell parameters  $a_0$ ,  $b_0$  and  $c_0$  observed at  $\theta_i = 0.4^\circ$ . The black symbols represent cell parameters observed at  $\phi = 0^\circ$ , whereas the open symbols denote cell parameters observed at  $\phi = 0^\circ$  after cooling down from  $T = 380$  K. The green symbols stand for the subunit cell parameters obtained at  $\phi = 90^\circ$  from  $T = 95$  to 290 K. The red line is a guide for the eye [71].

crease in intensity if a phase transition is present, such as in conventional melting. However, this transition is only sharp if the layers are thick enough to define a three-dimensional collective behavior. For two-dimensional melting, pretransitional disordering in the form of thermally-induced random tilt and/or bending of the aliphatic chains [120] erodes the sharpness and renders the transition to occur over a wider temperature range. This picture of disorder involves several steps, first disordering of the hydrocarbon tails and then the breakdown of the head-group region, the latter occurs at the main melting point [116, 117]. Raman studies also support the presence of pretransitional regions [132].

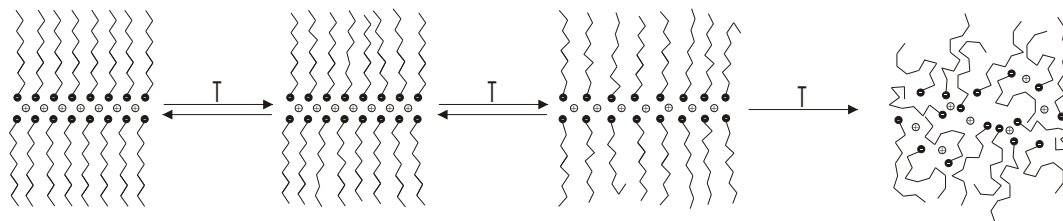
The effect of static temperature on the subunit cell parameters is shown in figure 5.8(B). With increasing temperature, the film expands along  $a_0$  and  $b_0$ , first slowly then more rapidly with an onset of  $\sim 50$  K below the bulk melting point. A similar behavior has been reported for a fatty acid salt LB film [121], however, the expansion reported here is significantly more pronounced. It should be noted that the guide for the eye (red line) has the same shape for  $a_0$  and  $b_0$  but is only shifted along the  $y$ -axis of the figure, indicating a similar expansion in  $a_0$  and  $b_0$  of  $\sim 25\%$  in the range from 100 to 380 K.

The expansion of the subunit cell in the plane parallel to the substrate surface is fully reversible as long as the sample is heated to temperatures below or near the bulk melting point and for a short time (minutes). In figure 5.8(B) the open circles and squares indicate that the initial cell parameters are retrieved after cooling down. However, the intensity of the Bragg spots recovers only partially (not shown), indicating some loss of crystalline order in the LB film. Within our accuracy no expansion is observed along  $c_0$ , i.e., along the fatty acid chains.

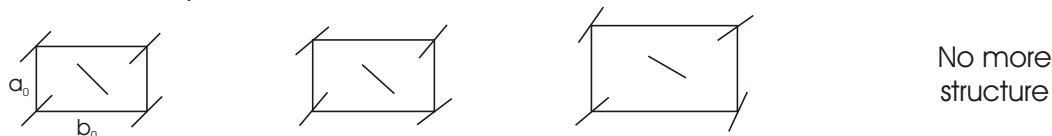
In summary, with increasing temperature we observed a pronounced loss of Bragg spot intensity, but with behavior much different from what is expected from the Debye-Waller effect for a bulk material. Rather, the behavior reflects the two-dimensional pretransitional structural changes. We also observed an in-plane expansion of the subunit cell of the chains, together with increased lateral (in-plane) disorder, as evidenced in the buildup of background scattering. At the same time

the degree of order in the carbon chains decreases. These processes are partially reversible as long as the temperature is below the main melting point. Beyond the main melting point the head-group region breaks down and the crystalline order of the adsorbate is lost. A structural picture is depicted in figure 5.9.

Structural changes: Static thermal expansion and inhomogeneity



Anharmonicity effect:



Vibrational amplitude effect:

High Bragg Intensity      Lower Bragg Intensity      Lowest Bragg Intensity      No more Bragg spots

Figure 5.9: Schematic view of the static thermal behavior for changes of a bilayer with temperature increase [71].

## 5.5 Fatty acid multilayers structure

The static diffraction patterns recorded at room temperature for 2-, 4- and 8-layer samples deposited at  $\text{pH} = 6.4$  and  $\pi = 29 \text{ mN/m}$  are shown in figure 5.10. The upper panels show the diffraction patterns observed along the silicon  $[11\bar{2}]$  direction ( $\phi = 0^\circ, \perp$ ), and the lower panels show the patterns along the silicon  $[\bar{1}10]$  direction ( $\phi = 90^\circ, \parallel$ ). All diffraction patterns take the form of rectangular arrays of spots, and are indexed from the positions of the Bragg spots, as shown for the bilayer (see figure 5.4(B) and also figure 5.6). The indexing is the same for the 4- and 8-layer samples, but omitted in the figure for clarity. The fatty acid molecules arrange in an

orthorhombic R(001) packing with the subunit cells  $b_0$ -axis aligned along the silicon  $[\bar{1}10]$  direction for all samples independent of layer thickness.

The extracted subunit cell parameters are summarized in Table 5.2. Within the error bars, the 2- and 4- layer samples have the same lattice parameters, possibly because of the strong influence of the underlying substrate. With more deposited layers this influence becomes weaker and results in the slight expansion of  $b_0$  in the 8-layer sample by  $\sim 8\%$  compared to the 2-layer sample;  $a_0$  remains unaltered in the 8-layer sample. This can be explained as follows: because  $b_0$  is the direction of better match (stronger interaction) with the substrate the change is larger in this direction as layers become further away from the surface. On the other hand, an increase of “defects” and holes, when multiple layers are deposited [88], can also lead to a relaxation of the observed film structure. The Bragg spots are not as sharp for the 8-layer sample as they are for the 2- and 4-layer ones, and this behavior is consistent with some loss of order of crystallinity to randomly oriented crystallites, as has been observed for behenic acid multilayers [103, 104]. However, the aliphatic chains are still aligned nearly perpendicular to the sample surface and keep their stacked arrangement.

	<b>2-layer</b>	<b>4-layer</b>	<b>8-layer</b>
$\mathbf{a}_0/\text{\AA}$	4.86	4.87	4.85
$\mathbf{b}_0/\text{\AA}$	8.28	8.33	8.91
$\mathbf{c}_0/\text{\AA}$	2.59	2.54	2.54

Table 5.2: Lattice parameters for the 2-, 4- and 8-layers deposited on the hydrophobic substrate of Si(111) surface: pH = 6.4 and  $\pi = 29$  mN/m.

Before IR laser ( $\lambda = 800nm$ ) irradiation, the 8-layer sample gives the diffraction pattern shown in figure 5.11(A) for  $\phi = 0^\circ$ . Upon laser annealing this sample recovers the diffraction pattern shown in figure 5.11 and is that of figure 5.10. The pattern before annealing is basically characteristic of the film but along an “inclined line” (by  $\sim 20^\circ$ ), reflecting partial inclination of the chains; the annealing leads to the disappearance of such a tilt and the structure becomes that of a perpendicular chain geometry. However, another 8-layer LB film prepared at pH  $\simeq 7$  and  $\pi = 29$  mN/m,

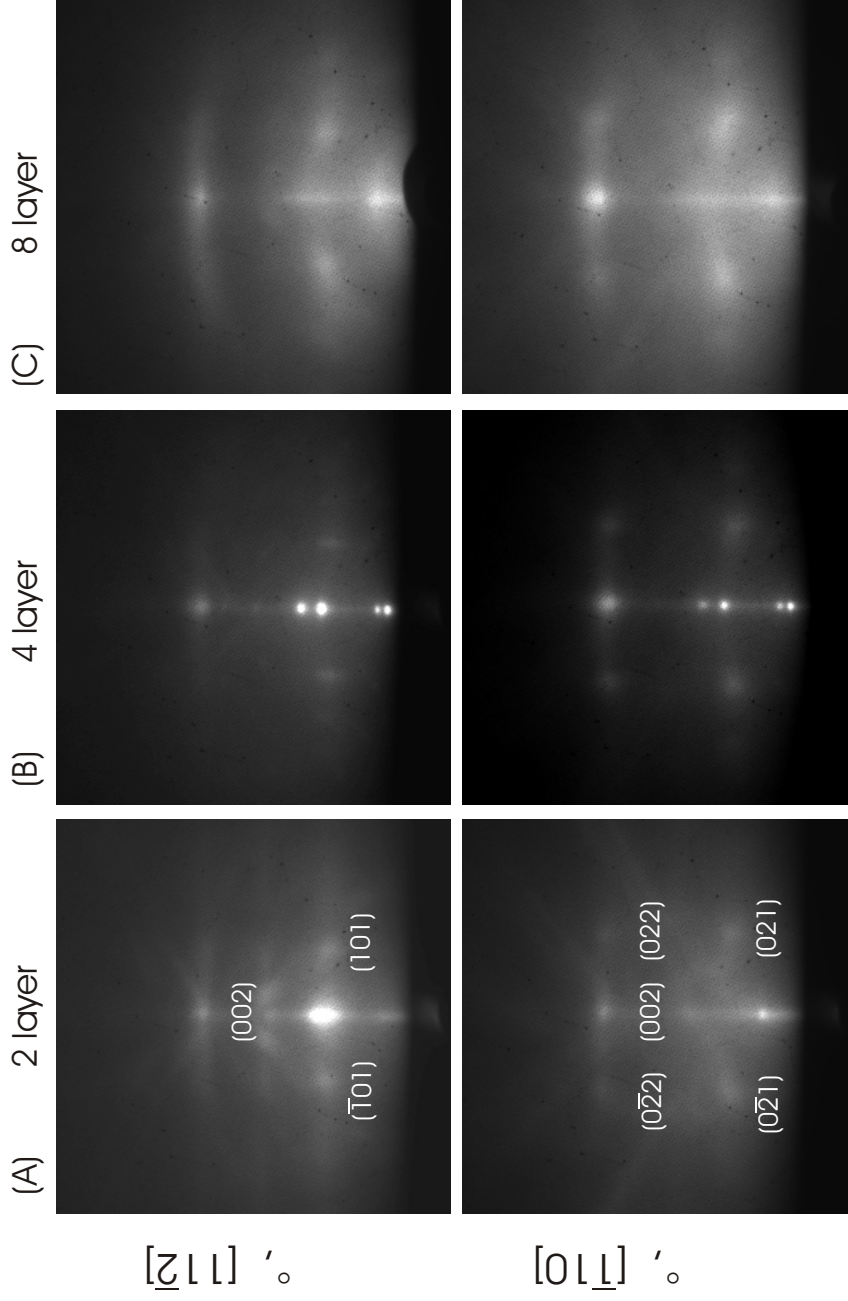


Figure 5.10: Diffraction patterns obtained for the calcium arachidate LB films of (A) 2-, (B) 4- and (C) 8-layers deposited at  $\text{pH} = 6.4$  and  $\pi = 29$   $\text{mN/m}$ . Deposition occurred along the  $[\bar{1}10]$  direction of silicon. The incidence angles for the patterns observed at  $\phi = 0^\circ$  (upper panels) are  $\theta_i = 0.8^\circ, 0.8^\circ, 0.5^\circ$  for 2-, 4-, and 8-layers, respectively, and for  $\phi = 90^\circ$  (lower panels) they are  $\theta_i = 0.9^\circ, 0.4^\circ, 0.4^\circ$ . The  $s$  range for all diffraction patterns is from  $-0.6$  to  $+0.6$   $\text{\AA}^{-1}$  in the horizontal direction and from  $0$  to  $+1.2$   $\text{\AA}^{-1}$  in the vertical direction [71].

although showed clearly the partial inclination, it did not change upon laser irradiation, as is apparent in the static diffraction pattern shown in figure 5.11(B), which shows the persistence of the inclined feature. Two parallel lines with a tilt angle of  $\sim 10^\circ$  to the right were observed at both  $\phi = 0^\circ$  and  $\phi = 90^\circ$ .

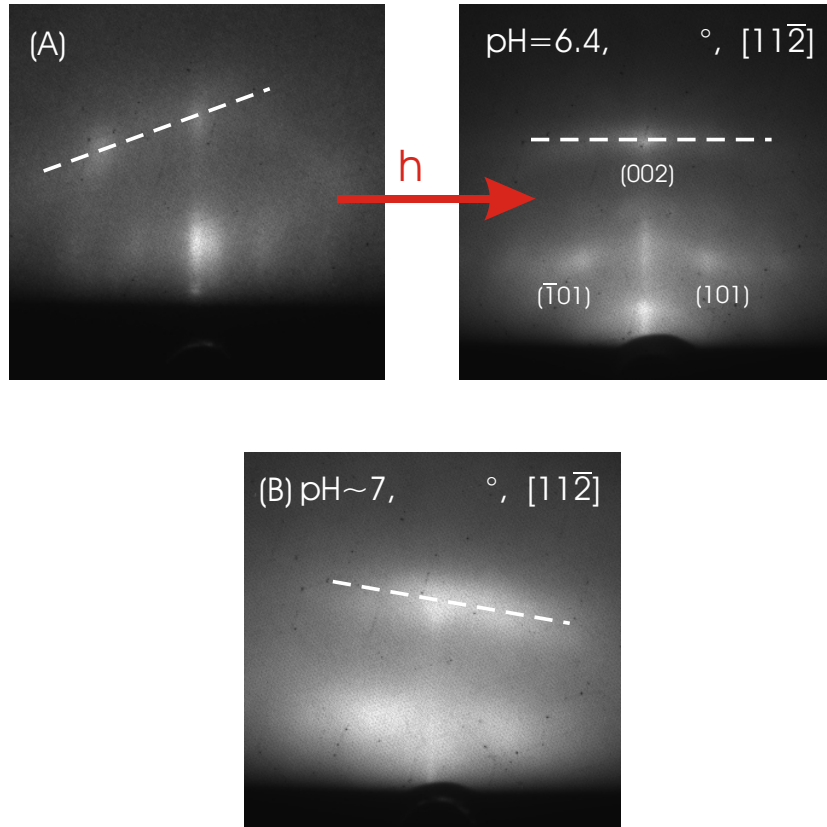


Figure 5.11: Inclined diffraction patterns for 8-layer samples at  $\phi = 0^\circ$ , with the  $s$ -range from  $-0.6$  to  $+0.6 \text{ \AA}^{-1}$  in the horizontal direction and from  $0$  to  $+1.2 \text{ \AA}^{-1}$  in the vertical direction. (A) The 8-layer sample deposited at  $\text{pH} = 6.4$  and  $\pi = 29 \text{ mN/m}$  shows a partial inclination of  $\sim 20^\circ$  to the left (dotted line), which vanishes after laser irradiation. The incidence angle is  $\theta_i = 0.4^\circ$ . (B) The 8-layer sample deposited at  $\text{pH} \simeq 7$  and  $\pi = 29 \text{ mN/m}$  shows a partial inclination of  $\sim 10^\circ$  to the right, which for this sample is stable with laser irradiation. The incidence angle is  $\theta_i = 0.5^\circ$  [71].

The spacing between the inclined lines along the tilted direction gives again  $c_0 = 2.54 \text{ \AA}$ , consistent with results to all samples studied. Besides the smeared lines some Bragg spots are apparent, most notably the (002) reflection, however lateral order could not be extracted. This change into an inclined chain structure is consistent

with results showing that LB films composed of a few layers of fatty acid salts have an upright arrangement, whereas multilayers possess an inclined carbon chain geometry [88].

In summary, the static structures of 2-, 4-, and 8-layer samples of calcium arachidate are rather similar, though inclination of the fatty acids together with an increase in disorder begins to show in the 8-layer samples. The influences of substrate orientation and interaction decreases as more layers are formed in the structure.

## 5.6 Phospholipid monolayer and bilayer structure

In figure 5.12(B) and (C), the static diffraction patterns for DMPA monolayers and bilayers are depicted, respectively. The two patterns are very similar and their strongest feature is a horizontal diffraction (curved) line, which is labeled by the Miller indices  $(hk2)$ . Since the line is basically the composite of Bragg diffractions in the second diffraction order (compared to the diffraction pattern of fatty acids shown in figure 5.12(A)), we are able to determine the subunit cell parameter  $c_0$  to be 2.54 Å from the  $s$  value in the vertical direction. This again is expected because of the covalent  $-\text{CH}_2-\text{CH}_2-\text{CH}_2-$  distances involved in the aliphatic chains of DMPA, which are essentially the same as in arachidic acid (see figure 5.1(A)). The patterns indicate that the aliphatic chains are packed parallel to each other and are aligned nearly perpendicular to the surface.

However, long-range in-plane order was not observed, as we could not resolve separate Bragg spots, as we did for the fatty acids. This limited resolution may be due to the fact that the more complex chemical structure of DMPA does not allow the molecules to pack as easily into orthorhombic (or other symmetries) crystals over an extended area. The crystallinity of the film is more restricted; “bulk” crystals of DMPA show inclination  $\beta = 114.2^\circ$  of the carbon chains [133], whereas in the adsorbate DMPA on the substrate the chains are forced to be nearly perpendicular to the surface. Diffraction patterns also show diffuse scattering in the lower  $s$  range. The independence of the diffraction patterns on electron incidence angle  $\theta_i$  and the

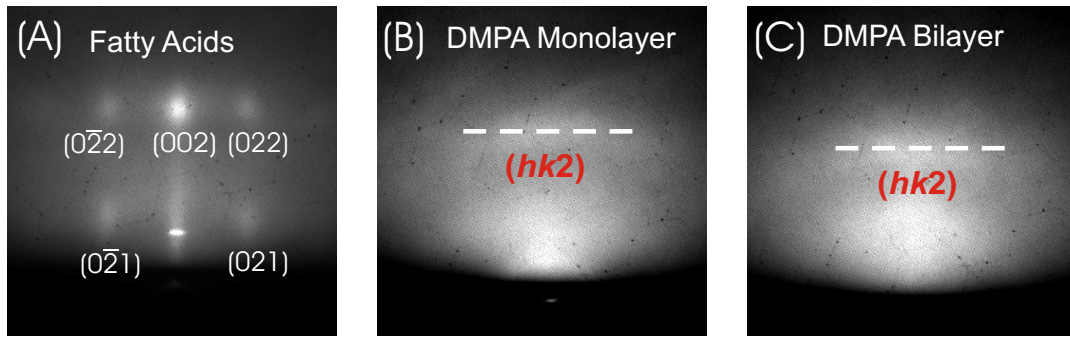


Figure 5.12: The diffraction patterns of fatty acids (A), DMPA monolayer (B) and bilayer (C) samples. The incidence angle is  $\phi = 90^\circ$  and  $\theta_i = 0.8^\circ$  for fatty acids (A),  $\phi = 90^\circ$  and  $\theta_i = 0.7^\circ$  for DMPA monolayer (B) and  $\phi = 0^\circ$  and  $\theta_i = 0.5^\circ$  for DMPA bilayer (C) [29, 71].

azimuthal angle  $\phi$  is consistent with the existence of polycrystalline domains.

## Chapter 6

# Fatty Acid and Phospholipid Crystalline Adsorbates: Ultrafast T-jump Dynamics\*

To study the dynamics of the surface adsorbates of crystalline fatty acids and phospholipids, the diffraction patterns were followed as a function of time after ultrafast laser irradiation. Earlier femtosecond spectroscopic studies have provided valuable information about the dynamics on the picosecond timescale, but could not determine the structure [134, 135]. Time-resolved X-ray diffraction studies showed a laser-induced ultrafast melting in fatty acid films above the damage threshold [136]. However, the results were not for monolayers and bilayers, and for the sample used (83 layers), a drawback is the inevitable destruction of the films. To our knowledge, the only reported nondestructive technique used to resolve the structure and dynamics is UEC.

In our experiments, the fatty acids and phospholipids have no absorption resonance at the excitation wavelength of 800nm and thus appear transparent, with the energy being absorbed solely by the silicon substrate. The mechanism of heating the substrate is discussed in chapter 4. Following the initial formation of electron hole pairs, the energy is transferred in a few picoseconds to the lattice through electron-phonon coupling, thereby virtually creating a temperature jump in the silicon substrate. Through coupling of the substrate to the fatty acid or phospholipid molecules the energy is also transferred into the adsorbate, where unique structural changes are

---

\*This chapter is based on the work presented in references [28, 29, 71].

induced at far-from-equilibrium temperatures.

At negative time delays, i.e., when the electrons arrive before the laser pulses, the observed diffraction frames are the same as those obtained at steady-state, i.e., the static diffraction patterns. The frames at negative times serve as reference for the subsequent changes with time. At positive time delays, we probe the structural changes of the adsorbate as a result of the temperature jump in the underlying substrate. For every time frame, each Bragg spot was fitted with a Voigt line shape function in the vertical and horizontal direction, respectively, after careful removal of the background, which results mainly from incoherent, inelastic and other scattering. This fitting procedure provides with precision the center position and the width as a function of time. The determination of the center position proved to be insensitive to background subtraction, because of the large intensity of diffraction spots relative to the background; for the line width accurate background removal and good signal-to-noise ratio determine the accuracy of the values obtained. The intensities of Bragg spots were obtained by gating with a window of pixels on the CCD and integrate it to give the changes with time; the gate remains the same for all frames.

## 6.1 Fatty acids structural dynamics

Figure 6.1 shows a typical time dependent diffraction difference frames of the (002) Bragg spot, with respect to the diffraction image before time zero, recorded for the bilayer film deposited at  $\text{pH} = 9$  and  $\pi = 10 \text{ mN/m}$  at low incidence angle ( $\theta_i = 0.8^\circ$ ,  $\phi = 0^\circ$ ). As expected, the diffraction difference frame at negative time delay (-20 ps) does not show any features, i.e., there is no change before time zero. Immediately after the heating pulse (0 ps and 1 ps), an intensity loss of the Bragg spots is observed, as dark spots appear in the difference frames. The change in the Bragg spots becomes more prominent over time (10–100 ps). The lower part of the peaks becomes brighter while the upper part becomes darker, showing a downward shift of the Bragg spots. With extended time delays (200–1110 ps), the difference patterns get fainter again, indicating that the peaks are moving back to their original position. This be-

havior confirms that both the heating and electron pulses, because of their ultrashort durations and fluxes, do not damage the bilayer. It should be emphasized, that the structural change is observed only in the direction perpendicular to the shadow edge of the diffraction pattern, i.e., in the vertical direction of the momentum transfer  $s$ -coordinate. A similar behavior is observed for all diffraction of all the fatty acid films studied, regardless of  $\phi$  and  $\theta_i$ .

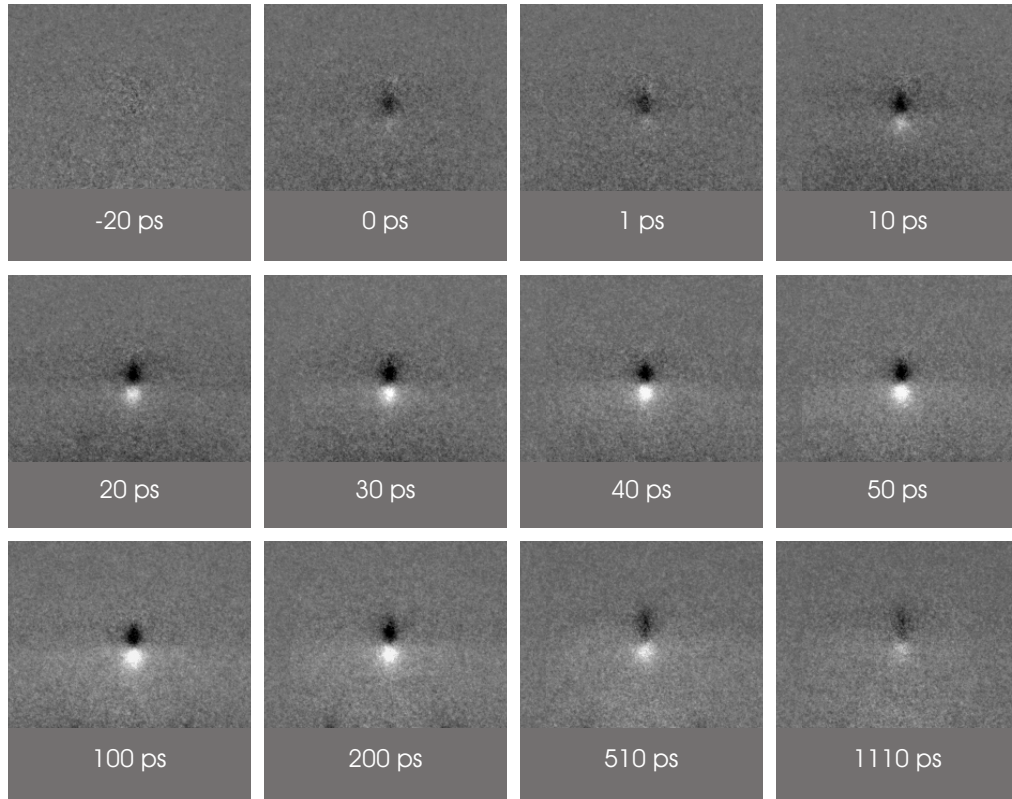


Figure 6.1: Diffraction difference frames of the (002) Bragg spot at various time delays for the bilayer film deposited at  $\text{pH} = 9$  and  $\pi = 10 \text{ mN/m}$ , obtained at low incidence angle ( $\theta_i = 0.8^\circ$ ,  $\phi = 0^\circ$ ) [28, 71].

In figure 6.2, we show examples of the detailed analysis of the (002) Bragg spot, here for the 4-layer sample deposited at  $\text{pH} = 6.4$  and  $\pi = 29 \text{ mN/m}$ . As depicted in figure 6.2 (A), for a delay time as long as  $t = 1000 \text{ ps}$  the fit of the Bragg spot with a Voigt line shape function in the vertical direction is very good; the same is true for all other time delays. From such excellent data sets the exact center position change, the

relative integrated intensity and full width at half maximum (FWHM) were obtained as a function of time (shown in figure 6.2(B), (C) and (D), respectively). We observed similar trends for all Bragg spots in each sample under investigation. We note that each Bragg spot was found to fit well to a Voigt line shape function in the horizontal or vertical direction after careful removal of the background. However, for the data sets with less than optimal quality samples, the line width changes with time were sometimes obscured by the noise.

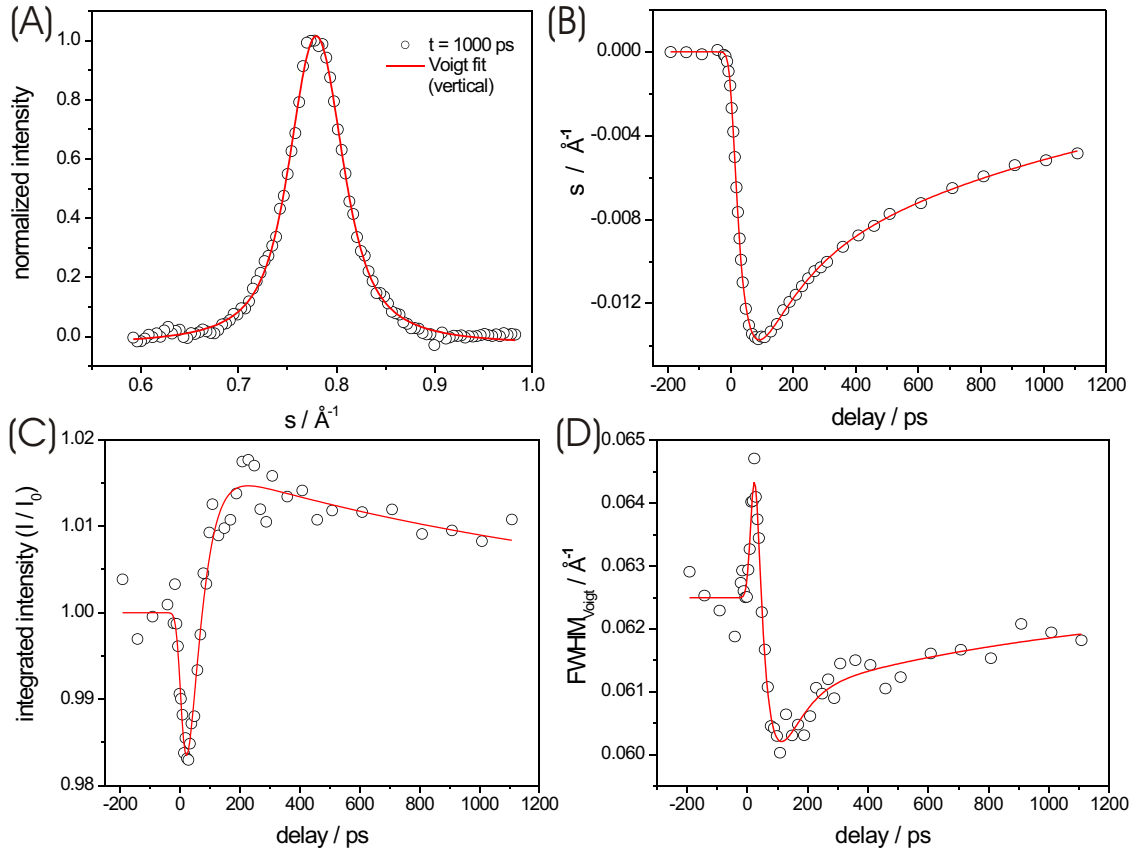


Figure 6.2: Full analysis of the (002) Bragg spot of the 4-layer calcium arachidate sample deposited at  $\text{pH} = 6.4$  and  $\pi = 29$  mN/m for  $\phi = 90^\circ$  and  $\theta_i = 0.4^\circ$ . (A) Representative Voigt fit of the normalized (002) Bragg spot in the vertical direction at  $t = 1000$  ps, after background removal. (B) The momentum transfer change  $\Delta s$  in the vertical direction as a function of time. (C) Relative intensity change  $I/I_0$  as a function of time. (D) Full width at half maximum (FWHM) for the (002) Bragg spot as a function of time [71].

The most pronounced dynamical features of the diffraction patterns after the ultrafast temperature jump are the collective downward movement of the Bragg spots

and subsequent recovery at longer times (figure 6.2(B)); the unusual intensity changes (figure 6.2(C)); and width changes (figure 6.2(D)), which are almost mirror images to the intensity changes, as a function of time.

### 6.1.1 Atomic motions in the chain

A downshift of Bragg spots in reciprocal space corresponds to an expansion of the orthorhombic R(001) subunit cell along  $c_0$  in real space. There is no measurable change in any of the in-plane directions, that is along  $a_0$  and  $b_0$ . This is in contrast to the observations made in the steady-state temperature dependence studies (see section 5.4), and indicates a nonthermal behavior of the LB films on the ultrafast timescale.

A typical time dependent peak shift of the Bragg spots in the vertical direction compared to their original position is depicted in figure 6.3(A) as the  $z$ -component of the momentum transfer  $s$  versus delay time. It is obtained for the bilayer film deposited at pH = 9 and  $\pi = 10$  mN/m at low incidence angle ( $\theta_i = 0.8^\circ$ ,  $\phi = 0^\circ$ ), as the static diffraction pattern shown in figure 5.4(A). As is readily seen, the five Bragg spots all move down and then come back with similar time dependencies. However, there is a relatively small difference between the spots with Miller indices  $l = 1$  (e.g.,  $(0\bar{2}1)$  and  $(021)$ ) and  $l = 2$  (e.g.,  $(0\bar{2}2)$ ,  $(002)$  and  $(022)$ ).

As we converted the peak shift into real space, the resulting change in lattice spacing  $\Delta c_0$ , which is the change of  $-\text{CH}_2\text{-CH}_2\text{-CH}_2\text{-}$  distances of chains, is plotted against time in figure 6.3(B). The plot shows an ultrafast rise of  $\Delta c_0$ , followed by a slower decay. This behavior represents an initial expansion of the sub-cell in the bilayer after impulsive laser-pulse heating of the substrate followed by a subsequent compression due to the heat dissipation. The absolute change  $\Delta c_0$  is 0.10 and 0.05 Å in the diffraction orders with  $l = 1$  and  $l = 2$ , respectively. For  $l = 1$ , the change is 4% of the static value  $c_0 = 2.54$  Å. For the same  $l$ , the expansion of the bilayer takes place with a time constant of 25 ps, whereas the subsequent compression occurs with 55 ps. For the other spots the behavior is similar, and for all peaks, the much longer time behavior is well described with a restructuring time constant of 1.15 ns.

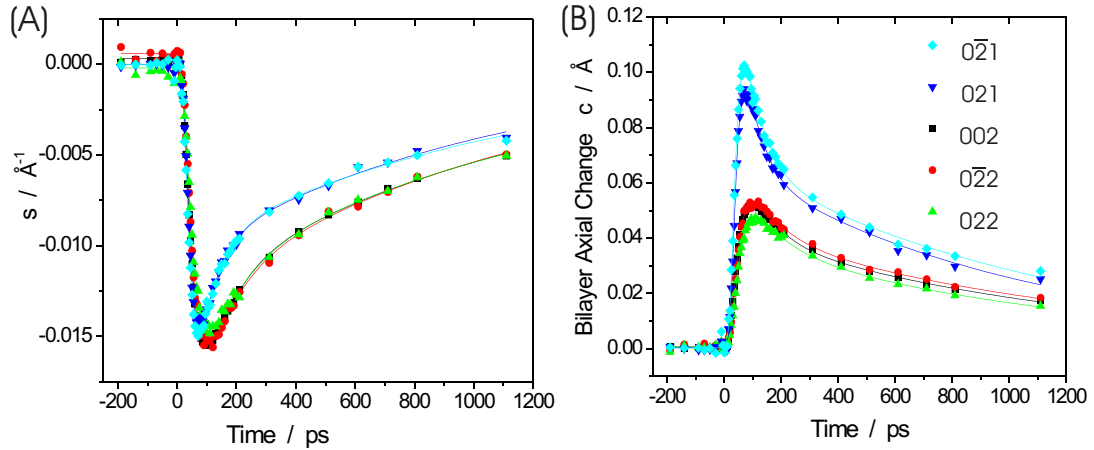


Figure 6.3: Time dependence of the peak shift and the corresponding molecular axial length change, obtained for the bilayer film deposited at  $\text{pH} = 9$  and  $\pi = 10 \text{ mN/m}$  at low incidence angle ( $\theta_i = 0.8^\circ$ ,  $\phi = 0^\circ$ ). (A) The  $z$ -component change  $\Delta s$  of the momentum transfer as a function of time for the different Bragg spots indexed in the diffraction patterns. (B) The corresponding molecular axial length change  $\Delta c_0$  of the  $\text{CH}_2$  sub-cell as a function of time [28].

It seemed obvious to propose that the fact that the Bragg spots of different order  $l = 1$  and  $l = 2$  move down for almost same amount in  $s$  is due to an electric field effect. However, close inspection makes this explanation not likely. First of all, the fatty acid LB films are insulators. The 800nm ultrafast laser did not excite the molecules directly, nor did the influence used in our experiments large enough to break the dielectrics. It seems unlikely that there are free carriers present at the film surfaces. Secondly, the diffraction patterns are generated from the electrons transmitted through the LB films. The simple estimation, assuming the peak shift is due to the electric field from a dipole layer, yields a field strength for  $10^7 \text{ V/cm}$  and  $5 \times 10^{12}$  electrons at the film surfaces, which seems too large to be possible. Finally, we note that even for the substrate, the rocking curve provides the correct lattice spacing only from higher order diffraction spots (large  $\theta_i$ 's), which have small widths, and therefore care has to be taken at small  $\theta_i$ 's when considering changes in  $s$  and the associated larger uncertainty (see section 4.1). We also observed that the downshift of the Si Bragg spots is different from the LB films' (see below), which indicates that

the shift is not due to an electric field effect.

It is interesting to compare the structural dynamics, e.g., the Bragg spots' position changes, in the fatty acid films with that in the silicon substrate. As shown in figure 6.4(A), the diffraction pattern for the bilayer film deposited at  $\text{pH} = 9$  and  $\pi = 10$  mN/m, obtained at  $\theta_i = 2.3^\circ$  and  $\phi = 1^\circ$  off the  $\text{Si}[11\bar{2}]$  zone axis, was followed as a function of time. At this higher  $\theta_i$  angle, Bragg spots from the bilayer ((002) Bragg spot) as well as the silicon substrate can be observed, making the comparison straightforward. In the diffraction pattern, the Bragg spots of silicon are indexed in terms of the (111) surface in the zone axis of  $[11\bar{2}]$ . At this angle  $\text{Si}(00)$  can also be indexed in terms of the bulk structure as  $\text{Si}(444)$ , as from the rocking curve (figure 5.5).

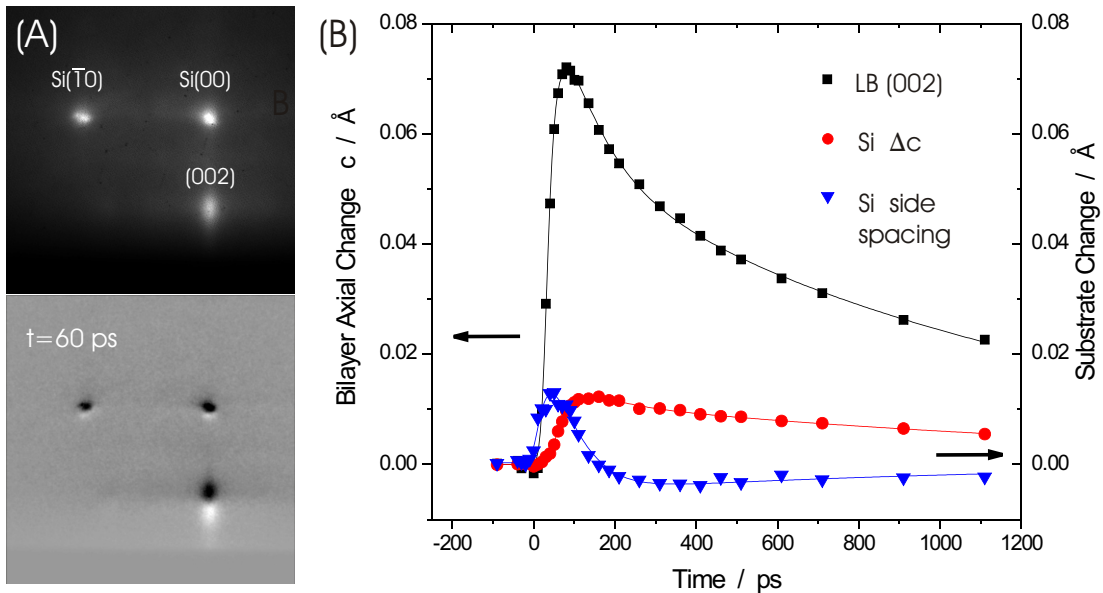


Figure 6.4: Dynamics of fatty acid bilayer compared to that of the substrate  $\text{Si}(111)$  surface. (A) The static diffraction pattern and the diffraction difference at delay time  $t = 60$  ps, obtained at  $\theta_i = 2.3^\circ$  and  $\phi = 1^\circ$ . The  $s$ -range is from  $-0.85$  to  $+0.35 \text{\AA}^{-1}$  in horizontal and from  $+0.45$  to  $+1.65 \text{\AA}^{-1}$  in vertical direction. (B) The change of the  $\text{CH}_2$  sub-cell in the bilayer and of the substrate. The LB bilayer  $\Delta c_0$  is obtained from momentum transfer  $s$ -values of the Bragg spots (002); the Si  $\Delta c$  from  $s$  of the Bragg spots  $\text{Si}(00)$ ; and Si side spacing from  $s$  of the Bragg spots  $\text{Si}(\bar{1}0)$  and  $\text{Si}(00)$  [28].

The Bragg spots were analyzed in a similar way as for the lower  $\theta_i$  angles. The

change of the lattice constant in the bilayer and silicon as a function of time are shown in figure 6.4(B). As expected, the LB(002) peak shows the same behavior as in figure 6.3(B). However the silicon lattice undergoes a very different dynamics. While the spot LB(002) of the bilayer changes only in the vertical direction, the spots of the silicon change also sideways, indicating a displacement in the planes parallel to the interface. The absolute change in the lattice spacing is much smaller in silicon than in the bilayer, 0.013 Å (from the (002) spot) vs. 0.072 Å. The temporal behavior indicates the temperature rise, similar to the behavior observed before (see chapter 4); following the rise, the silicon restructures on the nanosecond time scale. The presence of the bilayer on the surface enhances the vibrational couplings (faster rise) and suppresses the large amplitude surface displacement of silicon without the bilayer.

The effect of multilayers on the expansion is shown in figure 6.5 for each Bragg spot in the diffraction pattern at  $\phi = 90^\circ$  for the 2-, 4- and 8-layer samples. The data for  $\phi = 0^\circ$  are not shown, but the dynamical behavior is similar. The amplitude increases with overall chain length, which is not expected for the dynamics in simple equilibrium. However, as will be discussed in section 6.3, it is consistent with dynamics in the nonequilibrium regime. We must also take into account that LB films show an increased density of “defects” and holes upon increasing thickness (mainly in the outer layers) [88]. As mentioned in chapter 5, in static LB film structures, the decreased influence of substrate has the consequence of in-plane expansion of the subunit cell along  $a_0$  and  $b_0$ , the onset of chain inclination, and the loss of crystalline order. The decreased density in LB films upon going from single to multiple layers results in a less confined environment, with the expansion along the carbon chains becoming freer. Spatial confinement indeed decreases the mobility of say a chromophore in the membrane of vesicles [137] and even water in reverse micelles [138].

As a result of energy transfer from the heated silicon substrate into the adsorbate, the observed ultrafast increase of the axial change  $\Delta c_0$  is consistent with expansion of the fatty acids solely along their aliphatic chains (20–60 ps). This efficient and directional energy transfer within the fatty acid assembly is facilitated by the unique substrate heating. As discussed in chapter 4, the initial ultrafast heating induces

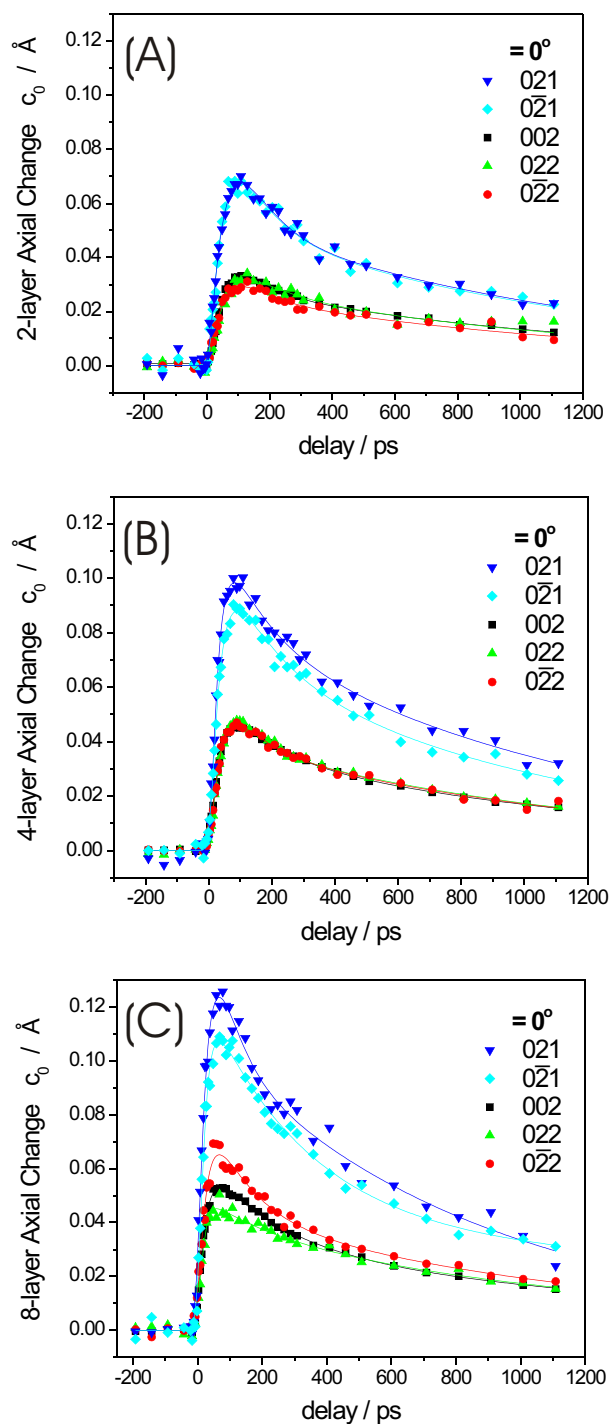


Figure 6.5: The molecular axial length change  $\Delta c_0$  of the  $\text{CH}_2$  subunit cell as a function of time showing the behavior for the different diffraction spots for (A) 2-, (B) 4- and (C) 8-layer samples. The incident azimuthal angle  $\phi = 90^\circ$ . The Bragg spots are those indexed in the static diffraction patterns shown in figure 5.10, for films deposited at  $\text{pH} = 6.4$  and  $\pi = 29 \text{ mN/m}$  [71].

a potential-driven lattice change in the material and this results in a surface displacement which for the case discussed here acts as a directional force. It should be mentioned that the surface heating area by the laser is much larger than the absorption depth in the substrate, and this gradient of stress (temperature) facilitates the  $c$ -direction change. Moreover, the transfer within the chain is much more efficient than across the chains because of covalent bonding, as opposed to the relatively weak interactions across the chains. The elongation is followed by nonequilibrium contraction and restructuring due to energy redistribution and diffusion at longer times (60–230 ps and 1.2–1.5 ns). This behavior is indicative of two regimes of structural dynamics, that of nonequilibrium coherent motion of atoms at short time, and the evolution toward equilibrium at longer times.

The inclined chains provide an opportunity to test the nature of the expansion in directions other than perpendicular. Their inclined diffraction patterns are shown in figure 6.6 for the 8-layer sample deposited at  $\pi = 29$  mN/m and  $\text{pH} \simeq 7$ . After the temperature jump, the smeared diffraction lines move down along the direction perpendicular to their longitudinal axis on the CCD, as shown in figure 6.6(A) for various diffraction difference images. The amplitude and time behavior of the change in the lattice spacing is comparable to that of a nontilted pattern as shown in figure 6.6(B), which is calculated from the  $s$  change for the  $(hk2)$  line along the inclined direction. The dynamics of the nontilted pattern is shown for the  $(002)$  Bragg spot of the 8-layer calcium arachidate sample deposited at  $\text{pH} = 6.4$  and  $\pi = 29$  mN/m.

This observation of tilted line movement is in total agreement with the heating pulse initiating an expansion and contraction solely along the fatty acid carbon chains. The fact that the lines move along the inclined direction rather than the direction perpendicular to the shadow edge also excludes other effects which could force the Bragg spots to move in the diffraction patterns — for example charging effects or direct beam movements.

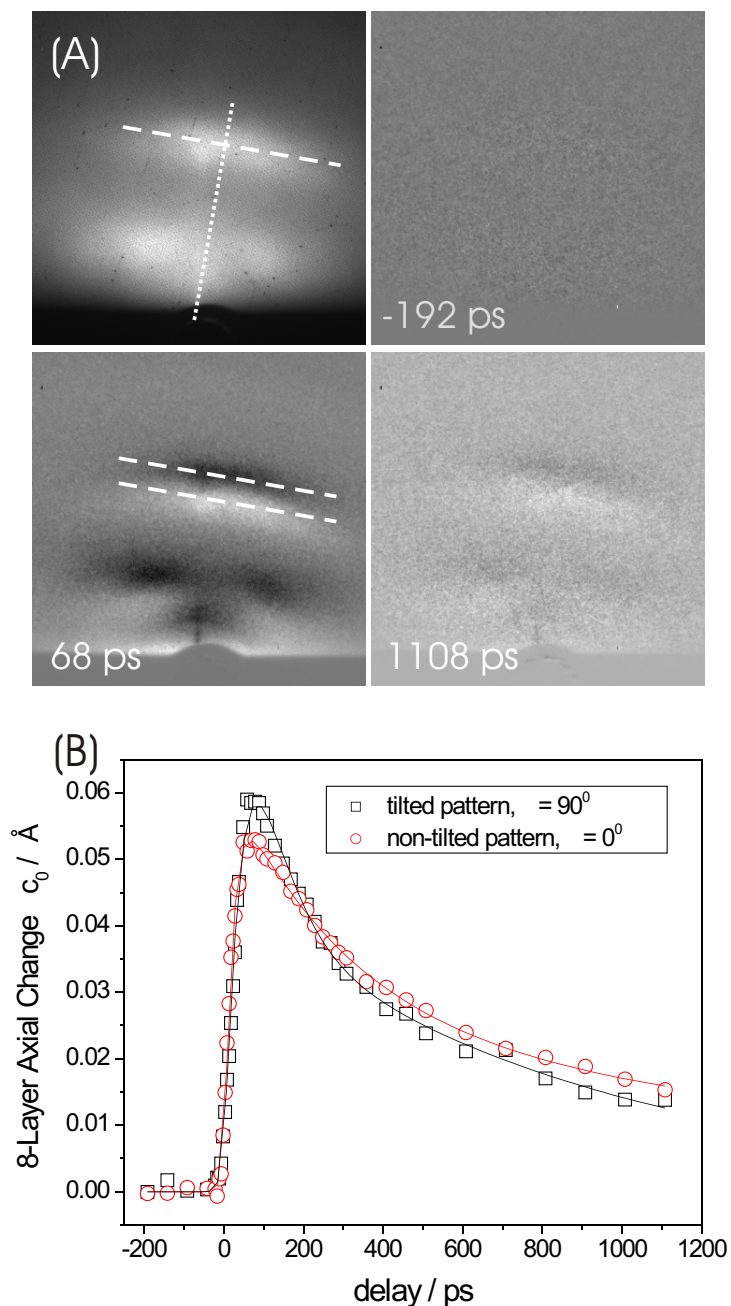


Figure 6.6: Diffraction difference patterns at  $\phi = 0^\circ$  and the axial change  $\Delta c_0$  of the inclined 8-layer sample deposited at  $\text{pH} \simeq 7$  and  $\pi = 29 \text{ mN/m}$ . (A) The static diffraction pattern before laser irradiation shows an inclination of  $\sim 10^\circ$ . The diffraction difference images show the movement of the smeared lines along the direction of the aliphatic carbon chains. (B) The axial change of  $c_0$  for the inclined fatty acids LB films at  $T = 300 \text{ K}$  in comparison with the changes for the noninclined 8-layer sample deposited at  $\text{pH} = 6.4$  and  $\pi = 29 \text{ mN/m}$  at  $\phi = 90^\circ$  (see figure 5.10) [71].

### 6.1.2 Transient structural ordering

In figure 6.7, the relative integrated intensity changes  $I/I_0$  of the (002) Bragg spots as a function of time for the 2-, 4- and 8-layer samples are depicted. Even though we show only transient intensity behavior of the (002) Bragg spot, the intensities of the other Bragg spots exhibit similar trends. All samples show comparable transient intensity change.

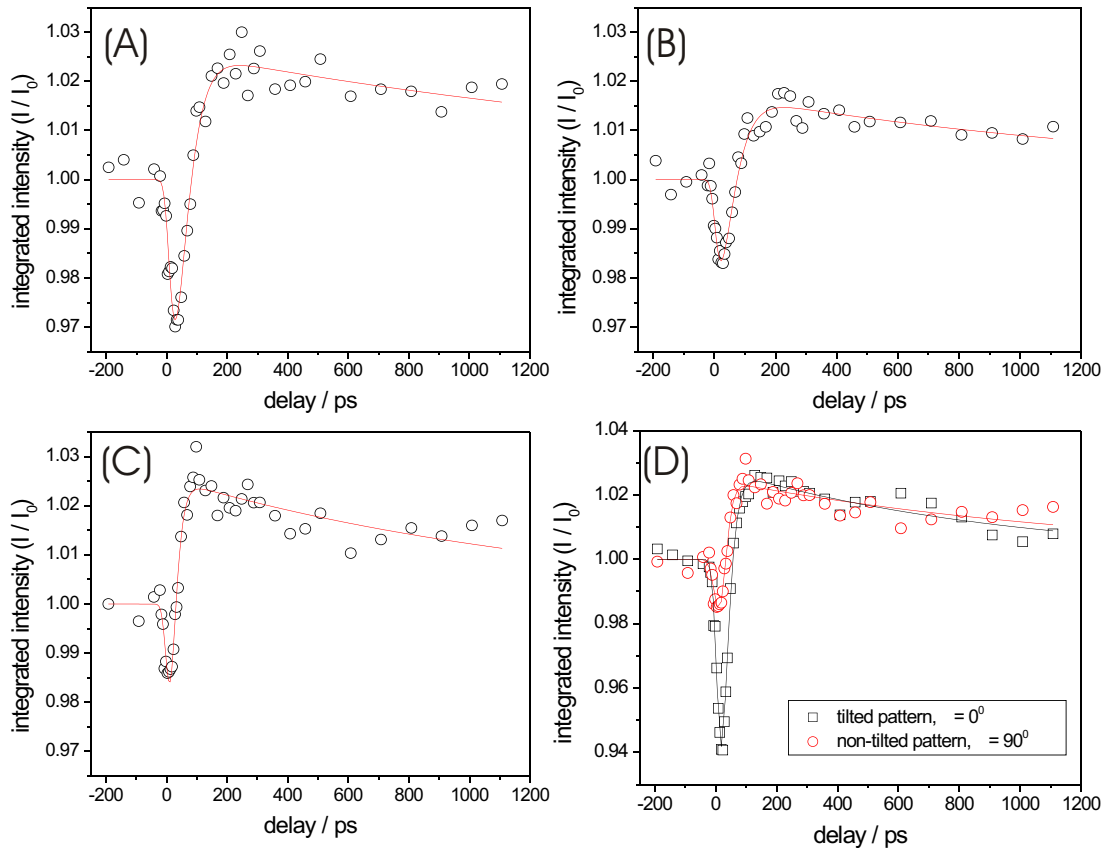


Figure 6.7: Relative intensity change  $I/I_0$  as a function of time for (A) 2-, (B) 4- and (C) 8-layer samples, deposited at  $\text{pH} = 6.4$  and  $\pi = 29$  mN/m, at incident angle  $\phi = 90^\circ$ . (D) The relative intensity change  $I/I_0$  for the inclined fatty acids LB films, deposited at  $\text{pH} \simeq 7$  and  $\pi = 29$  mN/m, at incident angle  $\phi = 0^\circ$ , in comparison with the changes for the noninclined 8-layer sample [71].

For “conventional” heating, the intensity is expected to initially drop and subsequently recover back to the initial value, similar to the trend observed for the Bragg spot center position,  $\Delta c_0$ . This intensity drop follows the influence of the incoherent

motions of the atoms, which are described by the Debye-Waller factors, and structural changes due to phase transitions (see figure 5.7 and 5.8 for the static temperature behavior). For the fatty acids the transient behavior is much different from that observed at steady-state. We observe only a very short lived intensity drop on the ultrafast timescale, on the order of tens of ps. This initial drop is consistent with a disorder-induced heating, as it represents a decrease in intensity. However, after this initial decrease, the intensity recovers also fast and even gains more intensity from that of the initial value. The fact that the transient intensity is higher than the initial one indicates the formation of a transient structure with a higher degree of order. We term this behavior transient structural ordering.

Interestingly, the intensity change mirrors the line width behavior as shown, e.g., in figure 6.2(C) and (D). The line width of the Bragg spots reflects the order of the crystalline structure, and is narrower for a more ordered state. This trend is again consistent with transient structural ordering, which can be understood using the following picture, schematically depicted in figure 6.8.

Initially, the dynamics follow the expected loss of order due to rapid thermal motions similar to that observed in the early stage of the static temperature dependence; note that the lower part of figure 6.8 is similar to that shown in figure 5.9. A static temperature rise results in an expansion of the fatty acid lattice along  $a_0$  and  $b_0$  (see figure 5.8(B)), whereas upon laser pulse heating the energy is mainly transferred along the aliphatic chains, which results in a large increase in  $c_0$ . By overcoming some energy barrier and through alignment of the aliphatic chains and other motions (rotation, bending, etc.), and possibly through transient annealing of the film, the fatty acid molecules find an energetically more favorable structure in the film. As a result, the formerly imperfect structure transforms into a more ordered system. Because of energy dissipation on the nanosecond time scale, the film eventually restructures to its initial state. The Bragg spot center position, intensity and the line width recover toward their equilibrium values with ns recovery component, and on the ms scale (our laser repetition time) the signal is certainly back to the initial values.

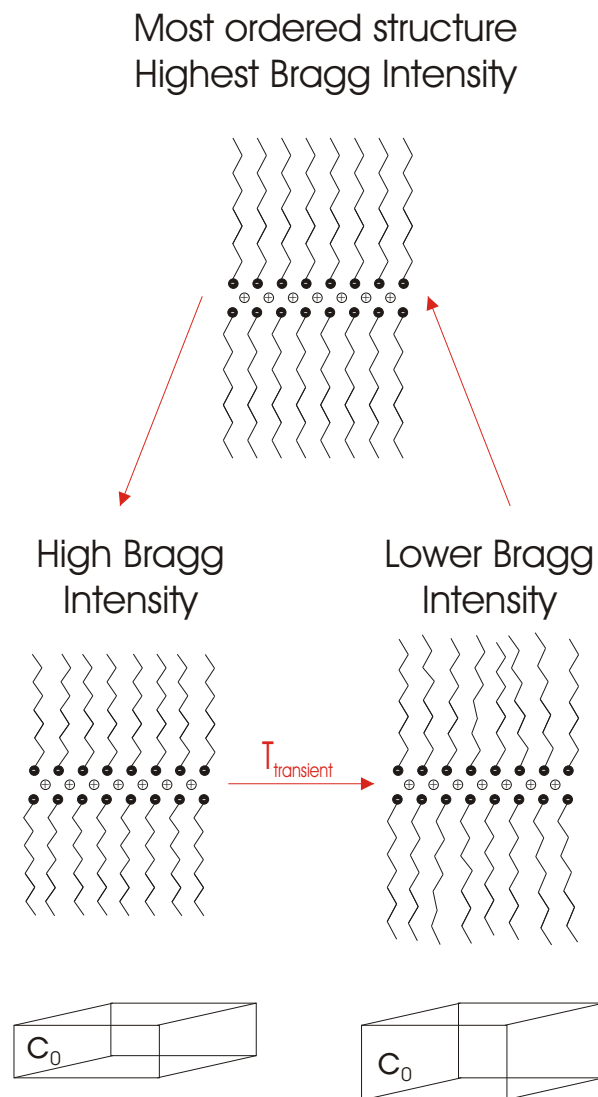


Figure 6.8: Schematic view of the transient structural ordering [71].

### 6.1.3 Dynamics at different static temperature

The comparison of transient and static structural changes was directly made by studying the transient behavior at different substrate temperatures. In figure 6.9 the transient axial change  $\Delta c_0$  and the integrated intensity change for different static temperatures are plotted for the bilayer deposited at  $\text{pH} \simeq 7$  and  $\pi = 29 \text{ mN/m}$ . The dynamics are shown for the (002) Bragg spot observed at  $\phi = 0^\circ$  and  $T = 100, 295$  and  $333 \text{ K}$ . Indeed, the temporal behavior for the expansion and restructuring is similar for the three different temperatures, but the initial maximum amplitudes of expansion are different, increasing with increasing temperature. This trend is again consistent with the picture discussed above, namely that elevated temperatures facilitate a more pronounced expansion.

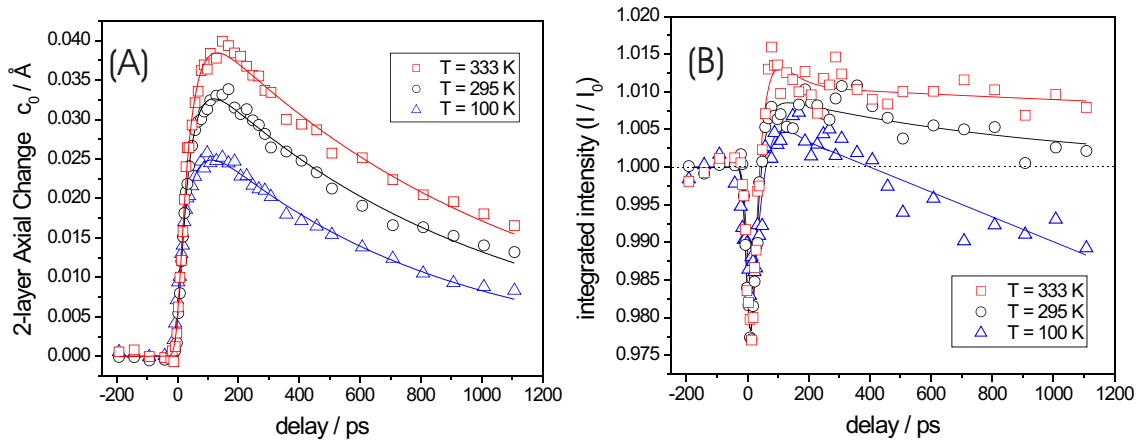


Figure 6.9: Dependence of the transient dynamics on initial substrate static temperature:  $T = 100, 295$  and  $333 \text{ K}$  are shown. (A) The transient molecular axial change  $\Delta c_0$  of the  $\text{CH}_2$  subunit cell as a function of time for  $\phi = 0^\circ$ . (B) The corresponding relative intensity change  $I/I_0$  as a function of time [71].

The results shown in figure 6.9(B) further support the picture, as the intensity changes show more pronounced transient structural ordering extending over a longer time span at elevated temperatures. For  $T = 295$  and  $333 \text{ K}$  the intensity recovers back to its initial value on a nanosecond timescale or larger, whereas for  $T = 100 \text{ K}$  the transient structural ordering persists only for  $\sim 350 \text{ ps}$  after laser pulse heating, after which the intensity drops below the initial value again, and therefore resembles

the conventional Debye-Waller behavior. This strengthens the view that expansion along  $c_0$  and preparation of the ordered state are not two unrelated processes, but are facets of the same underlying molecular motions.

In summary, all investigated fatty acid adsorbates show expansion and restructuring along the fatty acid carbon chains. From the transient and static diffraction behavior with time and temperature, it is shown that transient structural ordering on the ultrafast timescale, initiated by laser pulse heating, is a common feature of these layered structures. Such transient structures, their anisotropy of expansion, and inhomogeneity would remain unrevealed without the resolutions of UEC.

## 6.2 Phospholipid structural dynamics

For phospholipids, the diffraction patterns contain mainly the  $(hk2)$  line, as discussed in section 5.6. Figure 6.10 displays the static diffraction patterns and the diffraction difference patterns at various delay times after the fs laser-initiated temperature jump in the underlying substrate, for DMPA monolayer and bilayer film respectively. The patterns show no features at negative times, and at positive times, mainly a change in the  $(hk2)$  line position, becoming dark at the higher  $s$  value and bright at the lower  $s$  value, indicating a downward movement of the diffraction line. This translates to an increase of the  $-\text{CH}_2-\text{CH}_2-\text{CH}_2-$  distances along the aliphatic chains.

As before, we were able to fit the diffraction line with a Voigt function in the vertical  $s$  direction, providing us with accurate center position and intensity changes with time, as shown in figure 6.11(A) and (B) for the monolayer and bilayer, respectively. The error range for the width did not permit accurate values.

The dynamics of the center position change is similar for both samples, monolayer and bilayer, and are similar to the behavior observed for fatty acids. An increase in  $c_0$  within  $\sim 50$  ps was observed with a recovery on the  $\sim 500$  ps and longer time scale. This similarity in trend is not surprising since we are probing the structural dynamics of the aliphatic chains, and in this respect DMPA resembles the fatty acid samples. It is known that for phospholipids there exist different phases (“gel” and “liquid”)

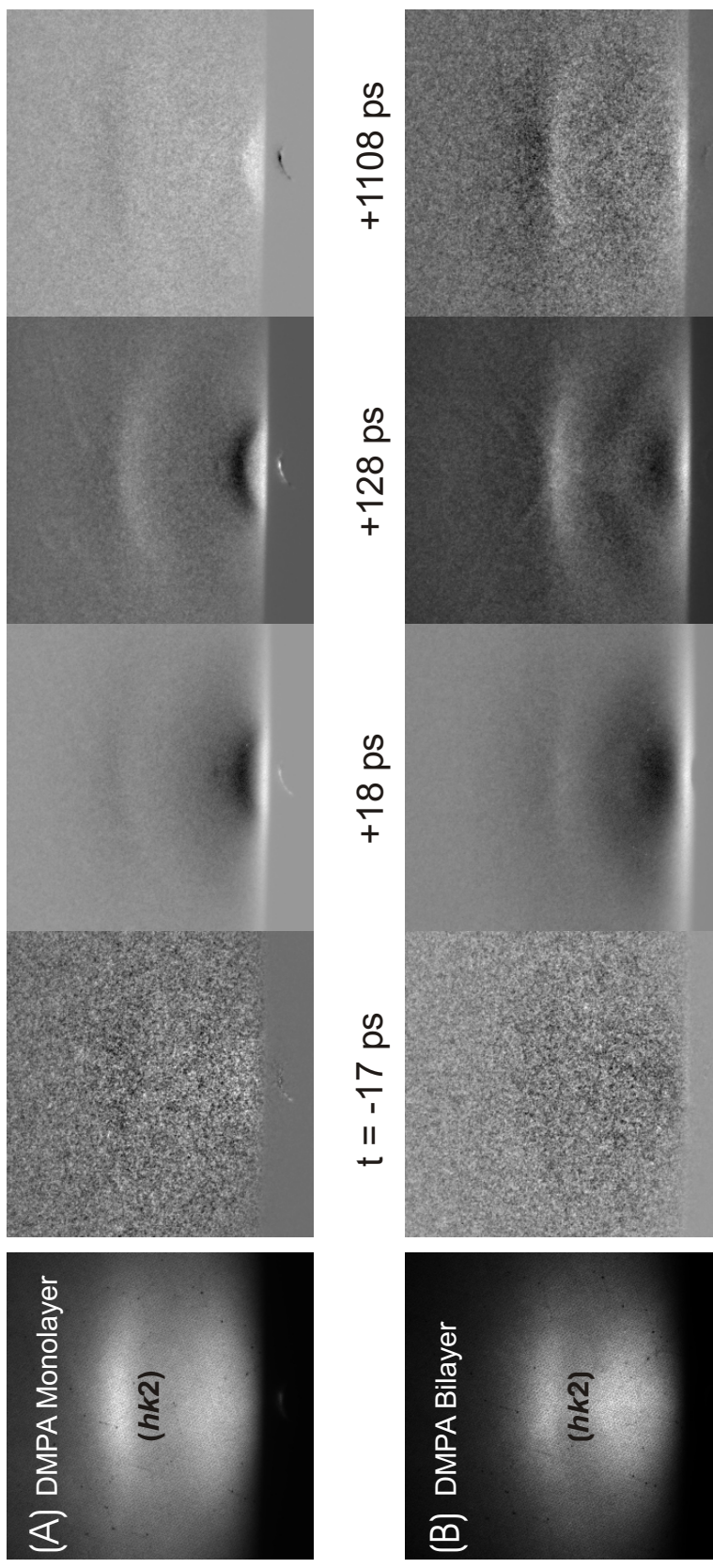


Figure 6.10: Static diffraction and diffraction difference patterns of DMPA monolayer (A) and bilayer (B). The diffraction difference patterns are shown with the time delays indicated [29].

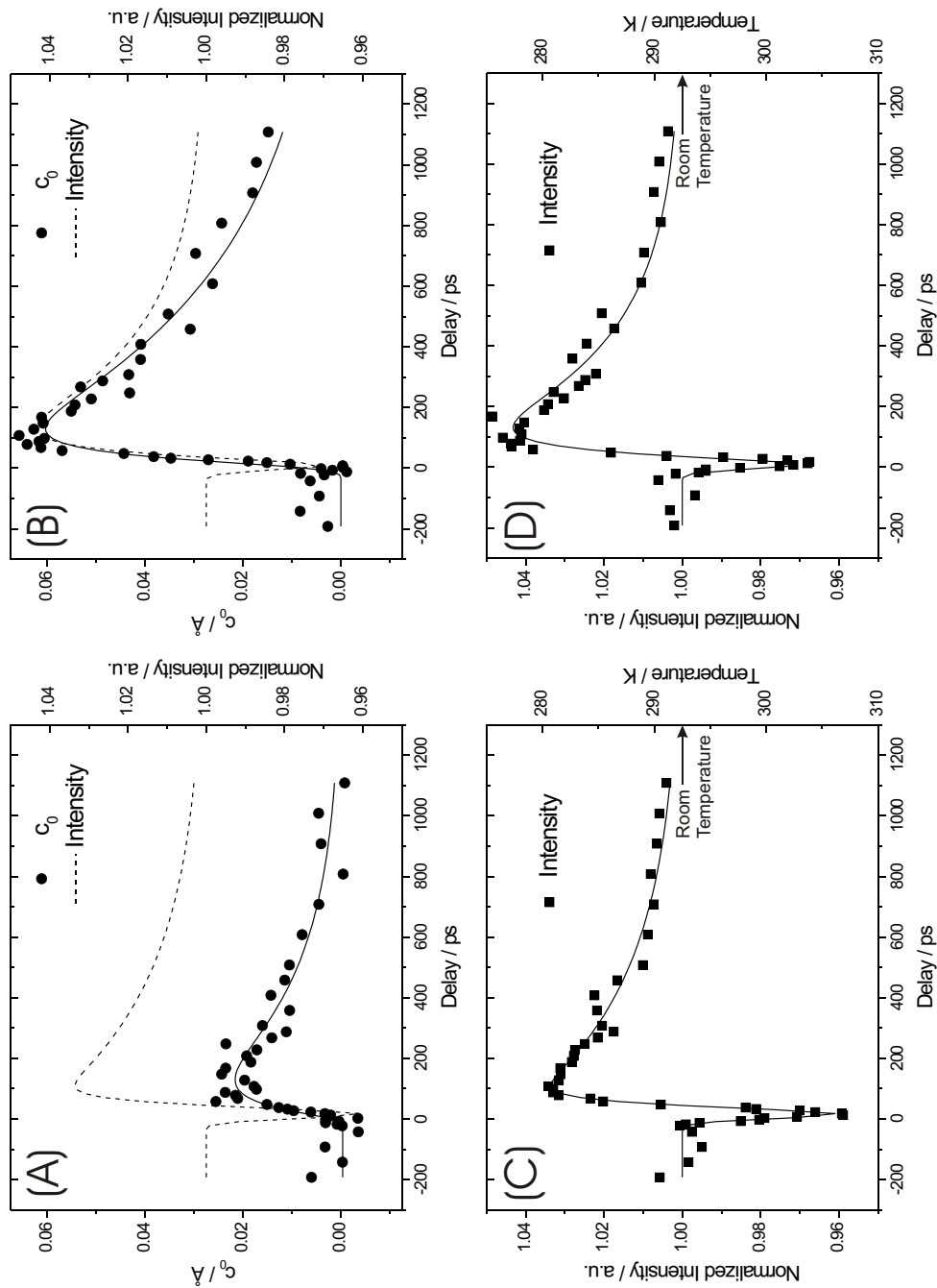


Figure 6.11: The axial change  $\Delta c_0$  and the normalized integrated intensity of the  $(hk2)$  diffraction line as a function of time, (A) and (C) for the monolayer and (B) and (D) for the bilayer of the phospholipid [29, 71].

and it is interesting that neutron scattering studies give a lifetime of 17 ps for the acoustic phonon excitation in the gel phase [139].

As shown in figure 6.11(A) and (B), the amplitude of the expansion for the bilayer is nearly three times that of the monolayer. A similar trend was observed for samples of 2-, 4- and 8 layers of fatty acids (see figure 6.5), but with smaller differences. This larger change of amplitude may be because the first layer exhibits different forces than the subsequent layers as it is directly bound to the silicon substrate. If the interaction forces are stronger than in the subsequent layers, we expect a tighter binding to the substrate and an increased order in the first layer, resulting in less mobility for expansion. It is interesting that for bilayers of fatty acids and phospholipids the expansion of the former is nearly half that of the latter, suggesting a bigger flexibility for expansion in phospholipids, which is again consistent with the above mentioned picture. The monolayer was studied on a hydrophilic surface, unlike the bilayer, and this is entirely in line with the proposed strong interaction with the substrate.

The intensity changes with time are also shown in figure 6.11. As in the case of the fatty acids, initially an intensity drop is recorded, consistent with the disorder being induced within 15 ps by the heating pulse. After this change the intensity increases to a value above the static one within  $\sim 130$  ps, before final recovery toward the initial configuration at  $\sim 400$  ps and longer times. The transient state of increased intensity is indicative of transient structural ordering, as discussed above for fatty acid structures. The temperature scale given in figure 6.11 is from the static intensity change as a function of equilibrium temperature (figure 5.8(A)) for a fatty acid bilayer. In the simplest model of harmonic chains, a change of  $0.02 \text{ \AA}$  corresponds to a temperature increase of approximately 30 K, in the nonequilibrium regime.

In conclusion, the phospholipid monolayer and bilayer samples of DMPA show a transient behavior similar to that of fatty acids, both being adsorbates on a substrate. We observed elongation along the aliphatic chains following the ultrafast temperature jump, accompanied by transient structural ordering. The similarity is not surprising because structural changes involve the  $-\text{CH}_2-\text{CH}_2-\text{CH}_2-$  subunit cell. However, the amplitude of expansion, the influence of substrate forces, and the mobility of the

structure are found to have differences.

### 6.3 Structural dynamics picture

In chapter 4, it was demonstrated that ultrafast dynamics and heating of materials with a band gap are directly evident in the change with time of Bragg diffraction spot positions, their intensities and widths. The mechanism for the generation of the temperature jump is basic: the femtosecond infrared pulse excites carriers which then by electron-phonon coupling heat up the lattice and the material sustains the lattice temperature until diffusion of heat takes place on a much larger time scale. Because of the change in potential by carrier excitation and the fact that the excited region with the laser pulse is much larger than the absorption length, the gradient change is perpendicular to the surface of the material. This gradient results in a large expansion of surface atoms which is a force on the ultrashort time scale [140].

This T-jump of the material (substrate) — or the force of surface atoms — is exploited to heat up the adsorbate in a direct contact with either a hydrophobic or hydrophilic substrate; the femtosecond infrared pulse has no resonance for absorption to the adsorbate. Such studies made here for monolayers, bilayers and multilayers of fatty acids and phospholipids provide an opportunity to study structural dynamics at these interfaces on the nanometer scale, and to examine changes due to the transition from two-dimensional to three-dimensional. To achieve crystallinity, we use the methodology of Langmuir-Blodgett film, providing control over pH, thickness and pressure.

Four types of UEC measurements make possible the study of structural dynamics: the change of position with time of Bragg spots; the temporal evolution of the diffraction intensity change; the increase/decrease in diffraction width; and the change of diffraction with angle of incidence  $\theta_i$  (rocking curve) and azimuthal angle  $\phi$  for the position of the electron pulse relative to the zone axis of the substrate (see figure 5.3). As shown above, these measurements can be made with the sensitivity achieved in UEC. Prior to these measurements, we establish the static (time-averaged) structures

of the adsorbates (fatty acids and phospholipids) by determining the orientation of the chains relative to surface plane, and the  $-\text{CH}_2-\text{CH}_2-\text{CH}_2-$  chain distances which are the subunit cell dimensions  $a_0$ ,  $b_0$  and  $c_0$ .

The transient anisotropic change in  $c_0$  of fatty acid and phospholipid layers is vastly different from that observed in the steady-state equilibrium state. At equilibrium, we observe changes in  $a_0$ ,  $b_0$  (not  $c_0$ ) and the diffraction intensity only decreases to reflect thermal, incoherent motions (Debye-Waller effect) and phase transitions. On the ultrafast timescale, the expansion is along  $c_0$ , unlike the thermal case, and the amplitude of change is far larger than predicted by incoherent thermal expansion. The expansion amplitude depends on layer thickness and the nature of bonding to the substrate (hydrophilic vs. hydrophobic). The intensity and width changes are also very different from those observed by equilibrium heating, showing a transient structural ordering in tens of ps.

Following the initial ultrafast heating, the structure first expands (atomic displacements) along the  $c$ -direction (compare figures 5.9 and 6.8). These motions with the acquired energy in the layers lead into transient structural ordering through “annealing” and/or chain motions, as evident from increased diffraction intensity and narrowing of diffraction width beyond the initial values. On the nanosecond and longer time scale, the structure reaches quasi-equilibrium or equilibrium (incoherent movement of atoms) and by dissipation of heat (diffusion) the structure acquires the original configuration, certainly on the millisecond time scale between pulses. This behavior is in contrast with that observed at steady state.

The net change in displacement is determined by the impulsive force (“temperature”) of the substrate (including coupling), and the maximum value of the extension depends on elasticity and heat capacity. If heating occurs for an equilibrated system, the change in the value of  $c_0$  with temperature  $\Delta c_0$  (by anharmonicity) should be independent of the number of  $-\text{CH}_2-\text{CH}_2-\text{CH}_2-$  subunits in the chain, and  $\Delta c_0/c_0$  becomes simply  $\alpha$  (the thermal expansion coefficient), which is typically very small  $\Delta c_0/c_0 \simeq 10^{-5}T^{-1}$  [141]; for a 10-degree rise, this expansion would be on the order of  $10^{-4}$  Å, while the observed transient change is as large as 0.01 Å. For nonequilibrium

dynamics in the chains, this large amplitude is understood even for harmonic chains.

The impulsive force at short times transmits a large change in the value of  $\Delta c_0$  as the disturbance (wave-type) accumulates to give the net effect that is dependent on the number of C atoms [142]. In other words, as the disturbance passes through the different bonds, the diffraction amplitude builds up and exhibits a delay, ultimately giving a rise and large total amplitude for the change. This picture also explains the dependence on the total length of the chains, the increase in initial maximum amplitude as the temperature of the substrate increases, and the effect of substrate strong (hydrophilic) vs. weak (hydrophobic) binding. Quantification of the total change must take into account the nature of the substrate force and variation in the density of the LB films upon going from single to multiple layers. It is known that “defects” or “holes” can be formed when multiple layers are deposited [88], and that disorder is expected as the influence of the substrate subsides.

The fact that the initial change in intensity (and elongation) occurs on the 10 ps time scale and that the distance traveled is approximately 20 Å (for a monolayer) the speed of propagation should be sub-kilometers per second, which is close to the propagation of sound waves. Because the substrate is heated through optical and acoustic phonons (see chapter 4), the rise is convoluted with the process of phonon generation which is on the time scale of 10 ps; we note that the resolution imposed by the geometry of electron and light propagation on the surface is  $\sim 1$ –2 ps. Accordingly, the speed could be of higher value reaching the actual speed of sound in the layers. Future experiments will further resolve this region to elucidate the maximum extension possible and the expected coherent features. The coherent coupling among bonds in the underdamped regime of harmonic motions is vastly different from the diffusive behavior in the overdamped regime.

The force and vibrational frequencies of  $-\text{CH}_2-\text{CH}_2-\text{CH}_2-$  motions in the diffusive (overdamped) regime have to be unrealistically large [142]. In the underdamped regime, although the force is significant to cause the large change in  $\Delta c_0$ , and coherent propagation is within the chain, the change in the value of  $\Delta c_0$  relative to that of  $c_0$  is relatively small to preserve the robustness of the Bragg spots throughout the

temporal change. It is important to point out that for large complex systems the diffraction has features of both “crystalline” and “diffusive” scattering. The latter gives structural information on the collective motions, which can be examined through cross-terms of the Debye-Waller factors [143]. In this regard, the ring(s) apparent at  $s \simeq 0.3 \text{ \AA}^{-1}$  in the diffraction difference patterns in figure 6.10 should be analyzed for such correlations in the phospholipid, and in future work we shall consider this analysis.

Besides the analytical theoretical work discussed above, in collaboration with Professor T. Shoji and colleagues in Japan, we have studied MD simulations of a prototype system. The model used is that of a silicon substrate with the adsorbates made of  $\text{C}_{20}\text{H}_{42}$  chains, covering a total combined length of  $95 \text{ \AA}$ . The potentials for the chains, substrate and the interaction at the interface were from *ab initio* calculations. The time step was 0.5 fs and the total number of steps was 200,000. The heat pulse was modeled based on the kinetic energy of the substrate atoms. The radial distribution function and the actual vibration motions of the atoms were obtained at different times, and we considered both the self-assembly and the confined geometry of the chains. These calculations provided the structural cell dimensions observed experimentally, and elucidated the coherent motion in the chain bonds and their time scales. Preliminary results show the increase in  $-\text{CH}_2-\text{CH}_2-\text{CH}_2-$  distance near the silicon surface by  $0.08 \text{ \AA}$  in about 5 ps.

# Chapter 7

## Conclusion

The advance of experimental techniques contribute significantly to the research of physics. In the study of ultrafast dynamics, laser spectroscopy has pushed the time resolution to femtosecond and attosecond. By using the femtosecond pulses as a spectroscopic probe, with light wavelengths ranging from the ultraviolet to the infrared and terahertz, or other emissions such as electrons and ions, a great number of systems and processes in biology, chemistry and physics have been studied. But when the process under study involves structural change, only indirect structural information can be obtained from ultrafast spectroscopy.

Combining the ultrafast time resolution in picosecond to femtosecond and the atomic spacial resolution in sub-ångström, ultrafast diffraction techniques are developed to study the structural dynamics directly. Comparing to X-rays, electrons have larger scattering amplitude, penetrate less and better match the optical penetration depth in most samples, and are less damaging to samples for the same diffraction signals (scattering events), especially for biological specimens. The technology for generating, deflecting and focusing the electrons is well developed and allows for diffraction and imaging experiments of laboratory scale.

Using the fs laser pulse as pump pulse and the ultrashort electron pulse as probe pulse, ultrafast electron crystallography (UEC) is developed as a pump-probe experiment, with the ultrafast time resolution in ps and the atomic spacial resolution in pm, to elucidate the structural dynamics in solids, surfaces and macromolecular systems.

The UEC apparatus consists a homemade ultrahigh vacuum (UHV) chamber sys-

tem and a commercial femtosecond laser system with optical interfaces. The fs laser system provides both the laser pulses for the generation of ultrashort electron pulses and those initiating the reactions to be studied. UHV is required for the surface experiments, and the chamber system includes the scattering chamber, the sample preparation chamber and the load lock chamber. The scattering chamber connects to the electron gun system and the imaging system, where the electron pulses are generated, focused and recorded after they are diffracted by the samples. A mechanical system allows the sample to be transferred between the chambers under UHV, and manipulated for the diffraction experiments. A homemade gas handling system with a microcapillary array beam doser augments the UHV chamber system to deliver gas adsorbates to the surface in a controlled and quantitative way.

The principle of the UEC analysis is from the static electron crystallography, with emphasis on RHEED for surface studies. As a pump-probe experiment, accurate characterization and alignment of the fs laser pump pulse and the ultrashort electron probe pulse were carried out, and the time zero and time resolution were determined. The diffraction patterns at each time step are analyzed to obtain the structural changes, especially the changes in the total intensity of the diffraction peak, the diffraction peak position and the peak width in reciprocal space.

The UEC experiments for surface studies are first demonstrated on semiconductor surfaces, because their surfaces can be relatively easily prepared with different adsorbates, and their crystalline and physical properties are well studied. UEC studies on silicon(111) surfaces and GaAs(111) surfaces show coherent nonthermal motions of atoms following ultrafast laser irradiation. The amplitude of atomic motions, the temperature change and the time scales are determined. Experiments on surfaces with molecular adsorbates are also carried out, but the challenges of structural disorder and low density prevent more detailed analysis.

Langmuir-Blodgett technique has proven powerful in the preparation of two-dimensional crystalline films. It allows for a controlled layer-by-layer deposition of ordered molecular films, and many different kinds of molecules have been successfully made into LB films. However, the selective preparation of adsorbates with well-defined

structures by means of the LB technique is not a trivial task, even for the “simplest” of all LB films, fatty acids and fatty acid salts. The steady-state studies of static structure using UEC without time resolution reveal crystal structures of fatty acid bilayers and multilayers, and their thermal behaviors. The impacts of the substrate, layer thickness and preparation conditions on the film structure are elucidated. We also studied the monolayer and bilayer LB films of phospholipid, which have similar structures to fatty acid but are more complex and are more relevant to biological molecules.

UEC studies of the structural dynamics following a temperature jump induced by femtosecond laser are based on the static structure determination and are compared to the equilibrium temperature dependence. For all LB films (fatty acids and phospholipids) studied, with sub-Å resolution and monolayer sensitivity, it is observed that a coherent anisotropic expansion solely along the aliphatic chains happens at picosecond time scale, followed by nonequilibrium contraction and restructuring at longer times. This motion is indicative of a nonlinear behavior among the anharmonically coupled bonds on the ultrashort time scale and energy redistribution and diffusion on the longer time scale. The effects of different molecules, layer thickness and substrate on the dynamics are examined. Unlike monotonic disordering in the equilibrium heating, a transient structural ordering was revealed on the picosecond time scale. Interestingly, it is found that this transient ordering is more pronounced and lasts longer at higher static sample temperature.

The combined structures (unit cell and orientation) and dynamics (after femtosecond laser heating) on LB films not only provide insights into the nature of atomic motions and energy transfer — coherent versus diffusive — in fatty acids and phospholipids, but also demonstrate the possibility of using UEC and LB films to study complex macromolecules. It will be very interesting to study other molecular dynamics, for example the photo-isomerization of retinal [144].

UEC is a very versatile technique. Although so far most UEC studies were done with reflection electron diffraction, the UEC apparatus was designed also capable of transmission experiments. In transmission mode, the velocity mismatch between

the laser and electrons is much smaller, and more Bragg spots can be obtained. The challenge with UEC in transmission mode is that the nondestructive structural change induced by laser inside the crystal, where the transmission electron diffraction probes, might be very small. The preparation of thin samples for the transmission experiments can also be difficult.

UEC is developed to study the structural dynamics of various materials. For bulk materials, many physical phase transitions involve structural changes, such as melting, surface reconstruction and solid-solid phase transitions. Also by observing the atomic motions in solids and on surfaces, we could study other physical processes related to phonons. On the other hand, the surfaces provide a template to study ordered molecules, as we have done for fatty acids and phospholipids.

As a pump-probe experiment, UEC can be used to study any structural dynamics induced by fs laser pulses. Although so far most experiments are done with 800nm or 266nm laser, it is possible to excite the molecules in the crystal or on the surface directly by varying the wavelength. Comparing to the gas phase, the excitation energy needed is smaller, though the heating effect will need to be taken into account.

Better time and space resolution will always be the pursuit for future UEC experiments. It has been shown that by better matching the velocity mismatch between the pump laser and probe electron pulses, the time resolution of UEC is improved in reflection mode [32]. Although our experiments are ultimately limited by the electron pulses we have, the single electron experiments provide entirely new ways of thinking [9]. Additionally, with the aid of dynamical diffraction theory, the transient crystal structures can be further refined from the diffraction patterns.

Together with new developments of UED in gas phase for more complex molecules, and new ultrafast electron microscopy (UEM), UEC proved to be a very important experimental technique to study the ultrafast structural dynamics of materials.

# Bibliography

- [1] A. H. Zewail, in *Les Prix Nobel: The Nobel Prizes 1999*, edited by T. Frängsmyr (Almqvist and Wiksell, Stockholm, 2000), Chap. Femtochemistry: atomic-scale dynamics of the chemical bond using ultrafast lasers.
- [2] E. T. Nibbering, H. Fidder, and E. Pines, *Annu. Rev. Phys. Chem.* **56**, 337 (2005).
- [3] J. M. Cowley, *Diffraction Physics* (Elsevier, Amsterdam, 1995).
- [4] *Time-resolved Diffraction*, edited by J. R. Helliwell and P. M. Rentzepis (Oxford University Press, Oxford, 1997).
- [5] A. Rousse, C. Rischel, and J. C. Gauthier, *Rev. Mod. Phys.* **73**, 17 (2001).
- [6] R. Srinivasan, V. A. Lobastov, C.-Y. Ruan, and A. H. Zewail, *Helv. Chim. Acta* **86**, 1761 (2003).
- [7] W. E. King, G. H. Campbell, A. Frank, B. Reed, J. F. Schmerge, B. J. Siwick, B. C. Stuart, and P. M. Weber, *J. Appl. Phys.* **97**, 111101 (2005).
- [8] A. H. Zewail, *Annu. Rev. Phys. Chem.* **57**, 65 (2006).
- [9] V. A. Lobastov, R. Srinivasan, and A. H. Zewail, *Proc. Natl. Acad. Sci. USA* **102**, 7069 (2005).
- [10] J. C. Williamson, Ph.D. thesis, California Institute of Technology, 1997.
- [11] H. Ihee, Ph.D. thesis, California Institute of Technology, 2002.
- [12] R. Srinivasan, Ph.D. thesis, California Institute of Technology, 2005.

- [13] J. S. Feenstra, Ph.D. thesis, California Institute of Technology, 2006.
- [14] D. Shorokhov, S. T. Park, and A. H. Zewail, *ChemPhysChem* **6**, 2228 (2005).
- [15] S. Habershon and A. H. Zewail, *ChemPhysChem* **7**, 353 (2006).
- [16] M. M. Lin, D. Shorokhov, and A. H. Zewail, *Chem. Phys. Lett.* **420**, 1 (2006).
- [17] J. Cao, H. Ihee, and A. H. Zewail, *Proc. Natl. Acad. Sci. USA* **96**, 338 (1999).
- [18] H. Ihee, V. A. Lobastov, U. M. Gomez, B. M. Goodson, R. Srinivasan, C. Y. Ruan, and A. H. Zewail, *Science* **291**, 458 (2001).
- [19] C.-Y. Ruan, V. A. Lobastov, R. Srinivasan, B. M. Goodson, H. Ihee, and A. H. Zewail, *Proc. Natl. Acad. Sci. USA* **98**, 7117 (2001).
- [20] R. Srinivasan, J. S. Feenstra, S. T. Park, S. Xu, and A. H. Zewail, *J. Am. Chem. Soc.* **126**, 2266 (2004).
- [21] S. Xu, S. T. Park, J. S. Feenstra, R. Srinivasan, and A. H. Zewail, *J. Phys. Chem. A* **108**, 6650 (2004).
- [22] J. S. Feenstra, S. T. Park, and A. H. Zewail, *J. Chem. Phys.* **123**, 221104 (2005).
- [23] S. T. Park, J. S. Feenstra, and A. H. Zewail, *J. Chem. Phys.* **124**, 174707 (2006).
- [24] C.-Y. Ruan, F. Vigliotti, V. A. Lobastov, S. Chen, and A. H. Zewail, *Proc. Natl. Acad. Sci. USA* **101**, 1123 (2004).
- [25] F. Vigliotti, S. Chen, C.-Y. Ruan, V. A. Lobastov, and A. H. Zewail, *Angew. Chem., Int. Ed.* **43**, 2705 (2004).
- [26] C.-Y. Ruan, V. A. Lobastov, F. Vigliotti, S. Chen, and A. H. Zewail, *Science* **304**, 80 (2004).
- [27] C.-Y. Ruan, D.-S. Yang, and A. H. Zewail, *J. Am. Chem. Soc.* **126**, 12797 (2004).

- [28] S. Chen, M. T. Seidel, and A. H. Zewail, Proc. Natl. Acad. Sci. USA **102**, 8854 (2005).
- [29] S. Chen, M. T. Seidel, and A. H. Zewail, Angew. Chem., Int. Ed. **45**, 5154 (2006).
- [30] J. Jonh T. Yates, in *Experimental Innovations in Surface Science* (Springer-Verlag, New York, 1998), Chap. V. Delivery of adsorbates to surfaces: A. Gases, pp. 604–615.
- [31] A. Winkler and J. J. T. Yates, J. Vac. Sci. Technol. A **6**, 2929 (1988).
- [32] P. Baum and A. H. Zewail, Proc. Natl. Acad. Sci. USA **103**, 16105 (2006).
- [33] Z. L. Wang, *Elastic and Inelastic Scattering in Electron Diffraction and Imaging* (Plenum Press, New York, 1995).
- [34] L.-M. Peng, S. L. Dudarev, and M. J. Whelan, *High-Energy Electron Diffraction and Microscopy* (Oxford University Press, Oxford, 2004).
- [35] B. Fultz and J. Howe, *Transmission Electron Microscopy and Diffractometry of Materials* (Springer, Berlin, 2002).
- [36] A. Ichimiya and P. I. Cohen, *Reflection High Energy Electron Diffraction* (Cambridge University Press, Cambridge, 2004).
- [37] *Reflection High-Energy Electron Diffraction and Reflection Electron Imaging of Surfaces*, edited by P. K. Larsen and P. J. Dobson (Plenum Press, New York, 1987).
- [38] W. Braun, *Applied RHEED* (Springer, Berlin, 1999).
- [39] J. E. Mahan, K. M. Geib, G. Y. Robinson, and R. G. Long, J. Vac. Sci. Technol. A **8**, 3692 (1990).
- [40] A. H. Chin, R. W. Schoenlein, T. E. Glover, P. Balling, W. P. Leemans, and C. V. Shank, Phys. Rev. Lett. **83**, 336 (1999).

- [41] A. M. Lindenberg, I. Kang, S. L. Johnson, T. Missalla, P. A. Heimann, Z. Chang, J. Larsson, P. H. Bucksbaum, H. C. Kapteyn, H. A. Padmore, R. W. Lee, J. S. Wark, and R. W. Falcone, *Phys. Rev. Lett.* **84**, 111 (2000).
- [42] M. Dantus, S. B. Kim, J. C. Williamson, and A. H. Zewail, *J. Phys. Chem.* **98**, 2782 (1994).
- [43] H. Park, Z. Hao, X. Wang, S. Nie, R. Clinite, and J. Cao, *Rev. Sci. Instrum.* **76**, 083905 (2005).
- [44] J. I. Langford, *J. Appl. Cryst.* **11**, 10 (1978).
- [45] D. Balzar, in *Defect and microstructure analysis by diffraction*, edited by R. L. Snyder, J. Fiala, and H. J. Bunge (Oxford University Press, Oxford, 1999), Chap. Voigt function model in diffraction-line broadening analysis, pp. 94–126.
- [46] S. Pedersen and A. H. Zewail, *Molecular Physics* **89**, 1455 (1996).
- [47] J. Shah, *Ultrafast Spectroscopy of Semiconductors and Semiconductor Nanostructures* (Springer, Berlin, 1996).
- [48] S. K. Sundaram and E. Mazur, *Nat. Mater.* **1**, 217 (2002).
- [49] P. Saeta, J.-K. Wang, Y. Siegal, N. Bloembergen, and E. Mazur, *Phys. Rev. Lett.* **67**, 1023 (1991).
- [50] L. Huang, J. P. Callan, E. N. Glezer, and E. Mazur, *Phys. Rev. Lett.* **80**, 185 (1998).
- [51] V. G. Lifshits, A. A. Saranin, and A. V. Zotov, *Surface Phases on Silicon: Preparation, Structures, and Properties* (Wiley, New York, 1994).
- [52] A. Bansal, X. L. Li, S. I. Yi, W. H. Weinberg, and N. S. Lewis, *J. Phys. Chem. B* **105**, 10266 (2001).
- [53] W. A. Goddard, J. J. Barton, A. Redondo, and T. C. McGill, *J. Vac. Sci. Technol.* **15**, 1274 (1978).

- [54] M. Albrecht and G. Meyer-Ehmsen, in *Reflection High-Energy Electron Diffraction and Reflection Electron Imaging of Surfaces*, edited by P. Larsen and P. Dobson (Plenum Press, New York, 1988), pp. 211–224.
- [55] F. A. Lindemann, *Phys. Z.* **11**, 609 (1910).
- [56] R. S. Berry, in *Clusters of Atoms and Molecules: Theory, Experiment, and Clusters of Atoms*, edited by H. Haberland (Springer, Berlin, 1994), pp. 1–12.
- [57] F. Wooten, K. Winer, and D. Weaire, *Phys. Rev. Lett.* **54**, 1392 (1985).
- [58] K. Laaziri, S. Kycia, S. Roorda, M. Chicoine, J. L. Robertson, J. Wang, and S. C. Moss, *Phys. Rev. B* **60**, 13520 (1999).
- [59] P. D. Mitev and Y. Waseda, *High Temp. Mater. Processes* **21**, 53 (2002).
- [60] C. V. Shank, R. Yen, and C. Hirlimann, *Phys. Rev. Lett.* **50**, 454 (1983).
- [61] H. E. Elsayed-Ali and P. Weber, in *Time-Resolved Diffraction*, edited by J. R. Helliwell and P. M. Rentzepis (Oxford University Press, New York, 1997), Chap. Time-resolved surface electron diffraction, pp. 284–322.
- [62] P. L. Silvestrelli, A. Alavi, M. Parrinello, and D. Frenkel, *Phys. Rev. Lett.* **77**, 3149 (1996).
- [63] J. S. Blakemore, *J. Appl. Phys.* **53**, R123 (1982).
- [64] Z. H. Lu, T. Tyliczszak, and A. P. Hitchcock, *Phys. Rev. B* **58**, 13820 (1998).
- [65] J. F. Vetelino, S. P. Gaur, and S. S. Mitra, *Phys. Rev. B* **5**, 2360 (1972).
- [66] L. J. Clarke, *Surface Crystallography* (Wiley, New York, 1997).
- [67] C. Rose-Petruck, R. Jimenez, T. Guo, A. Cavalleri, C. W. Siders, F. Raksi, J. A. Squier, B. C. Walker, K. R. Wilson, and C. P. J. Barty, *Nature* **398**, 310 (1999).

- [68] D. Troost, L. Koenders, L.-Y. Fan, and W. Mönch, *J. Vac. Sci. Technol. B* **5**, 1119 (1987).
- [69] M. C. Downer and C. V. Shank, *Phys. Rev. Lett.* **56**, 761 (1986).
- [70] T. Sjodin, H. Petek, and H. L. Dai, *Phys. Rev. Lett.* **81**, 5664 (1998).
- [71] M. T. Seidel, S. Chen, and A. H. Zewail, submitted to *J. Phys. Chem. C*.
- [72] K. B. Blodgett, *J. Am. Chem. Soc.* **57**, 1007 (1935).
- [73] K. B. Blodgett, *J. Phys. Chem.* **41**, 975 (1937).
- [74] K. B. Blodgett and I. Langmuir, *Phys. Rev.* **51**, 964 (1937).
- [75] G. Roberts, *Langmuir-Blodgett Films* (Plenum, New York, 1990).
- [76] M. C. Petty, *Langmuir-Blodgett Films* (Cambridge University Press, Cambridge, 1996).
- [77] M. Dyck, P. Krüger, and M. Lösche, *Phys. Chem. Chem. Phys.* **7**, 150 (2005).
- [78] C. A. Helm, P. Tippmann-Krayer, H. Möhwald, J. Alsnielsen, and K. Kjaer, *Biophys. J.* **60**, 1457 (1991).
- [79] I. Fujiwara, M. Ohnishi, and J. Seto, *Langmuir* **8**, 2219 (1992).
- [80] M. Subirade, C. Salesse, D. Marion, and M. Pezolet, *Biophys. J.* **69**, 974 (1995).
- [81] J. Zhang and P. R. Unwin, *J. Am. Chem. Soc.* **124**, 2379 (2002).
- [82] K. Nørgaard and T. Bjørnholm, *Chem. Commun.* **14**, 1812 (2005).
- [83] A. P. Girard-Egrot, S. Godoy, and L. J. Blum, *Adv. Colloid Interface Sci.* **116**, 205 (2005).
- [84] G. Khanarian, *Thin Solid Films* **152**, 265 (1987).
- [85] J. A. Zasadzinski, R. Viswanathan, L. Madsen, J. Garnæs, and D. K. Schwartz, *Science* **263**, 1726 (1994).

- [86] D. Y. Takamoto, E. Aydil, J. A. Zasadzinski, A. T. Ivanova, D. K. Schwartz, T. Yang, and P. S. Cremer, *Science* **293**, 1292 (2001).
- [87] D. K. Schwartz, *Surf. Sci. Rep.* **27**, 241 (1997).
- [88] J. B. Peng, G. T. Barnes, and I. R. Gentle, *Adv. Colloid Interface Sci.* **91**, 163 (2001).
- [89] D. K. Schwartz, R. Viswanathan, J. Garnaes, and J. A. Zasadzinski, *J. Am. Chem. Soc.* **115**, 7374 (1993).
- [90] P. P. Karageorgiev, V. V. Karageorgieva, V. V. Luchinin, and A. Z. Kazak-Kazakevich, *Crystallogr. Rep.* **43**, 968 (1998).
- [91] M. K. Mukhopadhyay, M. K. Sanyal, A. Datta, J. Webster, and J. Penfold, *Chem. Phys. Lett.* **407**, 276 (2005).
- [92] M. C. Shih, T. M. Bohanon, J. M. Mikrut, P. Zschack, and P. Dutta, *J. Chem. Phys.* **96**, 1556 (1992).
- [93] S. Kundu, A. Datta, and S. Hazra, *Chem. Phys. Lett.* **405**, 282 (2005).
- [94] R. Peterson, G. J. Russell, J. Earls, and I. Girling, *Thin Solid Films* **161**, 325 (1988).
- [95] I. Robinson, J. R. Sambles, and I. R. Peterson, *Thin Solid Films* **172**, 149 (1989).
- [96] I. Robinson, D. J. Jarvis, and J. R. Sambles, *J. Phys. D: Appl. Phys.* **24**, 347 (1991).
- [97] V. Brzezinski and I. R. Peterson, *J. Phys. Chem.* **99**, 12545 (1995).
- [98] S. A. Evenson, J. P. Badyal, C. Pearson, and M. C. Petty, *J. Phys. Chem.* **100**, 11672 (1996).
- [99] G. L. Gaines, Jr., *Thin Solid Films* **68**, 1 (1980).

- [100] A. Bonnerot, P. A. Chollet, H. Frisby, and M. Hoclet, *Chem. Phys.* **97**, 365 (1985).
- [101] M. Kinzler, A. Schertel, G. Hähner, C. Wöll, M. Grunze, H. Albrecht, G. Holzhüter, and T. Gerber, *J. Chem. Phys.* **100**, 7722 (1994).
- [102] I. R. Peterson and G. J. Russell, *Thin Solid Films* **134**, 143 (1985).
- [103] A. Leuthe and H. Riegler, *J. Phys. D: Appl. Phys.* **25**, 1786 (1992).
- [104] A. Leuthe, L. F. Chi, and H. Riegler, *Thin Solid Films* **243**, 351 (1994).
- [105] R. M. Morelis, A. P. Girardegrot, and P. R. Coulet, *Langmuir* **9**, 3101 (1993).
- [106] S. W. Hui, D. F. Parsons, and M. Cowden, *Proc. Natl. Acad. Sci. USA* **71**, 5068 (1974).
- [107] L. L. Orekhova, A. Mogilevich, S. V. Orechov, V. V. Klechkovskaya, and L. A. Feigin, *Physica B* **198**, 144 (1994).
- [108] M. Stevens, M. Longo, D. L. Dorset, and J. Spence, *Ultramicroscopy* **90**, 265 (2002).
- [109] M. Seul, P. Eisenberger, and H. M. McConnell, *Proc. Natl. Acad. Sci. USA* **80**, 5795 (1983).
- [110] B. W. Gregory, R. A. Dluhy, and L. A. Bottomley, *J. Phys. Chem.* **98**, 1010 (1994).
- [111] P. Lozano, A. J. Fernández, J. J. Ruiz, L. Camacho, and E. M. M. T. Martín, *J. Phys. Chem. B* **106**, 6507 (2002).
- [112] J. K. H. Hörber, C. A. Lang, T. W. Hänsch, W. M. Heckl, and H. Möhwald, *Chem. Phys. Lett.* **145**, 151 (1988).
- [113] J. M. Solletti, M. Botreau, F. Sommer, W. L. Brunat, S. Kasas, T. M. Duc, and M. R. Celio, *Langmuir* **12**, 5379 (1996).

- [114] G. J. Russell, M. C. Petty, I. R. Peterson, G. G. Roberts, J. P. Lloyd, and K. K. Kan, *J. Mater. Sci.* **3**, 25 (1984).
- [115] I. Kitaigorodskii, *Organic Chemical Crystallography* (Consultants Bureau, New York, 1961).
- [116] C. Naselli, J. P. Rabe, J. F. Rabolt, and J. D. Swalen, *Thin Solid Films* **134**, 173 (1985).
- [117] C. Naselli, J. F. Rabolt, and J. D. Swalen, *J. Chem. Phys.* **82**, 2136 (1985).
- [118] W. Richardson and J. K. Blasie, *Phys. Rev. B* **39**, 12165 (1989).
- [119] C. Böhm, R. Steitz, and H. Riegler, *Thin Solid Films* **178**, 511 (1989).
- [120] J. E. Riegler, *J. Phys. Chem.* **93**, 6475 (1989).
- [121] P. Tippmann-Krayer, R. M. Kenn, and H. Möhwald, *Thin Solid Films* **210/211**, 577 (1992).
- [122] C.-F. Chou, A. J. Jin, S. W. Hui, C. C. Huang, and J. T. Ho, *Science* **280**, 1424 (1998).
- [123] R. Viswanathan, L. L. Madsen, J. A. Zasadzinski, and D. K. Schwartz, *Science* **269**, 51 (1995).
- [124] H. D. Sikes and D. K. Schwartz, *Science* **278**, 1604 (1997).
- [125] J. B. Peng, G. J. Foran, G. T. Barnes, and I. R. Gentle, *Langmuir* **19**, 4701 (2003).
- [126] M. P. Fontana and P. Facci, *J. Chem. Phys.* **111**, 5562 (1999).
- [127] J. K. Basu, M. K. Sanyal, M. Mukherjee, and S. Banerjee, *Phys. Rev. B* **62**, 11109 (2000).
- [128] M. K. Mukhopadhyay, M. K. Sanyal, A. Datta, M. Mukherjee, T. Geue, J. Grenzer, and U. Pietsch, *Phys. Rev. B* **70**, 245408 (2004).

- [129] K. Kobayashi, K. Takaoka, and S. Ochiai, *Thin Solid Films* **159**, 267 (1988).
- [130] M. R. Buhaenko, M. J. Grundy, R. M. Richardson, and S. J. Roser, *Thin Solid Films* **159**, 253 (1988).
- [131] V. M. Kaganer, H. Möhwald, and P. Dutta, *Rev. Mod. Phys.* **71**, 779 (1999).
- [132] S. B. Dierker, C. A. Murray, J. D. Legrange, and N. E. Schlotter, *Chem. Phys. Lett.* **137**, 453 (1987).
- [133] K. Harlos, H. Eibl, I. Pascher, and S. Sundell, *Chem. Phys. Lipids* **34**, 115 (1984).
- [134] A. L. Harris and N. J. Levinos, *J. Chem. Phys.* **90**, 3878 (1989).
- [135] S. Ma, M. Aono, and T. Suzuki, *Colloids Surf. A* **257–258**, 357 (2005).
- [136] A. Rouse, C. Rischel, I. Uschmann, E. Forster, P. A. Albouy, J. P. Geindre, P. Audebert, J. C. Gauthier, and A. Antonetti, *J. Appl. Crystallogr.* **32**, 977 (1999).
- [137] M. Seidel, J. Jethwa, and P. Vöhringer, *Russ. Chem. Bull., Int. Ed.* **53**, 1471 (2004).
- [138] N. E. Levinger, *Curr. Opin. Colloid Interface Sci.* **5**, 118 (2000).
- [139] M. C. Rheinstädter, C. Ollinger, G. Fragneto, F. Demmel, and T. Salditt, *Phys. Rev. Lett.* **93**, 108107 (2004).
- [140] D.-S. Yang, N. Gedik, and A. H. Zewail, submitted to *J. Phys. Chem. C*.
- [141] T. Fukui, M. Sugi, and S. Iizma, *Phys. Rev. B* **22**, 4898 (1980).
- [142] J. Tang and A. H. Zewail (unpublished).
- [143] L. Meinhold and J. Smith, *Phys. Rev. Lett.* **95**, 218103 (2005).
- [144] C. Okazaki, *Jpn. J. Appl. Phys.* **37**, 983 (1998).